Corrosion of Ceramic Materials

Elizabeth J. Opila
Cleveland State University
Resident Research Associate at NASA Lewis Research Center
Cleveland, OH

Nathan S. Jacobson
NASA Lewis Research Center
Cleveland, OH

1. Introduction

Non-oxide ceramics are promising materials for a range of high temperature applications. Selected current and future applications are listed in Table I. In all such applications, the ceramics are exposed to high temperature gases. Therefore it is critical to understand the response of these materials to their environment.

The variables to be considered here include both the type of ceramic and the environment to which it is exposed. Non-oxide ceramics include borides, nitrides, and carbides. Most high temperature corrosion environments contain oxygen and hence the emphasis of this chapter will be on oxidation processes of the type (Shaw et al., 1987; Jacobson and Opila, 1999):

$$2\,MB + 5/2\,O_2(g) = 2\,MO + B_2O_3 \quad (1)$$

$$MC + O_2 = MO + CO(g) \quad (2)$$

$$MN + \tfrac{1}{2}\,O_2 = MO + N_2(g) \quad (3)$$

However other corrosive environments, such as water vapor and molten salts, will also be discussed.

In oxidation studies, most of the oxidation properties are determined by the oxide film. Therefore ceramic materials discussed in this chapter will be classified according to the particular oxide film. In general, long-term applications require a protective oxide with a low oxygen diffusivity. The leading protective oxides for ceramics are silica (SiO_2) and alumina (Al_2O_3). Other protective oxides, such as boria (B_2O_3), may be acceptable for short-term applications. Figure 1 illustrates the range of oxidation rates for different protective oxides (Shaw et al., 1987).

Most of the emphasis here will be on the silica forming ceramics--silicon carbide (SiC) and silicon nitride (Si_3N_4). Due to the proposed applications of silica-forming ceramics, behavior of these materials in complex corrosive environments will also be discussed. Next alumina forming

ceramics, aluminum nitride (AlN) and aluminum carbide (Al_4C_3), will be examined. The third class of ceramics to be considered are boria forming materials, such as boron nitride (BN). Next, transition metal carbides and nitrides which form the corresponding transition metal oxides will be discussed. Ceramic materials which form mixed oxide scales will also be considered. Finally, the oxidation of ceramic matrix composites (CMCs), which involves several parallel processes, is an important current area of research and will conclude the chapter.

High temperature corrosion of metals and alloys has been more extensively studied than high temperature corrosion of ceramics. Many of the same experimental techniques and basic principles apply to both metals and ceramics. In the case of metals, our fundamental knowledge is derived from studies on high purity metals and alloys. Oxidation/corrosion studies on metals are typically done on small coupons. For ceramics, high purity chemically vapor deposited (CVD) samples have recently become available for such studies. CVD coupons are available for most ceramics, however in some cases only ceramic powders are available. Experimental approaches and analyses of data must be modified for powders. Finally, an important chemical difference between metals and ceramics is the formation of gases in the case of ceramic oxidation, as illustrated in reactions (2) and (3). The escape of gases through the oxide film is an important issue.

2. Experimental Techniques

There are two objectives in high temperature corrosion studies: understanding the interaction of the ceramic and corrodent on a fundamental level and assessing the behavior of the ceramic in an actual application environment. The former requires a clean, well-defined environment designed to vary one or two parameters methodically (e.g. temperature and/or oxygen pressure). The latter requires a complex environment which accurately models the actual application. The emphasis of this chapter will be on fundamental oxidation mechanisms. However, when data are available, more complex environments, which come closer to the actual application, will also be discussed.

Most fundamental oxidation studies involve high purity oxygen in a well-controlled laboratory furnace at constant temperature. The amount of oxide can be monitored as a function of time via several techniques. The most common are optical measurements of oxide thickness and thermogravimetric monitoring of total weight gain. A thermogravimetric apparatus is illustrated in Figure 2. It is also possible to monitor oxidation kinetics via sensitive pressure gauges to monitor oxygen gas uptake and/or product gas release. Recently Gozzi and co-workers (1997) have developed a zirconia sensor to precisely monitor oxygen uptake in refractory carbide oxidation studies.

Kinetic information obtained via the above techniques is very useful in determining the rate controlling step of the reaction process. Scale formation which is linear with time obeys the following rate law and indicates an interfacial reaction or gas phase diffusion is rate controlling (Kofstad, 1988):

$$x = k_l\, t \tag{4}$$

Here x is the oxide scale thickness, k_l is the linear rate constant and t is the time. Scale formation which is parabolic with time obeys the following rate law and indicates diffusion through the oxide scale is rate controlling:

$$x^2 = k_p\, t \tag{5}$$

Here k_p is the parabolic rate constant. Another common observation is linear weight loss, which generally indicates that gas phase diffusion of volatile products through a boundary layer is rate controlling. For a flat plate coupon, this boundary layer-controlled flux, J, is given by (Geiger and Poirier,1973):

$$J = 0.664\,(Re)^{0.5}\,(Sc)^{0.33}\,\rho_v \frac{D}{L} \tag{6}$$

$$Re = \frac{\rho v L}{\eta};\quad Sc = \frac{\eta}{\rho D} \tag{7}$$

Here, the dimensionless quantities Re and Sc are the Reynolds and Schmidt numbers, respectively. In these expressions, ρ is the density of the gas atmosphere above the sample, ρ_v is the density of the volatile species at the oxide/gas interface, v is the linear gas velocity, η is the viscosity, L is a characteristic dimension of the coupon and D is the diffusivity of the volatile species in the boundary layer.

The above rate laws are for coupons of well-defined geometry, however they can be adapted to powders as well. Jander (Hulbert, 1969) first developed a 'shrinking sphere' model for this purpose. First assume the radius of each particle, R, decreases linearly with time:

$$\alpha = 1 - \frac{R^3}{R_o^3} = 1 - \frac{(R_o - kt)^3}{R_o^3} \tag{8}$$

$$1-(1-\alpha)^{1/3}=\frac{kt}{R} \tag{9}$$

Here R_o is the initial radius of the particle and α is the volume fraction reacted. A plot of $1-(1-\alpha)^{1/3}$ vs. t gives a linear plot if an interface reaction is rate controlling. If diffusion in the solid is rate controlling then Equation (8) becomes:

$$\alpha = 1-\frac{R^3}{R_0^3} = 1-\frac{(R_o - k_p\sqrt{t})^3}{R_0^3} \tag{10}$$

$$1-(1-\alpha)^{1/3}=\frac{k_p\sqrt{t}}{R} \tag{11}$$

Now a plot of $1-(1-\alpha)^{1/3}$ vs. $\sqrt{t}$ will give a linear plot if diffusion is rate controlling. In theory, boundary-layer controlled diffusion rate laws can also be extended to powders, but diffusion through a powder bed is a more complex problem.

Once an oxide scale is established on the coupon or powder, its composition and morphology may be characterized by a variety of optical, electron optical, and x-ray diffraction techniques (XRD). In many cases the products are amorphous and other techniques are used to supplement XRD, such as chemical analyses of the scale alone. Scanning electron microscopy (SEM) has proven most useful, although transmission electron microscopy (TEM) is playing an increasingly important role as well.

The preceding discussion has dealt with studies of ceramics in pure environments at constant temperatures. In actual applications, high temperature materials are rarely at constant temperatures, but rather thermally cycled. Materials which show good isothermal resistance may not show oxidation resistance under thermal cycling. Thus thermal cycling oxidation tests are important in understanding overall oxidation behavior.

A variety of complex test rigs have been developed to simulate the behavior of high temperature materials in actual process environments. Consider first combustion conditions. Figure 3 shows calculated combustion gases for burning of a typical hydrocarbon fuel. Note that oxygen is only one constituent of the hot gas stream. It consists of CO_2, H_2O, N_2 and O_2 in fuel-lean environments and CO, H_2, and N_2 in fuel-rich environments. Burner rigs are very useful in simulating turbine engine conditions (Deadmore et al., 1978). Figure 4 shows a schematic of a burner rig. It is critical to control the parameters as tightly as possible in such a rig in order to allow comparison of one burner to another. Similar large scale rigs have been developed in order to simulate the environments in coal slagging (Ferber and Tennery, 1983) and various chemical process environments.

3. Oxidation of Silica Formers

To begin this section on the oxidation of silica formers, SiC and Si_3N_4, some of the properties of silica are briefly reviewed. Next, the oxidation of silicon is considered. While silicon is not a ceramic, its oxidation behavior nevertheless forms the basis for discussion of other silica formers. The section then proceeds from the oxidation mechanisms and rates obtained under the most ideal, clean conditions in pure oxygen to those conditions closer to actual application environments. These include effects of small amounts of impurities, sintering aids, effects of other oxidants, cyclic oxidation, effects of oxidation on strength, volatility effects, and hot corrosion.

3.1. Properties of Silica

Silica scales can exist in either an amorphous or a crystalline form. Both are composed of SiO_4 tetrahedra. The crystalline phase generally observed is cristobalite. Tridymite is sometimes observed when impurities are present, however, this phase will not be discussed further. Cristobalite can be envisioned as a regular lattice of six member rings composed of alternating silicon and oxygen atoms as shown in Figure 5a. The amorphous structure is an open and disordered structure in which seven or eight member rings can also be found as shown schematically in Figure 5b.

Under many conditions, transport of oxidant through the silica scale limits the growth rate of silica and the corresponding recession of the matrix material. Understanding the transport of oxidant or gaseous products through silica is therefore crucial to predicting the oxidation rates of silica forming materials. Oxygen transport in silica has been reviewed by Lamkin et al. (1992) in detail and is summarized briefly here. Two transport mechanisms can occur. First, molecular oxygen can move through the interstitial rings in the silica structure by a permeation mechanism. Second, charged oxygen species can move from oxygen lattice site to lattice site. The second process is expected to have a higher enthalpy since bond breaking is required.

While transport through silica is slower than any other oxide under ideal conditions as shown in Figure 1, and thus limits the growth rate of silica scales, the transport properties of this oxide are very susceptible to the environment and under any real application conditions these slow rates of silica growth are seldom observed.

3.2. Basic Oxidation Mechanisms of Silica Formers

3.2.1. Oxidation of Silicon

The oxidation of silicon has been studied extensively due to the need for formation of dielectric silica layers on silicon by thermal oxidation for semiconductor devices. Deal and Grove (1965) have written a classic paper on this subject in which gas phase diffusion rates, linear reaction rates of oxygen with silicon, as well as oxygen transport rates through the growing silica scale are all considered. It was found that silicon oxidation can be described by a linear parabolic rate law:

$$x_o^2 + Ax_o = B(t + \tau) \tag{12}$$

where x_o is the oxide thickness, t is the time, and τ is a time correction for any pre-existing oxide. B is the parabolic rate constant, often referred to as k_p in the oxidation literature. B/A is the linear rate constant referred to as k_l in the oxidation literature. At short times Equation 12 reduces to $x_o = (t + \tau)B/A$ which is the simple case for reaction controlled oxidation. At long times Equation 12 reduces to $x_o^2 = Bt$, which is the simple case for solid state diffusion controlled oxidation.

In addition Deal and Grove (1965) show that oxygen transport through the silica scale occurs by molecular permeation of O_2 since B is directly proportional to the oxygen partial pressure. Also, the parabolic rates measured by Deal and Grove (1965) were in good agreement with rates measured by Norton for permeation of molecular oxygen through silica.

3.2.2. Oxidation of Pure SiC in Dry Oxygen

Since SiC oxidation also results in the formation of a silica scale, many analogies can be made with the oxidation of silicon. First, the oxidation of SiC can be modeled using the Deal and Grove treatment of linear parabolic kinetics. Ramberg et al. (1996) have studied the oxidation of pure SiC in the temperature range of 800-1100°C and shown that the linear reaction rate limits the oxidation rate in this temperature range. At temperatures of 1200°C and higher, the oxidation kinetics are generally considered purely parabolic (Costello and Tressler, 1986; Zheng et al., 1990a; Ogbuji and Opila, 1995). As first noted by Motzfeldt (1964), the parabolic rates of SiC should be 1.5 to 2 times slower than Si due to the additional oxygen consumed in the formation of gaseous products by the reactions:

$$SiC + 3/2\ O_2(g) = SiO_2 + CO(g) \tag{13}$$

$$SiC + 2\ O_2(g) = SiO_2 + CO_2(g) \tag{14}$$

This has been shown to be true experimentally (Motzfeldt, 1964; Costello and Tressler, 1986; Ogbuji and Opila, 1995). Parabolic oxidation rates for pure materials, Si and SiC, as well as Si_3N_4 discussed below, are compared in Figure 6 on an Arrhenius plot.

Oxidation of silicon is typically studied to 1200°C, whereas SiC is useful to much higher temperatures. Thus, additional high temperature phenomena for SiC oxidation must be discussed. First, Zheng et al. (1990a,b) have shown by oxygen isotope tracer studies that significant exchange with the oxygen lattice occurs at temperatures of 1300°C and higher. In addition it was found that the dependence of the oxidation rate of SiC on oxygen partial pressure decreases as temperature is increased (Zheng et al. 1990b). Both these results suggest that at higher temperatures, increased transport of oxygen through the silica scale by motion of charged oxygen species on the oxygen network sites occurs. The overall oxidation rate, however, is still dominated by molecular permeation through interstitial sites up to temperatures of 1500°C (Ogbuji and Opila, 1995).

An additional complication occurring at higher temperatures is the crystallization of the silica scale. Thermally grown silica crystallites are spherulitic (Ogbuji, 1981) as shown in Figure 7. For very pure SiC, crystallization occurs at temperatures of 1300°C and higher (Ogbuji and Opila, 1995). Several studies report decreases in weight change with time and attribute this to crystallization of the silica scale (Narushima et al., 1989; Costello and Tressler, 1981; Fergus and Worrell, 1990). Recent work (Ogbuji, 1997) shows that oxygen transport through cristobalite is slower than through amorphous silica by about a factor of 30 at 1300°C. Under clean oxidation conditions, however, a continuous film of amorphous silica is found under the cristobalite. In addition, a film of amorphous silica is found between the cristobalite spherulites (Ogbuji, 1981). Thus, the extent of crystallization is not complete enough to result in a slowing in the observed oxidation rate of SiC at least for times less than one hundred hours (Ogbuji and Opila, 1995).

An upturn in the oxidation rate and activation energy of SiC at temperatures of about 1350 to 1400°C has been observed in several studies (Costello and Tressler, 1981, 1986; Fergus and Worrell, 1990; Fillipuzzi et al., 1992; Frisch et al., 1988; Ramberg, 1997; Singhal, 1976a; Zheng et al., 1990a) This has been variously attributed to crystallization of the scale (Costello and Tressler, 1981; Singhal, 1976a; Frisch et al., 1988) or a change in oxygen transport mechanism (Costello and Tressler, 1986; Fergus and Worrell, 1990; Zheng et al., 1990a; Filipuzzi et al., 1992). However, it has also been shown that this increase in rate and activation energy is not observed for very pure materials in very clean conditions (Ogbuji and Opila, 1995; Ramberg, 1997) even when crystallization occurs. It has been suggested that this upturn in rates and energies may be

attributed to impurities either in the oxidation environment (Ogbuji and Opila, 1995) or in the SiC (Ramberg, 1997).

Oxidation of SiC at temperatures greater than 1500°C has been studied by Narushima et al. (1989) and Schiroky et al. (1986). Narushima et al. (1989) showed that the oxidation kinetics were parabolic at temperatures as high as 1675°C. The oxide scales formed were initially amorphous and after four hours primarily crystalline. After the scale crystallized the oxidation rates were about an order of magnitude slower. Schiroky et al. (1986) found that at temperatures of 1700°C and higher the oxide scale, being near its melting point, became amorphous. Under these conditions bubbles formed in the silica scale due to the presence at the interface of the gaseous products CO and or CO_2 at pressures greater than one atmosphere.

3.2.3. Oxidation of Pure Si_3N_4 in Dry Oxygen

The oxidation of silicon nitride typically occurs with parabolic kinetics (Choi et al. (1989), Du et al., 1989a; Schiroky et al. (1986); Ogbuji and Opila, 1995), is dependent on oxygen partial pressure, and is independent of nitrogen partial pressure (Du et al., 1989a). These three observations show that the oxidation kinetics are controlled by oxygen transport across a growing scale. However, it is also well known that the oxidation of pure Si_3N_4 in clean conditions at temperatures less than 1500°C are much lower than the oxidation rates of Si and SiC (Choi et al., 1989; Du et al., 1989a; Ogbuji and Opila, 1995) as shown in Figure 6. This has been attributed to the formation of a silicon oxynitride layer which forms below the silica scale during oxidation of Si_3N_4. The composition of the oxynitride layer has been described as both a discrete phase, Si_2ON_2, (Du et al., 1989a) and as a solid solution of SiO_2 and Si_3N_4 of variable composition, SiO_xN_y (Ogbuji, 1995). This leads to the formulation of the oxidation reactions in two possible ways. For the discrete oxynitride phase the oxidation proceeds by a two-step reaction:

$$Si_3N_4 + 3/4O_2(g) = 3/2\ Si_2ON_2 + 1/2\ N_2(g) \quad (15)$$

$$Si_2ON_2 + 3/2\ O_2(g) = 2SiO_2 + N_2(g) \quad (16)$$

While for the solution oxynitride, the oxidation reaction has been formulated by Sheldon as:

$$Si_3N_{4(1-x)}O_{6x} = 3\ \delta x\ O_2(g) = Si_3N_{4(1-x-\delta x)}O_{6(x+\delta x)} + 2\ \delta x\ N_2(g) \quad (17)$$

The evidence that supports a discrete oxynitride phase is the discontinuity in the etching rate of the oxide scale formed on silicon nitride (Du et al., 1989a) as well as the contrast observed in TEM and SEM images of scale cross-sections (Ogbuji and Smialek, 1991). An SEM image of the

oxynitride/oxide formed on Si_3N_4 is shown in Figure 8. However, for a diffusion controlled oxidation process, it is assumed that equilibrium is achieved at the oxide/matrix interface. This assumption results in impossibly high nitrogen pressures at the Si_2ON_2/N_2 interface (Du et al., 1989b). Other work by Ogbuji and Bryan (1995) shows an amorphous oxynitride layer with a continuous gradation in oxygen and nitrogen composition from SiO_2 to Si_3N_4. The accompanying model (Ogbuji, 1995) proposes that oxidation proceeds by a substitution of oxygen for nitrogen across the graded SiO_xN_y network rather than at an interface. This is illustrated in Figure 9. The contrast observed in images of scale cross-sections is attributed to the interface between the amorphous subscale and the crystalline silica top layer.

The high temperature oxidation of pure Si_3N_4 has been studied by Hirai et al. (1980) as well as Narushima et al. (1993a). As for SiC, as the temperature is increased toward the melting point of silica, the scales formed on Si_3N_4 become more amorphous and the oxidation kinetics change from parabolic to linear.

3.3. Oxidation of SiC and Si_3N_4 in the Presence of Low Level Impurities

The oxidation rates of SiC and especially Si_3N_4 in clean environments are quite low. However, for any real application, impurities in the oxidizing environment are likely to be present. The effect of impurities on the oxidation rate of these materials can be quite significant. This issue has been explored experimentally in a number of ways. First, one of the most common contaminants, sodium, was ion implanted in both SiC (Zheng et al., 1992a) and Si_3N_4 (Zheng et al., 1992b) at levels between 50-1000 ppm. Upon oxidation, the Na was incorporated in the oxide scale. The oxidation kinetics remained parabolic for both implanted materials. The oxidation rates were enhanced by a factor of two in the case of SiC, but by an order of magnitude for the case of Si_3N_4. Nevertheless, the oxidation rate of Si_3N_4 remained lower than that of SiC. The activation energy for oxidation remained the same for SiC, but decreased for Si_3N_4. The enhanced oxidation in the presence of Na is attributed to the accelerated transport of oxygen through the silica scale which is due to incorporation of Na in the silica network and the formation of non-bridging oxygens. The incorporation of Na into the silica network is shown schematically in Figure 5c. In the case of Si_3N_4 the more dramatic enhancement in oxidation rates is attributed to the modification of the silicon oxynitride structure by sodium. While this phase is still present, in this case, its protective properties diminish substantially with incorporation of sodium.

Enhanced parabolic oxidation rates of SiC and Si_3N_4 due to contamination from furnace tubes used in oxidation experiments have also been observed (Choi et al., 1989; Opila, 1995; Ogbuji and Opila, 1995; Fox, 1998). This enhancement is also attributed to Na impurities from impurities in alumina tubes (Opila, 1995). In one case (Fox, 1998), the oxidation rates of SiC and Si_3N_4,

both very pure CVD materials, were found to follow parabolic kinetics, but at essentially the same rate. It was proposed that impurities from the alumina furnace tubes modified the structure of the silicon oxynitride so much that it no longer offered any additional barrier to oxygen transport than the silica scale. Backhaus-Ricault and Gogotsi (1995) have also shown that silicon oxynitride is absent in hot isostatically pressed additive-free silicon nitride. This result may also be due to minor amounts of impurities resulting from the HIP process.

Finally, moderate amounts of alkali impurities have been intentionally introduced into silica scales growing on both SiC and Si_3N_4 by vapor techniques (Pareek and Shores, 1991; McNallan et al., 1994; Sun et al., 1994). Alkali halides or alkali salts are vaporized in one portion of a furnace and transported with a carrier gas to the test specimen in another zone of the furnace. Depending on the activity of the alkali vapor species in the test, the oxide scale composition varied from 0.4 (Pareek and Shores, 1991) to 30 (Sun et al., 1994) mole percent alkaline oxide. Oxidation kinetics for the lowest levels of alkali impurity in the scale were parabolic, but elevated over rates observed for pure silica formers (Pareek and Shores, 1991). As the alkali content increased, oxidation rates increased and changed from parabolic to linear kinetics (Pareek and Shores, 1991; McNallan et al., 1994; Sun et al., 1994). The linear oxidation kinetics were ascribed to gas phase mass transfer controlled kinetics (McNallan et al., 1994) or interfacial corrosion reaction limited kinetics (Sun et al., 1994; Pareek and Shores, 1991).

In combustion environments, the deposition of alkali impurities in combination with impurities in common fuels, called hot corrosion, results in dramatically increased corrosion rates. This more severe corrosion process is discussed in Section 3.9.

3.4. Oxidation of SiC and Si_3N_4 Containing Sintering Aids

Sintering aids are often added to SiC and Si_3N_4 to promote densification of these materials. Sintering aids have several noteworthy effects on the oxidation of silica forming materials including increased oxidation rates, change in rate controlling mechanism, and alteration of the oxide scale structure.

First, for SiC materials, typical sintering aids are B, C, and/or Al. B and C are typically added to the SiC in the form of B_4C (Browning et al., 1987). For commercially available SiC containing B_4C at levels of about 0.5 wt% levels (Browning et al., 1987), parabolic oxidation rates are the same as those observed for CVD SiC (comparing results from Costello and Tressler, 1986 to Ogbuji and Opila, 1995). It has been shown that the boron segregates into the oxide leaving a depleted region in the SiC near the interface (Costello et al., 1981). Boron in turn is depleted near the oxide surface due to volatilization losses. While boron at this concentration has no apparent

affect on the oxidation rate, bubbles are formed in the oxide scale at temperatures between 1200 and 1300°C as partial pressures of volatile boron species approach one atm. (Fergus and Worrell, 1990).

Aluminum additions to SiC are made in the form of alumina additions typically in the amount of 4 wt%. This additive has been studied by Hinze et al. (1975a), Singhal and Lange (1975), Singhal (1976a), and Costello and Tressler (1981). It has been found that the parabolic oxidation rates increase with alumina content (Singhal and Lange, 1975) as shown in Figure 10. The alumina additives tend to enhance crystallization of the scale (Singhal, 1976a; Costello and Tressler, 1981). Glassy areas of the oxide scale are found to be enriched in Al as well as other impurities. Also, for high aluminum contents, mullite can be found in the oxide scale. Apparent activation energies for oxidation are higher than for pure SiC. This has been variously attributed to a mechanism controlled by outdiffusion of the oxidation product CO (Singhal, 1976a), crystallization of the silica scale (Costello and Tressler, 1981), or to incorporation of aluminum in the glass-forming network (Hinze et al., 1975a). Work by Costello and Tressler (1981) indicates that the oxidation rate is controlled by oxygen transport through the Al_2O_3-altered scales.

Densification of silicon nitride by conventional hot pressing also requires the use of sintering aids, typically MgO and Y_2O_3. As for SiC, the oxidation rates of these materials increase as the silica scale becomes less pure. Singhal (1976b) showed that silicon nitride, 1 wt% MgO oxidizes parabolically but that oxidation rates are higher than for pure Si_3N_4. The oxide was composed of cristobalite with segregated magnesium silicate ($MgSiO_3$) grains on the surface. Similar yttrium silicate phases are shown in Figure 11. It was also demonstrated that oxidation rates were independent of both oxygen and nitrogen partial pressure. It was suggested that out-diffusion of the Mg cation to the silica surface controls the rate. In a series of elegant oxidation/reoxidation experiments, Cubiciotti and Lau (1978, 1979) demonstrated that diffusion of the sintering aid cation, Mg or Y, to the surface controlled the oxidation rate of these materials. The weight change kinetics for an oxidation/reoxidation experiment are shown in Figure 12 for Si_3N_4 containing MgO. After oxidizing and removing the scale, reoxidation follows the original kinetic curve showing that the oxidation rate is not dependent on silica thickness. Clarke (1983) has modeled this process assuming gradients in chemical potential of these cations are maintained by continuous formation of SiO_2 and the consumption of cations in the scale to form silicates at the oxide surface.

It should be noted that if too much sintering aids are added to these materials, cation-rich silicates form in the grain boundaries during oxidation. The volume expansion that accompanies this phase formation results in destruction of the material (Patel and Thompson, 1988). Finally, for large amounts of phases added to SiC or Si_3N_4 the resulting material may be considered a composite

material. Oxidation of these materials may result in multiphase oxide scales. This type of behavior is considered in more detail in Section 7 below.

3.5. Oxidation of Silica Formers in Other Oxidants

3.5.1. Oxidation of Si, SiC, and Si_3N_4 in Water Vapor

Return now to the behavior of very pure materials and consider the effect of changes in the gaseous environment from dry oxygen to those environments more commonly found for high temperature applications of silica forming ceramics. Many proposed high temperature applications for SiC and Si_3N_4 are in combustion environments. Water vapor is always present in combustion environments since it is a product of the burning of hydrocarbon fuels. Water vapor is typically found at a level of about 10% of the total gas pressure, independent of fuel-to-air ratio, as shown in Figure 3 (Jacobson 1993). The effects of water vapor on oxidation of SiC and Si_3N_4 are therefore of significant interest and can be classified in three areas. First, water vapor increases the transport of impurity species to the silica scale. As already demonstrated, these impurities increase the oxidation rate of silica formers. Second, water vapor, as the primary oxidant species, intrinsically increases the oxidation rate of silica formers. Finally, silica scales are volatile in water vapor due to the formation of gaseous silicon hydroxide species. Under these conditions SiC and Si_3N_4 oxidize to form silica scales which simultaneously volatilize. The net result is paralinear kinetics and enhanced rates of matrix recession. Each of these effects will now be considered in more detail.

3.5.1.1. Water Vapor-Impurity Effects

Water vapor enhances the transport of impurities because of the stability of gaseous hydroxides. Many impurities found in real application environments, such as Na and K, readily form hydroxides at partial pressures greater than other alkali-containing vapor species. This is documented in several of the studies already referenced in Section 3.3 on low level impurities above. For example, Pareek and Shores (1991) have calculated that KOH formation from K_2CO_3 in water vapor increases the activity of potassium-containing species in the vapor phase as shown in Figure 13. The resulting increased activity of potassium in the silica scale increases the oxidation rate of SiC. Opila (1994) also noted that sodium impurities from furnace tubes contaminated SiO_2 scales on SiC at an increased level in the presence of water vapor presumably to due sodium hydroxide formation. Higher oxidation rates were observed for samples oxidized in 99.8% pure alumina tubes than in high-purity fused quartz tubes. Thus, oxidation rates of silica formers are enhanced in water vapor due to the formation of impurity-carrying hydroxide species which contaminate the silica scale.

3.5.1.2. Intrinsic Effects of Water Vapor on Oxidation

Water vapor also intrinsically increases the oxidation rate of silica formers compared to results obtained in dry oxygen. To begin this discussion, consider again the results of Deal and Grove (1965) for silicon. As in oxygen containing environments, linear-parabolic oxidation kinetics are again observed for silicon in water vapor. Deal and Grove (1965) show that the parabolic rate constant, B is proportional to the product of the effective diffusivity of the oxidant in the silica scale, D_{eff}, and the solubility of the oxidant in the silica scale, C^*, or:

$$B=2D_{eff}C^*/N \tag{18}$$

where N is the number of oxidant molecules incorporated in a unit volume of oxide. Based on work of Norton (1961) and Moulson and Roberts (1961) for the diffusivities and solubilities of oxygen and water in silica, as well as the parabolic oxidation rates of silicon measured by Deal and Grove(1965), the following summary can be made. The effective diffusivity of water in silica is about an order of magnitude less than oxygen as shown in Figure 14. The solubility of water in silica, however, is two to three orders of magnitude higher than oxygen. Thus, the parabolic rate constant for silicon in water vapor is one to two orders of magnitude higher than in oxygen as can be seen in Figure 15. Since the solubilities of water and oxygen in silica are relatively temperature independent, (Deal and Grove, 1965; Moulson and Roberts, 1961) the temperature dependence of the parabolic rate constant in each environment reflects the enthalpy of diffusion for that oxidant species in silica. Simply put, the enhanced oxidation rates for silica formers in water vapor are due to the high solubility of water in silica.

As already discussed, it is generally concluded that the oxidation of silicon in dry oxygen is controlled by the transport of molecular oxygen through the silica scale. Likewise in water vapor, Deal and Grove (1965) concluded that transport of molecular water in silica is the rate controlling mechanism for parabolic oxidation of silicon. Molecular transport limited parabolic oxidation for silicon is demonstrated in Figure 16. The plot of parabolic rate constant versus oxidant partial pressure for both oxygen and water vapor results in a line of slope one. In separate experiments, Deal and Grove (1965) also conclude that the oxidation of silicon by water vapor is independent of the carrier gas, based on results with oxygen and argon carrier gases, demonstrating that water vapor is the primary oxidant in water vapor/oxygen mixtures.

Again, comparisons between the oxidation of SiC and Si_3N_4 in water vapor and the oxidation of Si can be made since they are all silica formers. The oxidation of SiC in water vapor has been studied extensively, however, in many of these studies, it is difficult separate effects from

impurities and those from water vapor. Several studies have been conducted for pure materials in clean water vapor-containing environments (Fung and Kopanski, 1984; Lu et al., 1984; Suzuki et al., 1982; Tressler et al., 1985). The results of each of these studies shows that SiC oxidation is accelerated in water vapor compared to dry oxygen. However, Opila (in press) has examined the oxidation kinetics of CVD SiC over a range of water vapor partial pressures, mainly in an oxygen carrier gas, but also in an argon carrier gas. These results show a number of interesting trends. First, at 1200°C bubbles are found in the amorphous scales for water vapor contents of 25% H_2O/O_2 and higher. The density of bubbles increases with water vapor partial pressure. An example of bubbles formed in a silica scale from oxidation of SiC in 90% H_2O/10% O_2 at 1200°C for 64h is shown in Figure 17. These bubbles are not observed at 1100°C nor are they observed for crystalline scales formed at 1400°C. Again, these bubbles are an effect of gaseous oxidation products formed by the reaction:

$$SiC + 3\ H_2O(g) = SiO_2 + CO(g) + 3\ H_2(g) \qquad (19)$$

Also, Figure 18 (Opila, in press) shows that the variation of parabolic rate constant with water vapor partial pressure yields a power law exponent less than one. This indicates that some ionic oxidant species contributes to the oxidation process in addition to molecular water. Finally, crystallization of the silica scale is shown to be only weakly dependent on water vapor and more strongly dependent on an impurity nucleation mechanism.

Similarly, the oxidation of Si_3N_4 has primarily been studied for materials containing sintering aids. The only study where pure Si_3N_4 has been studied in a clean water vapor-containing environment is that by Choi et al. (1989). In this study, the oxidation rate is found to depend on carrier gas and in addition, a complicated dependence on water vapor partial pressure is observed. Oxidation rates in high water vapor partial pressures are lower than rates observed in lower water vapor partial pressures. This result may be due to silica volatility which is discussed in detail below. In addition, it is not yet established whether the silicon oxynitride layer is protective in water vapor environments.

To summarize, both SiC and Si_3N_4 oxidize more rapidly in water vapor very likely due to the increased solubility of water in the silica scale. The apparent dependence of the parabolic rate constant on water vapor partial pressure is not the same as for silicon oxidation at lower temperatures, indicating more complex oxidation mechanisms are operative. This is an area that requires additional work before an in depth understanding of the oxidation mechanisms in water vapor are understood.

3.5.1.3. Silica Scale Volatility in Water Vapor

Another important effect of water vapor on oxidation of silica-forming materials is its ability to readily react with the silica scale to form volatile silicon hydroxide species. There is a substantial amount of work in the 1950's and 60's that indicated silica was volatile in water vapor containing environments although the identity of the volatile species was not known (Glemser and Wendlandt, 1963). Silica volatility was also measured more recently by Cheng and Cutler, (1979). However, it is not until recently the following formation reaction has been identified in a transpiration study by Hashimoto (1992) and confirmed by Opila et al. (1997) using mass spectrometry:

$$SiO_2 + 2H_2O(g) = Si(OH)_4(g) \tag{20}$$

The effect of silica volatility on the oxidation of silica-forming materials has also gone largely unnoticed until recently. Silicon oxidation literature contains only a few comments that there is a slight deficiency of silica formed during thermal oxidation of silicon in water vapor (Deal, 1963; Ligenza, 1962). This can be attributed to the interest in the short-term oxidation behavior of silicon.

The importance of this effect has only recently been documented for silicon carbide (Opila and Hann, 1997; Robinson et al., 1999; and Opila et al., 1999). SiC exposed to water vapor-containing environments will oxidize to form a silica scale which simultaneously volatilizes to form $Si(OH)_4$ by the above reaction. The resulting kinetics are paralinear in nature. The change in oxide thickness for a paralinear process is shown in Figure 19a and is described by the following equation:

$$\frac{dx}{dt} = \frac{k_p}{2x} - k_l \tag{21}$$

Similar expressions are developed for surface recession and weight change (Opila and Hann, 1997;Tedmon, 1966). Surface recession kinetics are shown in Figure 19a while paralinear weight change is shown in Figure 19b. At long times a steady state process is achieved in which silica is consumed at the same rate it forms resulting in a linear recession rate of SiC. Paralinear oxidation kinetics of Si_3N_4 have also recently been documented by Fox et al. (1997b). A comparison of kinetics in 50% H_2O/O_2 for SiO_2, CVD SiC, and CVD Si_3N_4 is shown in Figure 20. Silica shows a simple linear weight loss. SiC shows a larger weight gain before the weight loss than Si_3N_4 since the ratio of k_p/k_l is larger for SiC.

The volatility rate of silica, k_l, is shown by Opila and Hann (1997) in furnace studies, and Robinson and Smialek (1999) in burner rig studies, to be controlled by transport of the volatile silicon hydroxide species through a gaseous laminar boundary layer. Equation 6 gives the following expression for the volatility rate, k_l:

$$k_l = 0.664\, Re^{1/2}\, Sc^{1/3} \frac{D\rho_v}{L} \tag{22}$$

where, in this case, D is the interdiffusion coefficient of $Si(OH)_4$ in the boundary layer, ρ_v is the density of the volatile species $Si(OH)_4$ in the boundary layer, and L is the characteristic length of the test coupon. Silica volatility is dependent on pressure, temperature, and gas velocity. Rewriting Equation 22 in terms of these parameters results in:

$$k_l \propto \frac{v^{1/2}}{P_{total}^{1/2}} P_{Si(OH)_4} \tag{23}$$

The temperature dependence of the volatility rate is included in the $P_{Si(OH)4}$ term and arises from the enthalpy for reaction of Equation 20. Also, it can be seen from Equation 20 that the partial pressure of $Si(OH)_4$ increases with the square of the water vapor partial pressure. This pressure dependence has been demonstrated by Hashimoto (1992) for silica. Inserting this relationship in Equation 23, while remembering that in combustion environments the water vapor partial pressure scales with the total pressure, results in:

$$k_l \propto v^{1/2} P_{total}^{3/2} \tag{24}$$

The pressure dependence, $P^{3/2}$, has been demonstrated by Robinson and Smialek (1999) for SiC recession as shown in Figures 21 and 22. In addition, Figure 22 shows the temperature and velocity dependence for silica volatility in combustion conditions. Many proposed applications of SiC and Si_3N_4 involve high pressure and high velocity combustion environments, thus silica volatility and the corresponding substrate recession become critical life limiting processes especially for thin components.

3.5.2. Oxidation of SiC in CO_2

Another common component of gaseous environments in which silica forming materials can be used is carbon dioxide. Again this gaseous species is a product of combustion of hydrocarbon fuels. The oxidation reaction for SiC in CO_2 can be given by the following:

$$SiC + 3CO_2(g) = SiO_2 + 4CO(g) \quad (25)$$

Oxidation of SiC in this environment is much less studied than in oxygen and water vapor. Nevertheless, Antill and Warburton, (1970), Fitzer and Ebi, (1974) and Opila and Nguyen, (1998) all find that oxidation rates of SiC in pure CO_2 are much lower than in oxygen. This is shown graphically in Figure 23. While the rate limiting mechanism is unclear, it can be concluded that passive oxidation of SiC in CO_2 is negligible compared to the rates observed in oxygen or water vapor.

3.6. Cyclic Oxidation of Silica-Formers

Cyclic oxidation tests simulate the temperature cycles of actual engine mission cycles for applications such as aircraft engines. These tests subject the samples to cooling stresses which form due to thermal expansion mismatches between the substrate and the growing oxide scale. Thermal expansion curves for SiC, Si_3N_4, amorphous SiO_2, and cristobalite are shown in Figure 24. Assuming the scale is stress-free at temperature, then during cooling, compressive stresses would develop in the scale for amorphous silica, while tensile stresses would develop in the scale for cristobalite. Since most real applications of silica-formers result in at least partially crystalline scales, it is expected that the silica scale will be in tension on cooling. Cracks in the oxide may form. On reheating, the stress is relieved, the cracks heal at temperature resulting in protective behavior of the oxide. In contrast, for amorphous silica on silica-formers and typical superalloys, the scale buckles and spalls on cooling due to compressive stress formation. Thus, one expects for silica-forming ceramics, in contrast to superalloys, little difference between isothermal and cyclic oxidation rates. This has in fact been shown to be the case by Andrews and Riley, (1990), Maeda et al., (1989), Opila et al., (1993), and Park et al. (1998). Figure 25 shows typical cyclic oxidation behavior for a number of silica-forming ceramics exposed to 5h cycles at 1300°C for a total of 1000h. In general the silica growth shows fairly protective behavior. In addition, little difference in flexural strength between isothermally and cyclically exposed samples is observed (Andrews and Riley, 1990; Maeda et al., 1989).

3.7. Effect of Oxidation on Fracture Strength of Silica Formers

Oxidation of SiC and Si_3N_4 affects the fracture strength of these materials. After short oxidation times, increased fracture strengths are reported for SiC (Easler et al., 1981; Becher, 1983) and Si_3N_4 (Jakus et al., 1984). The initial formation of amorphous silica rounds existing surface flaws. At longer oxidation times, surface pits, bubble formation at the oxide/matrix interface, attack of secondary phases and grain boundary attack may all lead to flaws larger than those originally

present. Strength reductions are then observed (Easler et al., 1981; Becher, 1983, Jakus et al., 1984). The formation of these oxidation flaws is dependent on the sample purity and the oxidation temperature. Thus pure materials oxidized at lower temperatures exhibit less oxidation-induced strength degradation.

Tressler (1990) has also summarized the oxidation effects on crack growth and creep in SiC and Si_3N_4. Crack growth is generally controlled by grain boundary phases. Materials containing glassy grain boundary phases are more susceptible to crack growth than single phase materials. When oxidation increases the glassy grain boundary phase, the threshold stress intensity above which crack growth occurs decreases. Likewise, if oxidation results in a more creep resistant grain boundary phase due to crystallization or depletion of additive cations, the threshold stress intensity increases.

3.8. Volatility

3.8.1. Direct Vaporization

SiC and Si_3N_4 ceramics form vapor species via a variety of mechanisms. The simplest mechanism is direct vaporization of SiC or Si_3N_4. There are numerous vaporization studies of these compounds (Hincke and Brantley, 1930; Drowart et al., 1958; Zmbov et al., 1971). SiC vaporizes to Si(g), Si_2C(g), SiC_2(g), and Si_2(g) in vacuum; Si_3N_4 decomposes to Si(l) and N_2(g) in vacuum. However, in most applications there is some oxygen present in the atmosphere and the interaction of this oxygen with SiC and Si_3N_4 is important in determining the volatile species.

Volatility diagrams are the best way to represent the vapor species over a condensed phase (Wagner, 1958; Kohl et al., 1977; Heuer and Lou, 1990). Figure 26(a) is a simple volatility diagram for the vapor species over Si in varying oxygen potentials. Note the condensed phases in Figure 26(a). The vapor species on the left hand side are in equilibrium with Si(l) and the vapor species on the right hand side are in equilibrium with SiO_2(s). SiO(g) is the primary vapor species above Si(l) or SiO_2(s) for $P(O_2)$ from about 10^{-24} to 10^{-4} bar. Below 10^{-24} bar Si(g) becomes dominant; above 10^{-4} bar SiO_2(g) becomes dominant.

Heuer and Lou (1990) also develop volatility diagrams for SiC and Si_3N_4, shown in Figures 26(b) and 26(c), respectively. The basic difference between these and Figure 26(a) is that the activity of Si is now less than unity. The Si_3N_4 diagram also includes a region of stability for SiN_2O_2. For clarity, these diagrams only show the dominant vapor species.

3.8.2. Oxide/Substrate Reactions

As the volatility diagrams indicate, in most cases a stable SiO_2 film is present on a SiC or Si_3N_4 substrate in all but the lowest oxygen potentials. At high temperatures, the silicon dioxide scale reacts with the SiC or Si_3N_4 substrate, generating volatile species as:

$$SiC(s) + 2\ SiO_2(s) = 3\ SiO(g) + CO(g) \quad (26)$$

$$Si_2N_2O(s) + SiO_2(s) = 3\ SiO(g) + N_2(g) \quad (27)$$

Note that the reaction for Si_3N_4 has been written with the Si_2N_2O, although this intermediate layer may be variable in composition.

The formation of vapor species at the oxide/ceramic interface can be displayed with a predominance diagram and overlaid equilibrium vapor species. These are illustrated in Figures 27(a) and 27(b) for the Si-C-O and Si-N-O systems, respectively. At temperatures above 1800 K, substantial pressures can be generated at the SiC/SiO_2 interface (Jacobson et al., 1992). This is shown in a plot of P(Total) vs. temperature in Figure 28. Note that the pressure is quite significant for carbon-saturated SiC/SiO_2 and can be reduced with silicon-saturated SiC/SiO_2.

Figure 29 is a photograph of a coupon of SiC oxidized at 2073 K for 1 hr. Note the extensive bubbling. Some of this is due to the rapid oxidation rates and formation of CO(g) bubbles as an oxidation product. However some of the bubbling is very likely due to the SiC/SiO_2 interactions described above.

3.8.3. Active Oxidation

The most common route for silica-forming ceramics to vaporize is active oxidation. Silica is a unique protective oxide in that it has a stable gaseous suboxide. Its stability is comparable to that of $SiO_2(g)$ (Chase et al., 1986):

$$\tfrac{1}{2}\ Si + O_2(g) = \tfrac{1}{2}\ SiO_2(g) \quad \Delta G^\circ_{1500\,K} = -322\ kJ/mol \quad (28)$$

$$Si + \tfrac{1}{2}\ O_2(g) = SiO(g) \quad \Delta G^\circ_{1500\,K} = -227\ kJ/mol \quad (29)$$

Consider a bare silicon surface. At low partial pressures of oxygen, there is sufficient oxygen to form SiO(g), but insufficient oxygen to form a stable $SiO_2(s)$ film. This is termed 'active oxidation'

and can lead to substantial material consumption. At higher partial pressures of oxygen, a stable SiO_2(s) film forms. This situation is termed 'passive oxidation'.

The theoretical and experimental aspects of active oxidation have been nicely summarized in a recent overview (Narushima, et. al, 1997). There are several approaches to calculating the oxygen partial pressure at which the active-to-passive transition occurs. Before discussing this issue it is important to recognize that the active-to-passive transition and the passive-to-active transition are different. The former is attained by gradually increasing oxygen pressure over a bare Si, SiC, or Si_3N_4 to the point where SiO(g) is no longer dominant and a stable SiO_2 film forms; the latter is attained by gradually decreasing oxidant pressure over a SiO_2-protected surface to the point where SiO(g) formation dominates. These transitions occur at partial pressures of oxygen that differ by several orders of magnitude.

Wagner (1958) was the first to approach these transitions for pure silicon. Wagner's (1958) approach is based on the condition for Si/SiO_2 equilibria. This concept has been extended to SiC and Si_3N_4 (Singhal, 1976c). In the active region, a flux of oxygen atoms strikes the SiC surface and reacts to form SiO(g) and CO(g).

$$SiC + O_2(g) = SiO(g) + CO(g) \tag{30}$$

As pressure is increased, the resultant flux of SiO(g) and CO(g) increase. Eventually, there is sufficient SiO(g) and CO(g) so that SiC and SiO_2 can co-exist in equilibrium as shown in the equations below. The exact condition for SiC and SiO_2 equilibrium has been an issue of some controversy. There are three possibilities:

$$SiC(s) + 2\ SiO_2(s) = 3\ SiO(g) + CO(g) \tag{31}$$

$$SiC(s) + SiO_2(s) = 2\ SiO(g) + C(s) \tag{32}$$

$$2\ SiC(s) + SiO_2(s) = 3\ Si(l,s) + 2\ CO(g) \tag{33}$$

In order to determine when the necessary P(SiO) and/or P(CO) is attained, the flux of O_2(g) striking the surface must be examined. The relevant diagram is Figure 30(a). The flux of oxygen is written in terms of oxygen atom flux for clarity in mass conservation.

$$J_O^{incident} = 2D_{O_2}\frac{p^o_{O_2}}{\delta_{O_2}RT} \tag{34}$$

The resultant fluxes of SiO(g) and CO(g) emerging from the surface are given by :

$$J_{SiO}^{reaction} = D_{SiO}\frac{p^{\bullet}_{SiO}}{\delta_{SiO}RT} \tag{35}$$

$$J_{CO}^{reaction} = D_{CO} \frac{p_{CO}^{*}}{\delta_{CO} RT} \tag{36}$$

Here J is the flux of the subscripted species, D is the diffusion coefficient of the subscripted species, p is the pressure of the subscripted species, δ is the thickness of the boundary layer, R is the gas constant and T is the absolute temperature. In the case of p^*, this is the pressure calculated from the above equilibria. Thus the transition pressure is:

$$p_O^{transition} = \left(\frac{D_{SiO}}{D_{O_2}}\right)\left(\frac{\delta_{O_2}}{\delta_{SiO}}\right) p_{SiO}^{*} = \left(\frac{D_{SiO}}{D_{O_2}}\right)^{1/2} p_{SiO}^{*} \tag{37}$$

$$p_O^{transition} = \left(\frac{D_{CO}}{D_{O_2}}\right)\left(\frac{\delta_{O_2}}{\delta_{CO}}\right) p_{CO}^{*} = \left(\frac{D_{CO}}{D_{O_2}}\right)^{1/2} p_{CO}^{*} \tag{38}$$

The relationship between diffusivities and boundary layer thickness allows the above simplification. It is generally agreed that the second equation more closely describes the active-to-passive transition for SiC.

Next consider Wagner's (1958) calculation of the oxygen partial pressure at the passive-to-active transition. The passive-to-active transition begins with a stable SiO_2 film. As oxygen potential is lowered, this SiO_2 film decomposes and eventually active oxidation begins. Wagner (1958) derives the passive-to-active transition from the decomposition of SiO_2:

$$SiO_2(s) = SiO(g) + \tfrac{1}{2}\, O_2(g) \tag{39}$$

When the partial pressure of oxygen is low enough, SiO_2 decomposes and is no longer stable. This marks the beginning of active oxidation. For SiC, the active-to-passive and passive-to-active transition differ by about four orders of magnitude.

More recently, a purely thermodynamic approach has been developed, based on the volatility diagrams illustrated in Figures 26(a-c). Heuer and Lou (1990) modify the original volatility diagram of Wagner (1958) in this approach. The modifications include the representation of only the dominant volatile species and inclusion of an equimolar $P(O_2) = \tfrac{1}{2}\, P(SiO)$ line. A lower and upper limit for the active-to-passive transition can then be calculated. (Heuer and Lou, 1990 and Schneider, 1995). The lower limit is from a modification of Turkdogan's theory of enhanced vaporization of metals in reactive gas streams (Turkdogan, 1963) and is illustrated in Figure 30(b). The Turkdogan theory is based on a metal vaporizing into a gas stream, reacting to form a metal oxide 'fog' in the gas, and condensing. In the case of Si, SiC, or Si_3N_4 the vapor pressure of Si(g), Si-C gas species or Si-N gas species are much too low to have much effect; however the SiO(g) can form appreciable vapor pressures at low oxygen potentials. If a bare SiC surface is actively

oxidizing, SiO(g) diffuses outward from the sample. At the point when $P(O_2) = ½ P(SiO)$, then the following reaction in the gas phase occurs:

$$SiO(g) + ½ O_2(g) = SiO_2(smoke) \quad (40)$$

The point at which $P(O_2) = P(SiO)$ can be determined from the intersection of the equimolar line with the P(SiO) line in Figures 26(b-c). Some of the smoke will condense on the SiC surface and this is the onset of passive oxidation. This lower-limit transition is very similar to the passive-to-active transition derived by Wagner (1958), but does not contain the small corrections due to mass transport.

An upper limit for the active-to-passive transition can also be derived from a volatility diagram (Schneider, 1995). Going back to Wagner's criteria that enough SiO(g) must form to satisfy the equilibria:

$$\underline{Si} + SiO_2 = 2SiO(g) \quad (41)$$

The underline indicates the activity of silicon is unity (pure silicon) or less (SiC or Si_3N_4). This equilibrium pressure of SiO is given by point T in the volatility diagrams of Figures 26(a-c). The amount of $O_2(g)$ necessary to produce SiO(g) for the above equilibrium is determined from:

$$Si + ½ O_2 = SiO(g) \quad (42)$$

This upper limit for active oxidation is thus found at the intersection of the eqimolar line (due to the stoichiometry of the above equation) and a horizontal line drawn from the SiO(g) pressure at point T. Note that this particular point has no physical meaning. It is simply a convenient way of reading the proper $P(O_2)$ from the graph. Again, this is similar to the Wagner active-to-passive transition without the small correction for mass transport effects.

Figure 31 summarizes these approaches and some experimental data (Narushima et al., 1997). The experimental data exhibit considerable spread, likely due to morphology and mass-transport effects (Hinze and Graham, 1976) which are not fully incorporated into the current models.

The above discussion has focused on oxygen as the primary oxidant in determining the active-to-passive and passive-to-active transition. There are studies in the measurement of the active-to-passive transition in H_2O/H_2 (Kim and Readey, 1987) and CO_2/CO (Narushima et al., 1993b). It has been shown that these are equivalent to the oxygen cases with H_2O and CO_2 acting as the primary oxidant, respectively (Opila and Jacobson, 1995).

3.9. Molten Salt Corrosion

In combustion environments sodium impurities are very common. These can lead to highly corrosive salt deposits. An example is ingested NaCl in combustion air, which reacts with sulfur impurities in the fuel to form highly stable Na_2SO_4 (Jacobson, 1989):

$$2\ NaCl\ (v) + SO_3(g) + H_2O(g) = Na_2SO_4(l) + 2\ HCl(g) \qquad (43)$$

The sodium may come from a marine environment in a gas turbine, process chemicals in an industrial furnace, or even fuel impurities. Under the appropriate conditions, Na_2SO_4 forms as a condensed phase, depositing on parts. Figure 32 shows the calculated dew points for Na_2SO_4 deposition. The rates of deposition are also critical and have been treated in detail (Stearns et al., 1983).

Deposition of corrosive salts is a continuous process. It is difficult to simulate this in a laboratory furnace. For this reason many salt corrosion studies are done by seeding a flame in a burner rig. Figure 33 is a comparison of SiC treated in a burner without salt and with a flame seeded with NaCl. Note the extensive corrosion in the latter case.

These processes are best interpreted with the acid/base theory of oxides (Rapp, 1986; Jacobson, 1993). Na_2SO_4 decomposes to Na_2O, which is the key reactant:

$$Na_2SO_4(l) = Na_2O(s) + SO_3(g) \qquad (44)$$

The partial pressure of $SO_3(g)$ [or $SO_2(g) + O_2(g)$] effectively sets the activity of $Na_2O(s)$. A high activity of Na_2O is a basic molten salt; a low activity of Na_2O is an acidic molten salt. Since SiO_2 is an acidic oxide, it is readily attacked by a basic oxide:

$$2\ SiO_2(s) + Na_2O = Na_2O{\cdot}2(SiO_2)\ (l) \qquad (45)$$

This reaction describes the process which leads to the thick, glassy product in Figure 33. The solid protective SiO_2 layer has been replaced by a liquid, non-protective sodium silicate layer. The liquid layer permits rapid diffusion of oxygen inward and carbon monoxide outward, resulting in accelerated oxidation. This provides more silica for the above reaction and leads to rapid consumption of SiC.

The necessary conditions for the silica reaction with Na_2O follow from basic chemical thermodynamics (Jacobson, 1989). Assuming unit activities for SiO_2 and $Na_2O{\cdot}2(SiO_2)$, the threshold Na_2O activity [$a(Na_2O)$] for SiO_2 dissolution can be calculated:

$$a(Na_2O) = \exp(-\Delta G^\circ/RT) \tag{46}$$

Here ΔG° is the free energy for reaction (45) above. At 900°C, the minimum $a(Na_2O)$ is 10^{-11}, meaning any activity greater than this will lead to silicate formation. Since the $a(Na_2O)$ is set by the partial pressure of $SO_3(g)$, this means that a $P(SO_3)$ of 5×10^{-5} bar or less will lead to silicate formation.

Some of these predictions have been verified in a burner using different sulfur levels in the fuel to set a partial pressure of $SO_3(g)$. These results are shown in Figure 34 for quartz coupons heated in a low sulfur fuel (0.05%) and high sulfur fuel (0.5%). The first set of coupons was exposed to a low partial pressure of SO_3 and hence a more basic salt. Figure 34(a) shows there is clear evidence of more corrosion and chemical analysis revealed sodium silicate. The second set of coupons was exposed to a higher partial pressure of SO_3 and hence a more acidic salt. Figure 34(b) indicates less product formation and chemical analysis indicated no sodium silicate formation.

The preceding example illustrates the chemistry for Na_2O reactions with pure silica. Actual applications are more complex since additional elements may alter the basicity of the oxide. In the case of silica-forming ceramics, carbon is especially important. Carbon is a constituent of SiC, excess carbon may be added as a sintering aid, and carbon is often used as a fiber coating in fiber reinforced composites. In order to understand the effect of carbon, the following electrochemical cell was used to measure $a(Na_2O)$ (Watt et al., 1981 and Jacobson, 1989):

$$Pt,\ O_2(r)|ZrO_2|Na_2SO_4,\ SO_3|mullite|10\ m/o\ Ag_2SO_4,\ Na_2SO_3,Ag \tag{47}$$

Zirconia acts as a membrane for oxide anions and mullite acts as a membrane for sodium cations. The $O_2(r)$ is the oxygen reference and the Ag_2SO_4/Na_2SO_3 is the Na_2O reference. The net reaction is thus:

$$Na_2O + Ag_2SO_4 = 0.5\ O_2(g) + Na_2SO_4 + 2\ Ag \tag{48}$$

Using the Nernst Equation, $a(Na_2O)$ can be determined from the cell voltage (E) and the free energy change for the above reaction. At 900°C, for example, $a(Na_2O)$ is given by:

$$E = 1.498 + 0.116 \log a(Na_2O) \quad (49)$$

Figure 35 shows $a(Na_2O)$ measurements taken for $Na_2SO_4/(0.01\ SO_2/O_2)$ and $Na_2SO_4/(0.01\ SO_2/O_2)$ + carbon. Note, addition of carbon makes the melt swing strongly basic. This very likely occurs due to the formation of sodium sulfide and the subsequent formation of excess Na_2O:

$$Na_2SO_4(l) + C = Na_2S + 2\ CO_2 \quad (50)$$

$$Na_2S + 3\ Na_2SO = 4\ Na_2O + 4\ SO_2 \quad (51)$$

The fact that carbon drives Na_2SO_4 more basic explains why SiC corrodes more readily in molten salts than Si_3N_4. It also explains why excess carbon in a ceramic promotes corrosion.

Once basic Na_2O begins to react with SiO_2, this process continues until all of the available Na_2O is consumed. In a combustion situation where sodium is ingested from the air, there is an essentially infinite supply of sodium and it is possible for a large amount of the ceramic to be consumed. In a situation where the supply of sodium is limited, the reaction will stop at some composition given by the liquidus Na_2O-SiO_2/SiO_2 line on the Na_2O-SiO_2 phase diagram. A layered Na_2O-$SiO_2(l)$-$SiO_2(s)$ structure will result (Mayer and Riley, 1978 and Jacobson, 1986). This is shown in Figure 36.

The reactive species, Na_2O, can form from other salts as well. Na_2CO_3 readily decomposes:

$$Na_2CO_3 = Na_2O + CO_2 \quad (52)$$

In fact, Na_2CO_3 decomposes more readily than Na_2SO_4 and creates a more basic molten salt. McNallan et al. (1990) have shown that Na_2O can also form from the reaction of NaCl and water vapor:

$$2\ NaCl + H_2O = Na_2O + 2\ HCl \quad (53)$$

In addition to Na_2O, other oxides can potentially attack the protective SiO_2 film. Sea salt leads to $MgSO_4$ and $CaSO_4$ deposits as well as Na_2SO_4 deposits. This mixed sulfate can be described by molten salt solution models (Pelton, 1983; Bornstein, 1996) and leads to magnesium, calcium, and sodium silicates (Fox, 1998). Many fuels contain vanadium impurities. V_2O_5 is an acidic oxide and thus does not react directly with SiO_2. However, it accelerates Si_3N_4 oxidation, possibly due to the solubility of SiO_2 in V_2O_5 (Lamkin, et. al, 1990).

Similar principles apply to molten slags, which are complex mixtures of oxides. Here it is more difficult to define basicity, however a useful index has been the weight percent ratio of basic to acidic oxides. These are the basic and acidic oxides commonly encountered (Ferber and Tennery, 1983, 1984):

Basic Oxides: Na_2O, K_2O, MgO, CaO, Fe_2O_3

Acidic Oxides: SiO_2, Al_2O_3, TiO_2

The basic slags clearly degrade silica-forming materials more readily than the acidic slags. In a locally low partial pressure of oxygen, metal silicides may form (Ferber and Tennery, 1984).

It has been shown that molten salt-induced corrosion can lead to substantial attack of SiC and Si_3N_4. It is important to discuss the influence of this corrosion on microstructure and mechanical properties. Figure 37 illustrates the surface of as-received SiC (with B and C additives), the glassy coating after corrosion in Na_2SO_4, and then after cleanly removing the glassy coating with hydrofluoric acid. The last step reveals a highly pitted structure as opposed to the dense starting material. The reasons for this non-uniform attack are very likely due to structural discontinuities (e.g. grain boundaries, dislocations, etc.) in the SiC and bubble formation in the corrosion reactions (Jacobson and Smialek, 1986). Microstructural examination clearly indicates enhanced attack near grain boundaries, but also a correlation between the larger pits and bubbles in the silicate. A proposed mechanism for this is illustrated in Figure 38.

The strengths of monolithic ceramics are highly dependent on surface finish. Thus the pitting observed in Figure 37(c) is expected to lead to a strength decrease. Depending on the salt chemistry, which in turn determines the degree of pitting, room temperature strength reductions of up to 50% have been observed (Smialek and Jacobson, 1986; Jacobson et al., 1986; Fox and Smialek, 1990). In nearly all cases the fracture origins were the corrosion pits.

3.10. Refractory Oxide Coatings on Silica-Forming Ceramics

One possible solution to the corrosion problems of silica-forming ceramics is the application of a refractory oxide coating. Refractory oxides are generally more chemically inert than SiC and Si_3N_4 and this approach should combine the best properties of both materials. There are a number of important considerations in the application of a coating. The first is a good match between coefficients of thermal expansion (CTEs) and the SiC or Si_3N_4 substrate. Table II lists CTEs for SiC, Si_3N_4, and several refractory oxides. Note the remarkably close match of SiC and mullite.

Mullite coatings on SiC were first developed by researchers at Solar Turbines (Price, 1992) and further refined at the NASA Lewis Research Center (Lee et al., 1988, 1989). Critical issues are substrate surface roughening for adherence and application of fully crystalline mullite. Figure 39 shows a mullite coating on a SiC substrate.

Mullite-coated SiC exhibits substantially improved behavior in Na_2SO_4-induced corrosion as compared to uncoated SiC (Jacobson et al., 1996). This is due to the formation of higher melting sodium-alumino-silicates, as opposed to the low melting sodium silicates discussed in the section 3.9. above. However, in time, sodium penetrates the mullite coating and forms sodium silicate at the mullite/SiC interface. In the case of water vapor containing environments, mullite coatings offer limited benefits as the silica activity is only 0.4. Hence silica is readily volatilized from mullite by water vapor (Lee et al., 1989).

Other refractory oxide coatings are also candidates, however the problem of CTE mismatch must be considered (Table II). Graded coatings may be a possibility. Stability of the coating/substrate interface is also a critical issue.

4. Oxidation of Alumina-Forming Non-oxides

From Figure 1 it can be seen that after silica forming materials, those materials with the next most protective oxide scale would be alumina formers. Since alumina scales are less sensitive to impurities, AlN and Al_4C_3 appear, at first glance, to be ideal high temperature oxidation resistant materials. However, the recession rates in this figure are based on those observed for alumina forming metal alloys. Oxidation of both of these ceramic materials results in the formation of gaseous products which can alter the protective qualities of the alumina scale.

4.1. Oxidation of AlN

As previously mentioned the oxidation of AlN is complex since nitrogen gas is generated, as shown in the following reaction:

$$2AlN + 3/2\ O_2(g) = Al_2O_3 + N_2(g) \qquad (54)$$

The literature contains many discrepant reports on both the rate controlling oxidation mechanism as well as the oxidation rate. Including only the results for dense bulk AlN, the oxidation behavior of AlN can be summarized as follows. In general, the oxidation kinetics of AlN in dry air (Sato et al., 1987) or dry oxygen (Jones and Scott, 1989; Kuromitsu et al., 1992; Opila et al., 1998) were parabolic. The oxidation rate was found to be similar to that for alumina formation on NiAl (Opila

et al., 1998) as shown in Figure 40. Thus the rate controlling mechanism was concluded to be the same, i.e., oxidation rates are limited by transport of aluminum and/or oxygen through the α-alumina scale by short circuit paths such as grain boundaries. In laboratory air (Bellosi et al., 1993; Robinson and Dieckmann, 1994), wet air (Sato et al., 1987; Kim and Moorhead, 1994) or wet oxygen (Kuromitsu et al., 1992; Opila et al., 1998), however, the oxidation kinetics were much faster and generally linear in nature at temperatures below about 1200 to 1300°C. Typical weight change kinetics for AlN in 10% H_2O/90% O_2 are shown in Figure 41. At higher temperatures in wet air, kinetics were again parabolic (Sato et al., 1987; Kim and Moorhead, 1994). Oxidation rates were found to increase with water vapor content (Kuromitsu et al., 1992; Sato et al., 1987; Kim and Moorhead, 1994). It was concluded that oxidation in even small amounts of water vapor by the reaction

$$2AlN + 3H_2O(g) = Al_2O_3 + N_2(g) + 3H_2(g) \quad (55)$$

results in the formation of micropores (Sato et al., 1987; Opila et al., 1998; Azema et al., 1991) 20-100 nm in diameter, at temperatures below 1200-1300°C. A typical fracture section of the alumina scale from AlN exposed in 10% H_2O/90% O_2 at 1200°C for 48h is shown in Figure 42. For these high porosities, transport of the oxidant through the micropores is rapid and oxidation is limited by the surface reaction between AlN and the oxidant, hence the observed linear kinetics. At higher temperatures the scale becomes denser due to sintering of the micropores and the observed oxidation kinetics become parabolic once again. Thus, the oxidation rate of AlN under very dry conditions is parabolic and quite low, but at water vapor contents typical of normal humidity levels in air, rapid linear oxidation occurs.

4.2. Oxidation of Al_4C_3

While the oxidation of Al_4C_3 has not been studied nearly as much as AlN there are indications its oxidation resistance is similar. LeFort and Marty (1989) report that a nonprotective α-Al_2O_3 scale is formed on Al_4C_3 powder. The oxide scale was found to be severely cracked. Gas generation during oxidation may again explain the nonprotective nature of this oxide.

5. Boria forming Ceramics

Most borides actually form a mixed boria-metal oxide scale and will be discussed in Section 7.1.1. However, boron nitride (BN) and boron carbide (B_4C) form a pure boria scale. BN has been used for many years as a crucible material in vacuum and is of recent interest as a fiber coating for continuous fiber reinforced ceramic matrix composites. The most common form of BN is a

hexagonal, graphite-like structure. This discussion will be confined to oxidation of hexagonal BN. In pure oxygen BN oxidizes as:

$$2\ BN(s) + 3/2\ O_2(g) = B_2O_3(l) + N_2(g) \qquad (56)$$

Some $NO_2(g)$ has been detected (Pechentkoyskaya and Nazarchuk, 1981, Jacobson et al. 1999), but N_2 is likely the primary gaseous product. In pure oxygen, oxidation of BN becomes significant above about 800°C (Podobeda et al., 1976).

Boria is not a desirable protective oxide. It has a low melting point (410°C) and tends to be very reactive with water vapor, forming a number of stable $H_xB_yO_z(g)$ compounds (Chase et al. 1986). There are a number of oxidation studies of BN in the literature and the results indicate complex behavior (Lavrenko and Alexeev, 1986; Oda and Yoshio, 1993; Jacobson et al., 1999a). A recent study of BN indicates that oxidation behavior is quite dependent on structure of the starting BN material and water vapor content in the gas stream (Jacobson et al., 1999a). The first point is illustrated in Figure 43. Three types of BN—a CVD material deposited at a low temperature (Figure 43a), a CVD material deposited at a high temperature (Figure 43a), and a hot pressed material (Figure 43b) —are shown. Note the very different oxidation behavior. This is attributed to the differences in porosity and oxygen content of the various types of BN. These factors may provide rapid access for oxygen into the internal surfaces of the BN material, leading to more extensive oxidation. It also important to note that oxidation kinetics of BN are sensitive to crystallographic orientation, as observed by several investigators (Oda and Yoshio, 1993; Jacobson et al., 1999a).

Figure 44 shows the vapor species above B_2O_3 in an oxygen/10% H_2O environment. Note that the hydroxide species exhibit substantial vapor pressures. Thus in water vapor containing environments, BN is expected to volatilize via B_2O_3 and $H_xB_yO_z(g)$ species.

Boron carbide (B_4C) is an interesting ceramic due to its high hardness and strength. It also forms a B_2O_3 scale on oxidation and thus behaves similarly to BN (Gogotsi and Lavarenko, 1992). As with BN, oxidation of B_4C becomes significant above about 600°C and rapid oxidation occurs above 1200°C (Lavrenko et al., 1976). During oxidation, carbon is depleted in the B_4C region near the oxide/ceramic interface. This contributes to an oxidation-induced decrease in hardness after the B_2O_3 scale is removed (Lavrenko et al., 1976).

6. Transition Metal Carbides and Nitrides

The transition metal carbides and nitrides have a number of important properties including hardness, wear resistance, and high temperature strength. However, these carbides and nitrides do not form oxides with low oxygen diffusivities. There is also generally a large thermal expansion mismatch between metal carbides and their corresponding oxides, leading to scale cracking and the formation of easily accessible paths for oxygen inward. In addition, porous oxide scales may form with rapid gas diffusion paths inward. These factors all lead to rapid oxide growth rates. The major features in the oxidation of these materials will be discussed.

Often there is a stable oxycarbide or oxynitride formed between the oxide layer and the corresponding carbide or nitride. In the case of the carbides, the carbon may be liberated in a number of different forms. In some cases, free carbon is observed in the oxide scale. In other cases, all the carbon is oxidized to CO or CO_2. In the case of the nitrides, the liberated nitrogen escapes as NO_x or N_2.

6.1. Transition Metal Carbides

Now consider some specific carbides. Table III lists the stable transition metal carbides (Storms, 1967). The carbides to the right of these tend to form carbon/metal triple bonds, whereas the carbides to the left of these are of very low stability. Currently there is the most interest in ZrC, HfC and TaC as high temperature materials, due to their extremely high melting points. These materials are under consideration for rocket thrusters (Patterson et al., 1996) and ZrC is important in nuclear applications (Rama Rao and Venugopal, 1994).

Shimada and co-workers (1990, 1995, 1997) have extensively studied the oxidation of ZrC powders and single crystals at temperatures from 380-600°C at reduced oxygen pressures. Consider powder oxidation first. In the early stages of oxidation, oxycarbide forms. ZrC can have up to 60% of its interstitial positions occupied by oxygen. This is followed by nucleation of ZrO_2 on the oxycarbide. At higher temperatures, ZrO_2 grows rapidly and the associated volume expansion leads to cracking. Single crystals show a similar mechanism, shown schematically in Figure 45. At short times, an amorphous layer of ZrO_{2-x} grows parabolically (diffusion control). This is oxygen-deficient zirconia and the low oxygen potential allows free carbon to be deposited in the scale. Then the outer layers are oxidized to cubic zirconia and zone (2) starts to form linearly with time (interface control). This zone contains less free carbon and numerous cracks.

There are two important points from the above observations—the formation of free carbon in the oxide scale and the formation of cubic zirconia. In order for free carbon to precipitate, the oxygen pressure must be very low, as determined from the following reaction:

$$ZrC(s) + O_2(g) = ZrO_2(s) + C \quad (57)$$

Thus at 600°C, for the above reaction to be satisfied, $P(O_2)$ is 4×10^{-44} bar. If oxygen-deficient ZrO_{2-x} is formed, these extremely low oxygen potentials are possible. The formation of cubic zirconia at these low temperatures is surprising since it is not expected to be stable until 1590°C in a pure Zr-O system (Levin and McMurdie, 1975). However it has been shown that the cubic phase is stabilized in oxygen-deficient zirconia with carbon (Wang and Liang, 1998).

At higher temperatures, ZrC oxidizes at much more rapid rates. Kuriakose and Margrave (1964) report that the type of ZrC they examined is destructively oxidized above 652°C. However, Voitovich and Pugach (1973) observe little weight change until about 700°C. Clearly the form of the starting ZrC material must play a role in its oxidation behavior. At 800°C Voitovich and Pugach (1973) observe a two phase scale with a distribution of carbon in ZrO_2. At 1000°C the scale becomes more porous, at 1100°C a thin layer of carbon is observed at the ZrC/ZrO_2 interface. They also report the presence of cubic zirconia, which apparently is stabilized by carbon. At 1200°C, sintering of the scale is observed, which is surprising at these temperatures. At this high temperature, no free carbon is observed in the scale.

Currently, there is a good deal of interest in HfC for rocket thrusters (Patterson, 1996). Shimada et al. (1997) have examined the oxidation of HfC from 600 to 900°C. There are many similarities to ZrC oxidation. A two zone structure is formed where the inner layer forms with diffusion-controlled kinetics and the outer layer forms with interface-controlled kinetics. Unlike ZrC oxidation, only the monoclinic form of the product oxide (HfO_2) is observed. Carbon is observed in both layers (Shimada, 1999). At temperatures of 1400-2100°C Bargeron et al. (1993) also observed a multi-layer product structure. In this case the outer layer contained no carbon.

Courtright et al. (1991) have observed the formation of porous oxide scales on HfC and PrC at high temperatures. At temperatures of 1200 to 1530°C, Holcomb and St. Pierre (1993) have applied a counter-current diffusion model for carbon oxidation through this porous oxide. This is based on the two-step oxidation of carbon in the HfC, as shown in Figure 46 and the following reactions:

$$HfC(s) + 3\ CO_2(g) = HfO_2(s) + 4\ CO(g) \quad (58)$$

$$4\ CO(g) + 2\ O_2(g) = 4\ CO_2(g) \quad (59)$$

This two step oxidation is necessary due to the thermodynamic incompatibility of CO and O_2, which requires CO_2 to be the oxidant. They set up the necessary flux equations for each region and derive concentration profiles and parabolic rate constants. As expected for gas-phase

diffusion control, the temperature dependence is weak. Agreement between the model and measured rate constants is good.

The oxidation of other carbides, such as TiC, NbC, and TaC have also been studied. A two-layer oxide scale has also been observed on TiC (Voitovich, 1997; Shimada, 1996; and Shimada, 1999). Shimada (1996) has examined the oxidation of TiC powders as a function of temperature. Oxidation begins at about 300°C with the formation of TiC_xO_{1-x}. At higher temperatures anatase is formed and CO_2 is evolved. As temperatures approach 900°C, oxidation of the powder is nearly complete and rutile is observed. More recently Shimada (1998) has studied oxidation of single crystal TiC isothermally and observed a two layer product scale with carbon in the oxide film. Voitovich (1997) reports several reaction stages with initial parabolic kinetics followed by linear kinetics. He reports an inner layer composed of TiO, Ti_2O_3, and TiO_2 and an outer layer of TiO_2.

Recently Desmaison-Brut and co-workers (1997) have examined the oxidation of TaC and Ta_2C between 750 and 850°C. The TaC oxidizes directly to Ta_2O_5, whereas the Ta_2C forms Ta_2O_5 and an intermediate layer of tantalum oxycarbide. They attribute the different reaction rates and activation energies observed for Ta_2C as opposed to TaC to the formation of oxycarbide on Ta_2C.

As discussed in the Section 2, Gozzi and co-workers (1997) have reported on a novel method of following oxygen uptake in a refractory carbide oxidation reaction with a yttria-stabilized zirconia sensor. They use low oxygen pressures (~10^{-5} bar) and their approach is extremely sensitive to small changes in oxygen. They are able to follow oxygen incorporation into a carbide lattice at low temperatures. Interestingly at temperatures of about 400°C, the refractory carbides (Table II) behave very similarly, indicating behavior is controlled by the carbon sublattice.

6.2. Transition Metal Nitrides

Formation of oxynitride layers between transition metal nitrides and their corresponding oxides is common (Douglass et al., 1996). Voitovich and Pugach (1975) attribute the better oxidation resistance of HfN as compared to ZrN to differences in the structure of the oxynitride layer. The oxynitride formed on ZrN contains more vacancies than that formed on HfN. They also observe cubic ZrO_2 at low temperatures (500°C)—apparently stabilized by the oxygen-deficient zirconia and nitrogen in the system. Desmaison et al. (1976) have also observed a mixture of monoclinic zirconia and a mixture of cubic or tetragonal zirconia. Their kinetics and morphology observations indicate the oxidation of ZrN is controlled by an interfacial chemical reaction.

There is interest in TiN both as a wear-resistant material and as a diffusion barrier in electronics.

TiN exhibits a range of non-stoichiometry, with different compositions showing different oxidation mechanisms (Desmaison et al., 1979). However it is reported to have better oxidation resistance than ZrN or HfN (Voitovich and Pugach, 1975). The TiO_2 scale forms in layers with pores and tends to exfoliate (Desmaison et al., 1979), leading to complex oxidation kinetics. Tampieri and co-workers (1991) report varying oxidation kinetics, depending on the temperature range. At temperatures of 700-800°C parabolic kinetics suggest diffusion control and at higher temperatures diffusion through micro-cracks in the scale becomes important.

There is interest in TaN as a thin film resistor in the electronics industry. A range of oxidation kinetics and morphologies have been reported (Ibidunni, 1993; Bouzouita et al., 1983, 1987, 1988). In one case tantalum oxynitride is reported, in some cases porous scales are reported. These differences are partially due to oxidizing gases (O_2, CO_2/CO, or air) and may also be due to differences in the starting materials.

7. Oxidation of Ceramics Forming Multi-Component Scales

Thus far, the oxidation/corrosion behavior of materials which are nominally single phase, and form scales which are nominally single phase oxides has been discussed. In practice, composite materials are often desired to enhance mechanical properties or to improve other properties of the materials such as thermal conductivity, electrical conductivity, as well as oxidation resistance. In these cases, multi-phase materials are developed to enhance the desired properties. When these materials are subjected to high temperature oxidizing environments, the resulting oxidation products are also more complex. In general oxidation results in three classes of scales: mixed oxides, compound oxides, or solution oxides. Examples of each will be discussed below. In addition, fiber reinforced composites are a special class of composite materials in which an interphase material is required between the fiber and the matrix to provide the required fracture toughness. The unique issues with these materials will also be discussed.

7.1. Mixed Oxide Scales

7.1.1. Transition Metal Borides

This section reviews the oxidation behavior of HfB_2, ZrB_2, and TiB_2. HfB_2 and ZrB_2 as well as their oxides, HfO_2 and ZrO_2, are ceramics with capability for short-time use at ultra-high temperatures for applications such as rocket engine components and re-entry shields. TiB_2 is of interest for its high hardness, high melting point, and especially its good electrical and thermal conductivity. Applications of TiB_2 include coatings resistant to liquid metals and wear resistant parts. Unlike transition metal carbides and nitrides, the oxidation of transition metal borides can result in a two

phase scale consisting of boria in addition to the transition metal oxide. In general, at low temperatures and short times the borides have lower parabolic oxidation rates because transport of oxidant now occurs through a liquid boria phase rather than through the gas phase. The oxidation resistance of several transition metal diborides have been ranked by Kaufmann et al. (1967) in order of decreasing oxidation resistance as follows: HfB_2, ZrB_2, TiB_2, TaB_2, NbB_2.

The oxidation of borides is complex for a number of reasons. First, consider the formation of liquid boria. It is well known that boria is very volatile, forming both $B_2O_3(g)$ (Soulen et al., 1955) and volatile hydroxide species (Margrave, 1956; Meschi et al., 1960). At temperatures where the volatility of boria is readily observed, oxidation kinetics will therefore follow a paralinear rate law in which oxidation weight gains occur simultaneously with boria volatilization. At temperatures below 1000°C, both Irving and Worsley (1968) and Courtois et al. (1993) find protective oxidation behavior of TiB_2 attributed to a liquid boria film. A layered oxide is observed at these temperatures and is shown schematically in Figure 47. At temperatures higher than 1000°C, Courtois et al. (1993) observe paralinear behavior due to boria formation and volatilization. At these temperatures, Irving and Worsley (1968) observe that boria is volatilized as soon at is formed and the titania layer controls the oxidation kinetics. Tripp and Graham (1971) developed an experimental TGA technique for oxidation of ZrB_2 which measures each component of the paralinear kinetics: consumption of oxygen, weight change due to boria volatility, as well as total sample weight change. Typical results are shown in Figure 48. At higher temperatures, the boria will volatilize as soon as it is formed leaving only a porous transition metal oxide scale, just as in the case of carbides and nitrides. Parabolic kinetics may still be observed, but the rate limiting step is gas phase diffusion in the pores rather than diffusion through a condensed phase. In other cases, at high temperatures and low pressures, boiling boria may rupture the transition metal oxide scales resulting in linear oxidation rates controlled by the chemical reaction at the scale/matrix interface.

Other complications for oxidation of transition metal borides at high temperatures, where boria no longer offers protection, result from the properties of transition metal oxides. The monoclinic to tetragonal phase transition for zirconia and hafnia is accompanied by a volume changes which results in less protective scales (Berkowitz-Mattuck, 1966; Kaufmann et al.,1967). In addition, the titania grown on TiB_2 is usually highly textured and cracked resulting in linear kinetics at longer times (Tampieri and Bellosi, 1993).

7.1.2. Oxidation of Complex Systems Resulting in Mixed Oxide Scales

While any number of complex mixtures of non-oxide ceramics can be formulated and studied with regard to their oxidation resistance, one hopes to obtain a material whose oxidation properties are dominated by the most protective oxide in the system. However, for this to occur, a continuous layer of this oxide must be formed in the scale, otherwise the oxidation rates are controlled by less protective oxides, gas phase diffusion, or the linear reaction rate of oxidant with the matrix. Only several systems of particular note will be discussed here. In the first of these systems, Si-containing material, e.g. SiC, additions are made to less oxidation-resistant materials in hopes of improving the oxidation behavior by forming silica layers. In other systems, additions are made to SiC or Si_3N_4 to improve properties such as wear resistance. The oxidation behavior is then tested to ensure that these additions do not degrade the matrix oxidation resistance to unacceptable levels.

7.1.2.1. HfB_2/SiC

The first system of interest is the HfB_2-SiC system. While HfB_2 is the most oxidation resistant transition metal boride, oxidation rates are still quite high, especially at high temperatures where boria volatilizes as soon as it is formed. Claugherty et al. (1968) explored a variety of ways for improving the oxidation resistance of HfB_2. It was found that SiC additions increased the oxidation resistance of HfB_2 with best results obtained for 20 vol % SiC. The resulting scale was more adherent than that formed on pure HfB_2. The increased oxidation resistance of borides with SiC additions was explored further for ZrB_2 by Tripp et al. (1973) and for HfB_2 by Hinze et al. (1975b). At short times a transient rapid oxidation rate occurred as short circuit diffusion through ZrO_2 or HfO_2 controlled the oxidation rate. After this transient, parabolic kinetics were observed in both cases with the reaction rate controlled by diffusion of oxidant through a protective silica layer in the scale. Microscopy revealed a layer of silica on top of porous HfO_2. At temperatures below 1300°C, boria is found in the scale in the form of a borosilicate glass. Boria volatility is suppressed by the silica. At higher temperatures, selective vaporization of the boria occurs from the borosilicate glass.

7.1.2.2. Ti_3SiC_2

Another material of more recent interest is Ti_3SiC_2. This material has unique properties such as easy machinability, high thermal shock resistance, good ductility and high yield points at high temperatures. It has only recently been formulated as a single phase compound. The oxidation resistance has been studied by Barsoum et al. (1997). Parabolic oxidation is observed. Again a layered structure is observed with an inner layer of silica and titania and an outer layer of oriented rutile. The oxidation rates of this material are quite high suggesting diffusion control by the titania

layer. Barsoum et al.(1997) suggest that it may be possible to improve the oxidation resistance of Ti_3SiC_2 by adding $TiSi_2$ to form a continuous silica layer upon oxidation.

7.1.2.3. TiC or TiN additions to Si_3N_4

Composite materials based on Si_3N_4 with additions of TiC or TiN have been developed to increase wear resistance. The effect of the TiC (Opsommer et al., 1998) and TiN (Bellosi et al., 1990) additions on the oxidation behavior of these Si_3N_4 composites has been studied. In both cases, these additions have adverse effects on the oxidation resistance of Si_3N_4 especially at low temperatures. At low temperatures Bellosi et al. (1990) have shown that the Si_3N_4-TiN oxidation rate is dominated by the rate of reaction of the TiN phase with oxygen. At intermediate temperatures oxidation is rapid and parabolic, dominated by diffusion in the titania. At temperatures of 1200°C and higher, rates are parabolic and transport in the silicate phase in the scale limits the oxidation rates. In all three regimes, oxidation rates increase with the amount of TiC or TiN additive. At high temperatures, incorporation of titanium into the silicate scale as well as formation of TiO_2 may contribute to these enhanced oxidation rates (Opsommer et al., 1998). Therefore, additions of TiC or TiN to Si_3N_4 must be optimized so that wear resistance can be increased enough while not degrading the oxidation resistance of the Si_3N_4 matrix to unacceptable levels.

7.2. Composites which form Compound Oxides

In the preceding discussion on oxidation of composites, each matrix phase reacted with oxygen to form its corresponding oxide. No interactions between matrix or oxide phases were reported. In this section, a few examples are discussed in which the composite scale contains oxide compounds formed from more than one component of the matrix phases, e.g. mullite, zircon, or aluminum borates. This is not intended to be a complete review, but an illustration of the kinds of effects compound formation can have on oxidation behavior. For example, formation of the compound oxide scales may result in higher oxidation rates if the compound oxide is more permeable to oxygen, or likewise, lower oxidation rates if the compound oxide is less oxygen permeable. The volatility of scale components can also be reduced by the formation of compound oxides as will be discussed below for aluminum borates.

7.2.1. SiC-Reinforced Al_2O_3

SiC reinforcement of alumina results in significant improvements in mechanical properties such as toughness, creep strength, wear, and thermal fatigue compared to monolithic alumina, however,

these composites suffer from degradation due to thermal oxidation. Luthra and Park (1990) and Deqing and Lopez (1994) have studied the oxidation behavior of these composites. Parabolic oxidation is observed but at rates three orders of magnitude higher than for pure SiC indicating the reaction product is not pure silica. Oxidation rates increase with amount of SiC reinforcement. The observed reaction products are not the predicted equilibrium phases. For low SiC contents where alumina and mullite are predicted, alumina, mullite, and a glassy aluminosilicate are present in the oxidized zone. For higher SiC contents where silica and mullite are predicted, primarily mullite and glassy aluminosilicate phases are present after oxidation. Luthra and Park (1990) propose that oxygen diffusion through alumina controls the oxidation rate for low SiC concentrations. At higher concentrations the oxidation rate is controlled by oxygen diffusion in and/or diffusion of CO out through mullite or the glassy aluminosilicate phase. The composites form a layered structure in which a thin layer containing partially-reacted SiC particles is found beneath a completely reacted zone. A schematic of this structure can be found in Figure 49. TEM work on a similar composite (also containing zirconia in the alumina matrix) shows amorphous carbon and graphite (Backhaus-Ricault, 1991) are also present in the inner partially reacted SiC oxidation zone. The outer fully reacted zone contains porosity which is attributed to bubbles from CO evolution (Luthra and Park, 1990; Deqing and Lopez, 1994; Backhaus-Ricault, 1991). Thus, the formation of mullite and aluminosilicate glassy phases result in enhanced rates of transport of oxygen to the SiC reinforcement phase and corresponding rapid oxidation rates.

7.2.2. Si_2N_2O-ZrO_2

The porous Si_2N_2O-ZrO_2 composite material is another interesting example of the effects of compound formation on oxidation behavior. O'Meara et al. (1995) and Heim et al. (1995,1997a,b) have documented the case in which Si_2N_2O in this composite oxidizes to form SiO_2 at increasing rates up to temperatures around 1300°C. At temperatures higher than this, it is proposed that zircon, $ZrSiO_4$, or a mixture of zircon and an amorphous zircon silicate forms which effectively acts as a barrier to further oxidation. Schematics of the oxidation structure below and above the zircon formation temperature are shown in Figure 50. Courtright et al. (1991) have summarized the oxygen permeability of a number of oxides. In this summary the oxygen permeability of zircon is reported to be higher than that of silica. Therefore, the results of Heim et al. (1995, 1997a,b) are inconsistent with the permeability of zircon reported by Courtright (1991). Nevertheless, the concept of increasing the oxidation resistance of a material by choosing a composite which forms a less oxygen permeable compound oxide is viable.

7.2.3. TiB_2-Al_2O_3

From the discussion above on TiB_2 oxidation, it is known that the oxidation resistance of TiB_2 relies on the formation of a protective liquid boria scale. At temperatures high enough to volatilize the boria directly, linear oxidation rates are sometimes observed due to the nonprotective nature of the titania scale. The addition of Al_2O_3 or AlN to the TiB_2 results in better oxidation resistance (Tampieri and Bellosi, 1993; Schneider et al., 1996). At intermediate temperatures, 700-900°C, $Al_4B_2O_9$ is formed which slows the oxidation rate (Tampieri and Bellosi, 1993). In addition, boria volatility is reduced since it is entrapped in the aluminum borate phase (Schneider et al., 1996). At higher temperatures a less boria-rich phase is formed, $Al_{18}B_4O_{33}$, and higher oxidation rates are observed in the case of the AlN composite (Schneider et al., 1996). This system demonstrates the possibility to suppress volatility by compound formation during oxidation.

7.3. Composites which form Single Phase Oxide Solid Solutions

While few examples of this phenomenon exist and little work has been done in this area, it is possible to affect the oxidation behavior of materials which form a single phase oxide solid solution. For example, upon oxidation, a HfC/ZrC composite would form a solution of HfO_2/ZrO_2. Use of this type of composite, and choosing the HfC to ZrC ratio might be useful to control the monoclinic to tetragonal transformation temperature of the resulting scale or other properties of the matrix or scale.

8. Ceramic Matrix Composites

Ceramic matrix composites (CMCs) are perhaps the most promising ceramics today for high temperature structural applications. These CMCs include a wide range of multiphase ceramics with the additional phase added to impart improved fracture toughness. Examples of this include whiskers, particulates, and continuous fibers in a ceramic matrix (Evans, 1990). In many cases, the additional phase and/or coating around that phase has substantially different oxidation behavior than the matrix. This leads to complex oxidation and corrosion behavior for the entire composite.

Most of the current research on CMCs is focused on SiC fibers in matrices of oxides, Si_3N_4, or SiC. The fibers impart fracture toughness by deflecting the matrix cracks. To properly deflect cracks, a fiber must not bond with the matrix. For this reason, inert fiber coatings are needed. To date, only two adequate coatings have been found—graphitic carbon and boron nitride. Thus the entire composite has a slowly oxidizing phase (fibers and matrix) and an easily oxidizable phase (fiber coating). Generally at high temperatures, SiO_2 rapidly forms on the outside of the matrix and attack of the fiber coating is minimized. Even a matrix crack may quickly seal. However at

intermediate (500-1000°C) temperatures, silica forms very slowly and oxidative attack of the fiber coating becomes a critical issue. These constituents are shown schematically in Figure 51.

Consider first carbon fiber coatings. The attack of the coating at low temperatures is evident in the TGA data shown in Figure 52 (Bhatt, 1989). Note that the lower temperatures show an initial weight loss due to the oxidation of the carbon coatings of the fibers. At higher temperatures the matrix rapidly forms a film of SiO_2 and this oxidation is not evident. However in applications, components must operate at intermediate temperatures and hence it is important to understand this problem.

The most thorough treatment of this problem is from Filipuzzi and co-workers (1994) for carbon-coated SiC fibers in an SiC matrix. Their initial treatment consists of a matrix with uni-directional fibers with one end exposed. The process consists of a two-step oxidation of carbon and concurrent oxidation of the fiber and surrounding matrix. As carbon oxidizes, an annular region around the fiber is left. A schematic of this region is shown in Figure 53. The pressure dependence of SiC oxidation indicates that most of the oxidation would occur at the mouth of pore, as shown in Figure 53. Filipuzzi and co-workers first measured oxidation properties of each of the constituent parts of the composite as well as the composite as a whole. Standard TGA methods as well as resistivity measurements give an indication of the amount of carbon consumed. These data are used in an overall description of the composite oxidation.

The constituent data for the composite is used in the following analytical model. This is based on differential equations, which describe:

1. Diffusion of oxygen into the pore.
2. Two step oxidation of carbon to CO and CO_2.
3. Diffusion of CO out of the pore.
4. Consumption of oxygen by oxidation of the matrix.
5. Consumption of oxygen by oxidation of the fiber.

Appropriate boundary conditions are introduced and the equations are solved to generate kinetic curves such as those in Figure 52. Excellent agreement between their model and experiments are obtained. Their analysis indicates that thinner carbon coatings give better performance.

This analysis has been extended to other situations. Eckel and co-workers (1995) have examined the lower temperature regime, where SiC oxidation can be ignored. At temperatures near about 500°C reaction control becomes important in the oxidation of carbon. Windisch and co-workers

(1997) have seen evidence of reaction control at higher temperatures (1073-1373 K) and reduced oxygen pressures.

Recently Halbig et al. (1998) have examined the oxidation of SiC matrices with carbon fibers. Oxidation tests indicate low temperature oxidation is kinetically controlled by reaction of oxygen with the fibers and high temperature oxidation is diffusion controlled by diffusion of oxygen to the fibers. They have developed finite difference models of this process.

The other commonly used fiber coating is hexagonal BN. There are several important phenomena in the oxidation of a silicon-based composite with BN fiber coatings. These are illustrated in Figure 54(a) and (b). As the silicon-based material and the BN oxidize, both B_2O_3 and the SiO_2 form. These react to form low melting borosilicate melts, as shown in Figure 54a. Related to this, it is well-known that boron dramatically enhances the oxidation of silica forming materials (Schlicting, 1984). As discussed in Section 5 on monolithic BN, water vapor readily reacts with the B_2O_3 oxidation product and forms volatile $H_xB_yO_z(g)$ species. This can lead to effective volatilization of BN, much as carbon volatilizes, illustrated in Figure 54(b). However, unlike carbon, distinct interfaces are not formed with the BN. Rather there is a 'plug' of borosilicate formed and a gradual transition from oxide to nitride (Jacobson et al., 1999b) This is illustrated in Figure 55.

A description of this has been developed based on gas phase diffusion of the $H_xB_yO_z(g)$ species outward and boron-enhanced oxidation of the SiC to form a borosilicate plug (Jacobson et al., 1999b). This is shown schematically in Figure 56. Exposures of the SiC fiber with BN fiber coatings in a SiC matrix were conducted at 700 and 800°C in 1 and 10% H_2O/O_2 atmospheres with one end of the test sample ground off to expose the fiber ends and coatings. Then recession distances were measured. As illustrated in Figure 55, the exact distance was difficult to determine as interfaces were not always sharp. In order to apply the model to the experiments an adjustable parameter of boron-influenced SiC oxidation rates had to be introduced. Using substantially enhanced oxidation rates, reasonable agreement between the model and experimentally measured recession distances were obtained.

9. Summary

As structural ceramics find more applications in high temperature systems, oxidation and corrosion at high temperatures becomes an important field of study. In this chapter, the critical issues in this field have been surveyed. Ceramics have been classified according to the type of protective oxide they form. These include silica formers, alumina formers, boria formers, and transition metal oxide formers. Most of the literature covers silica formers since there are a

number of near-term applications for these materials. Basic oxidation mechanisms, water vapor interactions, volatilization routes, and salt-induced corrosion were discussed for these materials. Less information is available on alumina-forming ceramics. However the rapid oxidation rate in water vapor appears to be a major problem. Boria formers show rapid oxidation rates due to the formation of a liquid oxide film and are volatile in the presence of water vapor due to highly stable H-B-O(g) species formation. Transition metal carbides and nitrides also show rapid oxidation rates due to rapid transport in the oxide scale and cracking of that scale.

Multi-component ceramics allow the optimization of various physical properties. These include ceramics which form multi-component oxides as well as fiber-reinforced ceramic matrix composites. However, the oxidation behavior of these materials is complex compared to the pure materials. The leading fiber-reinforced composites are silicon-based and contain continuous SiC fibers with coatings of graphitic carbon or hexagonal boron nitride. The oxidation of the fiber coating at intermediate temperatures is a major issue and models of this process are discussed for both carbon and boron nitride coatings.

References:

Andrews, P., Riley, F. L. (1990), *Adv. Eng. With Ceramics*, Brit. Cer. Soc. Proc. 46, 259-270.

Antill, J. E., Warburton, J. B. (1970), *Reactions Between Solids and Gases*, NATO Advisory Group for Aerospace Research and Development Conference Proceedings 52, pp. 10-1 to 10-14.

Azema, N., Durand, J., Berjoan, R., Dupuy, C., Cot, L. (1991), *J. Eur. Cer. Soc. 8*, 291-298.

Backhaus-Ricoult, M. (1991), *J. Am. Ceram. Soc. 74*, 1793-1802.

Backhaus-Ricault, M., Gogotsi, Y. G. (1995), *J. Mater. Res. 10*, 2306-2321.

Balat, M., Flamant, G., Male, G., Pichelin, G. (1992), *J. Mat. Sci. 27*, 697-703.

Bargeron, C. B., Benson, R. C., Newman, R. W., Jette, A. N., Phillips, T. E. (1993*), Johns Hopkins APL Tech. Digest 14*, 29-36.

Barsoum, M. W., El-Ragby, T., Ogbuji, L. U. J. T. (1997), *J. Electrochem. Soc. 144*, 2508-2516.

Becher, P. F. (1983), *J. Am. Ceram. Soc. 66*, C-120-C-121.

Bellosi, A., Tampieri, A., Liu, Y.-Z. (1990), *Mat. Sci. Eng. A127*, 115-122.

Bellosi, A., Landi, E., Tampieri, A. (1993), *J. Mater. Res. 8*, 565-572.

Berkowitz-Mattuck, J. B. (1966), *J. Electrochem. Soc. 113*, 908-914.

Bhatt, R. T. (1989), NASA TM 102360.

Bouzouita, K., Desmaison, J., Billy, M. (1987), *J. Less-Common Met. 135*, 47-60.

Bouzouita, K., Desmaison, J., Billy, M. (1988), *J. Less-Common Met. 138*, 349-360.

Bornstein, N. M. (1996), *JOM 11*, 37-39.

Browning, R., Smialek, J. L., Jacobson, N. S. (1987), *Adv. Ceram. Matl. 2*, 773-779.

Chase, M. W. Jr., Davies, C. A., Downey, J. R. Jr., Frurip, D. J., McDonald, R. A., Syverud, A. N. (1986), *JANAF Thermochemical Tables, Third Edition*. New York: American Institute of Physics.

Chelnokov, V. E., Syrkin, A. L. (1997), *Mat. Sci. Eng. B 46*, 248-257.

Cheng, M. C., Cutler, I. B. (1979), *J. Am. Ceram. Soc. 62*, 593-596.

Choi, D. J., Fischbach, D. B., Scott, W. D. (1989), *J. Am. Ceram. Soc. 72*, 1118-1123.

Costa Oliviera, F. A., Edwards, R. A. H., Fordham, R. J., DeWit, J. H. W. (1994), in *Corrosion of Advanced Ceramics: Measurements and Modelling*, Nickel, K. G. (Ed.). Dordrecht, The Netherlands: Kluwer, pp. 177-188.

Clarke, D. R. (1983), *Progress in Nitrogen Ceramics*, Riley, F. L. (Ed.). The Hague, Netherlands: Martinus Nijhoff Publishers, pp. 421-426.

Claugherty, E. V., Pober, R. L., Kaufman, L. (1968), *Trans. Met. Soc. AIME 242*, 1077-1082.

Costello, J. A., Tressler, R. E. (1981), *J. Am. Ceram. Soc. 64*, 327-331.

Costello, J. A., Tressler, R. E., Tsong, J. S. T. (1981), *J. Am. Ceram. Soc. 64*, 332-335.

Costello, J. A., Tressler, R. E. (1986), *J. Am. Ceram. Soc. 69*, 674-681.

Courtois, C., Desmaison, J., Tawil, H. (1993), *J. Phys. IV C9*, 843-853.

Courtright, E. L., Prater, J. T., Henager, C. H., Greenwell, E. N. (1991a), *Wright Laboratory Technical Report 91-4006*, p. 5.2.

Courtright, E. L, Prater, J. T., Holcomb, G. R., St. Pierre, G. R., Rapp (1991b), R. A., *Oxid. Met. 36*, 423-437.

Cubiciotti, D., Lau, K. H. (1978), *J. Am. Ceram. Soc. 61*, 512-517.

Cubiciotti, D., Lau, K. H. (1979), *J. Electrochem. Soc. 126*, 1723-1728.

Deadmore, D. L., Lowell, C. E., Kohl, F. J. (1979), *Corrosion Science 19,* 371-378.

Deal, B. E. (1963), *J. Electrochem. Soc. 110*, 527-33.

Deal, B. E., Grove, A.S. (1965), *J. Appl. Phys. 36*, 3770-3778.

Deqing, W., Lopez, H. F. (1994), *Mat. Sci. Tech. 10*, 879-885.

Desmaison, J., Billy, M., and Smeltzer, W. W. (1976), in *Reactivity of Solids*, Wood, J., Lindqvist, O., Helgesson, Vannerberg, N-G. (Eds.). New York: Plenum Press, pp. 107-112.

Desmaison, J., Lefort, P., Billy, M. (1979), *Oxid. Met. 13*, 203-222.

Desmaison-Brut, M., Alexandre, N., Desmaison, J. (1997), *J. European Ceram. Soc. 17*, 1325-1334.

Douglass, D. L., Kofstad, P., Rahmel, A., Wood, G. C. (1996), *Oxid. Met.45*, 565-575.

Drowart, J., De Maria, G., Inghram, M. A. (1958), *J. Chem. Phys. 29*, 1015-1021.

Du, H., Tressler, R. E., Spear, K. E., Pantano, C. G. (1989a), *J. Electrochem. Soc. 136*, 1527-1536.

Du, H., Tressler, R. E., Spear, K. E. (1989b), *J. Electrochem. Soc. 136*, 3210-3215.

Easler, T. E., Bradt, R. C., Tressler, R. E. (1981), *J. Am. Ceram. Soc. 64*, 731-734.

Eckel, A. J., Cawley, A. J., Parthasarathy, T. A. (1995), *J. Am. Ceram. Soc. 78*, 972-980.

Evans, A. G. (1990), *J. Am. Ceram. Soc. 73*, 187-206.

Federer, J. I., Tiegs, T. N., Kotnick, D. M., Petrak, D. N. (1985), ORNL/TM-9677.

Ferber, M. K., Ogle, J., Tennery, V. J., Henson, T. (1985), *J. Am. Ceram. Soc. 68*, 191-197.

Ferber, M. K., Tennery, V. J. (1983), *Ceramic Bulletin 62*, 236-243.

Ferber, M. K., Tennery, V. J. (1984), *Ceramic Bulletin 63*, 898-904.

Fergus, J. W., Worrell, W. L. (1990), *Cer. Trans. 10*, 43-51.

Fillipuzzi, L., Naslain, R., Jaussaud, C. (1992), *J. Mat. Sci. 27*, 3330-3334.

Filipuzzi, L., Camus, G., Naslain, R., Thebault, J. (1994), *J. Am. Ceram. Soc. 77*, 459-466.

Filipuzzi, L., Naslain, R. (1994), *J. Am. Ceram. Soc. 77*, 467-480.

Fitzer, E., Ebi, R. (1974), *Silicon Carbide*, Marshall, R. C., Faust, Jr., J. W., Ryan, C. E. (Eds.). Columbia, S.C.: Univ. of S. Carolina Press, pp. 320-328.

Fox, D. S., Smialek, J. L. (1990), *J. Am. Ceram. Soc. 73*, 303-311.

Fox, D. S., Cuy, M. D., Nguyen, Q. (1997a), *J. Am. Ceram. Soc. 81*, 1565-1570.

Fox, D. S., Opila, E. J., Nguyen, Q. (1997b), *High Temperature Materials Chemistry IX*, 97-39, Spear, K. E. (Ed.). The Electrochemical Society: Pennington, N.J., pp. 804-811.

Fox, D. S. (1998), *J. Am. Ceram. Soc. 81*, 945-950.

Frisch, B., Thiele, W.-R., Drumm, R., Munnich, B. (1988), *Ber. DKG 65*, 277-284.

Fung, C. D., Kopanski, J. J. (1984), *Appl. Phys. Lett. 45*, 757-759.

Geiger, G. H., Poirier, D. R. (1973), *Transport Phenomena in Metallurgy,* Reading, MA: Addison-Wesley, p. 537.

Glemser , O., Wendlandt, H. G. (1963), *Advances in Inorganic Chemistry and Radiochemistry 5*, 215-258.

Gogotsi, Yu. G., Lavrenko, V. A. (1992), *Corrosion of High-Performance Ceramics*, Berlin: Springer-Verlag.

Gulbransen, E. A., Andrew, K . F., Brassart, F. A. (1966), *J. Electrochem. Soc. 113*, 1311-1314.

Halbig, M. C., Eckel, A. J., Cawley, J. D., Brewer, D.N. (1998), ARL-TR-1692.

Harris, J. H. (1998), *JOM*, June, 56-60.

Hashimoto, A. (1992), *Geochim. Cosmochim. Acta 56*, 511-532.

Heim, M., Arwin, H., Chen, J., Pompe, R. (1995), *J. Eur. Ceram. Soc. 15*, 313-318.

Heim, M., Chen, J., Pompe, R. (1997a), *J. Mat. Sci. 32*, 4025-4030.

Heim, M., O'Meara, C., Chen, J., Gatt, R., Pompe, R. (1997b), *J. Electrochem. Soc. 144*, 2740-2744.

Henager, C. H. Jr., Jones, R. H. (1992), *Ceram. Eng. Sci. Proceedings 13*, 411-419.

Heuer, A. H., Lou, V. L. K. (1990), *J. Am. Ceram. Soc. 73*, 2789-803.

Hincke, W. B., L. R. Brantley (1930), *JACS 52*, 48-52.

Hinze, J. W., Tripp, W. C., Graham, H. C. (1975a), in *Mass Transport Phenomena in Ceramics*, Cooper, A. R., Heuer, A. H. (Eds.). Columbus, OH: The American Ceramic Society, pp. 409-419.

Hinze, J. W., Tripp, W. C., Graham, H. C. (1975b), *J. Electrochem. Soc. 122*, 1249-1254.

Hinze, J. W., Graham, H. C. (1976), *J. Electrochem. Soc. 123*, 1066-1073.

Hirai, T., Niihara, K., Goto, T. (1980), *J. Am. Ceram. Soc. 63*, 419-424.

Holcomb, G. R., St. Pierre, G. R. (1993), *Oxid. Met. 40*, 109-118.

Hulbert, S. F. (1969), *J. Brit. Ceram. Soc. 6*, 11-20.

Ibidunni, A. O. (1993), *Oxid. Met. 40*, 5-20.

Irving, R. J., Worsley, I. G. (1968), *J. Less-Common Metals 16*, 103-112.

Jacobson, N. S. (1986), *J. Am. Ceram. Soc. 69*, 74-82.

Jacobson, N. S., Smialek, J. L. (1986), *J. Electrochem. Soc. 133*, 2615-2621.

Jacobson, N. S., Stearns, C. A., Smialek, J. L. (1986), *Adv. Ceram. Mat. 1*, 154-161.

Jacobson, N. S. (1989), *Oxid. Met. 31*, 91-103.

Jacobson, N. S. (1992), *J. Am. Ceram. Soc. 75*, 1603-1611.

Jacobson, N.S. (1993), *J. Am. Ceram. Soc. 76*, 3-28.

Jacobson, N. S., Smialek, J. L., Fox, D. S. (1994), *Corrosion of Advanced Ceramics*, Nickel, K. G. (Ed). Dordrecht, The Netherlands: Kluwer Academic Publishers, 205-222.

Jacobson, N. S., Rapp, R. A. (1995), NASA TM 106793.

Jacobson, N. S., Lee, K. N., Yoshio, T. (1996), *J. Am. Ceram. Soc. 79*, 2161-2167.

Jacobson, N. S., Opila, E. J. (1999), to appear in *Environmental Effects on Engineered Materials*, Jones, R. H. (Ed.). New York: Marcel-Dekker.

Jacobson, N. S., Farmer, S., Moore, A. J., Sayir, H. (1999a), *J. Am. Ceram. Soc.* in press.

Jacobson, N. S., Morscher, G. N., Bryant, D. R., Tressler, R. E.(1999b), *J. Am. Ceram. Soc.* in press.

Jakus, K., Ritter, Jr., J.E., Rogers, W. P. (1984), *J. Am. Ceram. Soc. 67*, 471-475.

Jones, S., Scott, W. D. (1989), *Adv. In Ceramics 26*, 151-157.

Kaufmann, L., Clougherty, E. V., Berkowitz-Mattuck, J. B. (1967), *Trans. Met. Soc. AIME 239*, 458-466.

Kim, H. -E., Moorhead, A. J. (1990), *J. Am. Ceram. Soc. 73*, 1868-1872.

Kim, H. -E., Moorhead, A. J. (1994), *J. Am. Ceram. Soc. 77*, 1037-1041.

Kim, N. -E., Readey, D. W. (1987), in *Silicon Carbide '87*, Cawley, J. D. and Semler, C. E. (Eds.). American Ceramic Society, pp. 301-312.

Kofstad, P. (1988), in *High Temperature Corrosion*, London: Elsevier, pp. 17-18.

Kohl, F. J., Liesz, D. M., Fryburg, G. C., Stearns, C. A. (1977), NASA TMX-73682.

Kuriakose, A. K., Margrave, J. L. (1964), *J. Electrochem. Soc. 111*, 827-31.

Kuromitsu, Y., Yoshida, H., Ohno, S., Masuda, H., Takebe, H., Morinaga, K. (1992), *J. Cer. Soc. Japan 100*, 70-74.

Lacombe, P., Bonnet, C. (1990), AIAA-90-5208, in *AIAA Second International Aerospace Plane Conference*, Washington, D.C.: American Institute of Aeronautics and Astronautics.

Lamkin, M. A., Riley, F. L., Fordham, R. J. (1990), in *High Temperature Corrosion of Technical Ceramics*, Fordham, R. J., (Ed.). London: Elsevier, 181-191.

Lamkin, M. A., Riley, F. L., Fordham, R. J. (1992), *J. Eur. Ceram. Soc. 10*, 347-367.

Lavrenko, V. A., Alexeev, A. F. (1986), *Ceram. Int. 12*, 25-31.

Lavrenko, V. A., Pomytkin, A. P., Kislyi, P. S., Grabchuk, B. L. (1976), *Oxid. Met. 10*, 85-95.

Lee, K. N., Miller, R. A., Jacobson, N. S. (1994), *MRS Bulletin 19*, 35-38.

Lee, K. N., Miller, R. A., Jacobson, N. S. (1995), *J. Am. Ceram. Soc. 78*, 705-710.

Lefort, P., Marty, F. (1989), *J. Chim. Phys. 86*, 1329-1342.

Lepp, A., Schwetz, K. A., Hunold, K. (1989), *J. European Ceram. Soc. 5*, 3-9.

Levin, E. M., McMurdie, H. F. (1975), *Phase Diagrams for Ceramists 1975 Supplement*, Columbus, OH: American Ceramic Society, 17.

Ligenza, J. R. (1962), *J. Electrochem. Soc. 109*, 73-76.

Lu, W. -J., Steckl, A. J., Chow, T. P., Katz, W. (1984), *J. Electrochem. Soc. 131*, 1907-1914.

Luthra, K. L., Park, H. D. (1990), *J. Am. Ceram. Soc. 73*, 1014-1023.

Maeda, M., Nakamura, K., Ohkubo, T., Ito, M., Ishii, E. (1989), *Cer. Intl. 15*, 247-253.

Margrave, J. L. (1956), *J. Phys. Chem. 60*, 715-717.

Mayer, M. I., Riley, F. L. (1978), *J. Mat. Sci. 13*, 1319-1328.

McLean, A. F. (1986), in *Proc. Second International Symposium on Ceramic Materials and Components for Heat Engines*, pp. 1023-1034.

McNallan, M. J., van Roode, M., Price, J. R. (1990), in *Corrosion and Corrosive Degradation of Ceramics, Ceramic Transactions, Vol. 10,* Tressler, R. E., McNallan, M. J., (Eds.). Westerville, OH: American Ceramic Society, pp. 181-191.

McNallan, M. J., Lee, S. Y., Hsu, P. P. (1994), *Corrosion of Advanced Ceramics*, Nickel, K.G. (Ed.). Kluwer Academic Publishers: Dordrecht, The Netherlands, pp. 189-202.

Meschi, D. J., Chupka, W. A., Berkowitz, J. (1960), *J. Chem. Phys. 33*, 530-533.

Motzfeldt, K. (1964), *Acta Chem. Scand. 18*, 1596-1606.

Moulson, A. J., Roberts, J. P. (1961), *Trans. Faraday Soc. 57*, 1208-1216.

Narushima, T., Goto, T., Hirai, T. (1989), *J. Am. Ceram. Soc. 72*, 1386-1390.

Narushima, T., Goto, T., Iguchi, Y., Hirai, T. (1991), *J. Am. Ceram. Soc. 74*, 2583-2586.

Narushima, T., Lin, R.Y., Hirai, T. (1993a), *J. Am. Ceram. Soc. 76*, 1047-1051.

Narushima, T., Goto, T., Yokoyama, Y., Iguchi, Y., Hirai, T. (1993b), *J. Am. Ceram. Soc. 76*, 2521-2524.

Narushima, T., Goto, T., Hirai, T., Iguchi, Y. (1997), *Mat. Trans. JIM 38*, 821-835.

Norton, F. J. (1961), *Nature 191*, 701.

Oda, K., Yoshio, T. (1993), *J. Mat. Sci. 28*, 6562-6566.

Ogbuji, L. U. (1981), *J. Mat. Sci. 16*, 2753-2759.

Ogbuji, L. U. J. T., Smialek, J. L. (1991), *J. Electrochem. Soc. 138*, L51-L53.

Ogbuji, L. U. J. T., Jayne, D. T. (1993), *J. Electrochem. Soc. 140*, 759-766.

Ogbuji, L. U. J. T. (1994), *Corrosion of Advanced Ceramics*, Nickel, K. G. (Ed). Dordrecht, The Netherlands: Kluwer Academic Publishers, 117-129.

Ogbuji, L. U. J. T., Bryan, S. R. (1995), *J. Am. Ceram. Soc. 78*, 1272-1278.

Ogbuji, L. U. J. T. (1995), *J. Am. Ceram. Soc. 78*, 1279-1284.

Ogbuji, L. U. J. T., Opila, E. J. (1995), *J. Electrochem. Soc. 142*, 925-930.

Ogbuji, L. U. J. T. (1997), *J. Am. Ceram. Soc. 80*, 1544-1550.

O'Meara, C., Heim, M., Pompe, R. (1995), *J. Eur. Ceram. Soc. 15*, 319-328.

Opila, E. J., Fox, D. S., Barrett, C. A. (1993), *Cer. Eng. Sci. Proc. 14*, 367-374.

Opila, E. J. (1994), *J. Am. Ceram. Soc. 77*, 730-736.

Opila, E. J. (1995), *J. Am. Ceram. Soc. 78*, 1107-1110.

Opila, E. J., Jacobson, N. S. (1995), *Oxid. Met. 44*, 527-544.

Opila, E. J., Fox, D. S., Jacobson, N. S. (1997), *J. Am. Ceram. Soc. 80*, 1009-1012.

Opila, E. J., Hann, Jr., R. E. (1997), *J. Am. Ceram. Soc. 80*, 197-205.

Opila, E. J., Nguyen, Q. N. (1998), *J. Am. Ceram. Soc. 81*, 1949-1952.

Opila, E., Jacobson, N., Humphrey, D., Yoshio, T., Oda, K. (1998), in *High Temperature Corrosion and Materials Chemistry*, Hou, P., McNallan, M., Oltra, R., Opila, E., Shores, D. (Eds.). Pennington, NJ: The Electrochemical Society, 430-437.

Opila, E. J., *J. Am. Ceram. Soc.* In press.

Opila, E. J., Smialek, J. L., Robinson, R. C., Fox, D. S., Jacobson, N. S., accepted for publication, *J. Am. Ceram. Soc.*

Opsommer, A., Gomez, E., Castro, F. (1998), *J. Mat. Sci. 33*, 2583-2588.

Pareek, V., Shores, D. A. (1991), *J. Am. Ceram. Soc. 74*, 556-563.

Park, S. C., Cho, K., Kim, J. J. (1998), *J. Mat. Sci. Lett. 17*, 23-25.

Patel, J. K., Thompson, D. P. (1988), *Br. Ceram. Trans. J. 87*, 70-73.

Patterson, M. C. L., He, S., Fehrenbacher, L. L., Hanigofsky, J., Reed, B. D. (1996), *Materials and Manufacturing Processes 11*, 367-79.

Pechentkovskaya, L. E., Nazarchuk, T. N. (1981), *Soviet Powder Metallurgy 7*, 83-86.

Pelton, A. D., Bale, C. W. (1983), in *High Temperature Corrosion*, Rapp, R. A. (Ed), Houston, TX: National Association of Corrosion Engineers, pp. 451-459.

Podobeda, L. T., Tsapuk, A. K., Buravov, A. D. (1976), *Soviet Powder Metallurgy 9*, 44-47.

Powell, J. A., Neudeck, P. G., Matus, L. G., Petit, J. B. (1992), *Mater. Res. Soc. Proc. 242*, 495-505.

Price, J. R., van Roode, M., Stala, C. (1992), *Key Eng. Mater. 72-74*, 71-84.

Probst, H. B. (1986), in *Ceramic Components for Engines*, London: Elsevier, pp. 45-58.

Rama Rao, G. A., Venugopal, V. (1994), *J. Alloys and Compounds 206*, 237-242.

Ramberg, C. E., Cruciani, G., Spear, K. E., Tressler, R. E., Ramberg, Jr., C. F. (1996), *J. Am. Ceram. Soc. 79*, 2897-2911.

Ramberg, C. E. (1997), Ph.D. Thesis, University of Pennsylvania.

Rapp, R. A. (1986), *Corros. Sci. 42*, 568-577.

Robinson, D., Dieckmann, R. (1994), *J. Mat. Sci. 29*, 1949-1957.

Robinson, R. C., Smialek, J. L, accepted for publication, *J. Am. Ceram. Soc.*

Rosner, D. E., Allendorf, H. D. (1970), *J. Chem. Phys. 74*, 1829-1839.

Sangiorgi, R. (1994), in *Corrosion of Advanced Ceramics: Measurements and Modelling*, Nickel, K. G. (Ed.). Dordrecht, The Netherlands: Kluwer, pp. 261-284.

Sato, T., Haryu, K., Endo, T., Shimada, M. (1987), *J. Mat. Sci. 22*, 2277-2280.

Schiroky, G. H., Price, R. J., Sheehan, J. E. (1986), *GA Technologies Report GA-A18696.*

Schneider, B. (1995), PhD Thesis, University of Bordeaux.

Schneider, S. V., Desmaison-Brut, M., Gogotsi, Y. G., Desmaison, J. (1996), *Key Engineering Materials 113*, 49-58.

Schlicting, J. (1984), *J. Non-Crystalline Sol. 63*, 173-181.

Shaw, N. J., DiCarlo, J. A., Jacobson, N. S., Levine, S. R., Nesbitt, J. A., Probst, H. B., Sanders, W. A., Stearns, C. A. (1987), NASA TM 100169.

Sheldon, B. W. (1996), *J. Am. Ceram. Soc. 79*, 2993-2996.

Shimada, S., Ishii, T. (1990), *J. Am. Ceram. Soc. 73*, 2804-8.

Shimada, S., Nishisako, M., Inagaki, M., Yamamoto, K. (1995), *J. Am. Ceram. Soc. 78*, 41-48.

Shimada, S. (1996), *J. Mat. Sci. 31*, 673-677.

Shimada, S. (1997), *Solid State Ionics 101-103*, 749-753.

Shimada, S., Inagaki, M., Matsui, K. (1997), *J. Am. Ceram. Soc. 75*, 2671-2677.

Shimada, S. (1998), in *Proceedings of the Symposium on High Temperature Corrosion and Materials Chemistry*, Hou, P., McNallan, M. J., Oltra, R., Opila, E. J., Shores, D. (Eds.). Pennington, NJ: The Electrochemical Society, 334-348.

Singhal, S. C., Lange, F. F. (1975), *J. Am. Ceram. Soc. 58*, 433-435.

Singhal, S. C. (1976a), *J. Mat. Sci. 11*, 1246-1253.

Singhal, S. C. (1976b), *J. Mat. Sci. 11*, 500-509.

Singhal, S. C. (1976c), *Ceram. Int. 2*, 123-130.

Smialek, J. L., Jacobson, N. S. (1986), *J. Am. Ceram. Soc. 69*, 741-752.

Soulen, J. R., Sthapitanonda, P., Margrave, J. L. (1955), *Phys. Chem. 59*, 132-136.

Stearns, C. A., Kohl, F. J., Rosner, D. E. (1983), in *High Temperature Corrosion*, Rapp, R. A. (Ed.). Houston, TX: National Association of Corrosion Engineers, 441-450.

Storms, E. K. (1967), *The Refractory Carbides*, New York: Academic Press, pp. 229.

Sun, T., Pickrell, G. R., Brown, Jr., J. J. (1994), *J. Am. Ceram. Soc. 77*, 3209-3214.

Suzuki, A., Ashida, H., Furui, N., Mameno, K., Matsunami, H. (1982), *Japan. J. Appl. Phys. 21*, 579-585.

Tampieri, A., Landi, E., Bellosi, A.. (1991), *Brit. Ceram. Trans. J. 90*, 194-196.

Tampieri, A., Bellosi, A. (1993), *J. Mat. Sci. 28*, 649-653.

Tedmon, Jr., C. S. (1966), *J. Electrochem. Soc. 113*, 766-768.

Tressler, R. E., Costello, J. A., Zheng, Z. (1985), in *Industrial Heat Exchangers*, A. J. Hayes et al. (Eds.). Warrendale, PA: American Society for Metals, pp. 307-314.

Tressler, R. E. (1990), *Cer. Trans. 10*, 99-124.

Tripp, W. C., Graham, H. C. (1971), *J. Electrochem. Soc. 118*, 1195-1199.

Tripp, W. C., Davis, H. H., Graham, H. C. (1973), *Bull. Am. Ceram. Soc. 52*, 612-616.

Turkdogan, E. T., Grieveson, P., Darken, L. S. (1963), *J. Phys. Chem. 67*, 1647-1654.

Vaughn, W. L., Maahs, H. G. (1990), *J. Am. Ceram. Soc. 73*, 1540-1543.

Voitoivich, V. B. (1997), *H. Temp. Mat. Processes 16*, 243-253.

Voitovich, R. F., Pugach, E. A. (1973), *Poroshkovaya Metallurigiya 11*, 67-74.

Wagner, C. (1958), *J. Appl. Phys. 29*, 1295-1297.

Wang, D. N., Liang, K. M. (1998), *J. Mat. Sci. Letters 17*, 343-344.

Watt, G. W., Andresen, R. E., Rapp, R. A. (1981), in *Molten Salts*, Braunstein, J., Selman, J. R. (Eds.). Pennington, NJ: The Electrochemical Society, p. 81.

Windisch, C. F., Jr., Henager, C. H., Jr., Springer, G. D., Jones, R. H. (1997), *J. Am. Ceram. Soc. 80*, 569-574.

Zheng, Z., Tressler, R. E., Spear, K. E. (1990a), *J. Electrochem. Soc. 137*, 854-858.

Zheng, Z., Tressler, R. E., Spear, K. E. (1990b), *J. Electrochem. Soc. 137*, 2812-2816.

Zheng, Z., Tressler, R. E., Spear, K. E. (1992), *Corrosion Science 33*, 545-556.

Zheng, Z., Tressler, R. E., Spear, K. E. (1992), *Corrosion Science 33*, 569-580.

Zmbov, K. F., Amers, I. I., Margrave, J. L. (1971), *High Temp. Sci. 5*, 235-240.

General References:

Gogotsi, Yu. G. and Lavrenko, V. A. (1992), *Corrosion of High-Performance Ceramics*, Berlin: Springer-Verlag.

Jacobson, N. S. (1993), *J. Am. Ceram. Soc. 76*, 3-28.

Narushima, T., Goto, T., Hirai, T., Iguchi, Y. (1997), *Mat. Trans. JIM* 38, 821-835.

Nickel, K. G. (Ed) (1994), *Corrosion of Advanced Ceramics*, Dordrecht, The Netherlands: Kluwer Academic Publishers.

Tressler, R. E. and McNallan, M. J. (Eds.) (1990), *Corrosion and Corrosive Degradation of Ceramics, Ceramic Transactions, Vol. 10,* Westerville, OH: American Ceramic Society.

Table I. Current and projected uses of ceramics.

Application	Ceramics	Approximate Use Temperatures	Environment	References
Turbine engine Components Combuster Liners Blades and Vanes	SiC, Si_3N_4, Composites	900-1400	Combustion gases Deposits: Na, Mg, Ca sulfates, Sodium vanadates	Probst (1986)
Piston engine Components Pistons Valves	SiC, Si_3N_4, Composites	900-1400	Combustion gases	McLean (1986)
Industrial Furnaces, Heat Exchangers	SiC, Composites	900-1400	Combustion gases, various deposits	Federer et al. (1985)
Coal combustion, Particle filters	SiC, Composites	700-1000	Combustion gases, slag deposits	Ferber et al. (1985)
Chemical Process Vessels, Coal Gasifiers, Waste Incinerators	SiC, Si_3N_4	900-1400	Various gases: air, H_2S, HCl	Costa Oliviera et al. (1994)
Re-entry shields	SiC, composites	1000-1800	Reduced pressure N_2, O_2, CO_2, N, O	Lacombe and Bonnet (1990) Jacobson and Rapp (1995)
High temperature semi-conductors	SiC	Use: 600 Processing: 1200	Air	Chelnokov and Syrkin (1997), Powell et al. (1992)
Electronic substrates	AlN	Use: 600 Processing: 1200	Air	Harris (1998)
Fiber coatings for composites, crucibles, insulators	BN	900-1400	Fiber coatings: reduced pressure combustion gases Crucibles: vacuum, inert gases	Henager and Jones (1992) Lepp et al. (1989)
Rocket Engine throats	HfC, ZrC	1500-2000	H_2/O_2 combustion products	Patterson et al. (1996)
Liquid metal containers, processing and heat transfer	Transition metal carbides	600-1400	Vacuum or inert gas and liquid metals	Sangiorgi (1994)

Table II. Coefficients of thermal expansion for silica-forming ceramics and several refractory oxides (Lee et al., 1994)

Material	CTE (10^6 K^{-1})
SiC	5.2
Si_3N_4	3.2
Mullite ($3Al_2O_3 \cdot 2SiO_2$)	5.4
Alumina (Al_2O_3)	9
Partially stabilized zirconia ($0.09Y_2O_3 \cdot ZrO_2$)	10

Table III. Transition Metal Carbides (Storms, 1967). The most stable carbides are shown in the box with strong metal-carbon and metal-metal bonds.

Sc	Ti	V	Cr	Mn
Y	Zr	Nb	Mo	Tc
La	Hf	Ta	W	Re

Figure Captions

1. Oxidation rates of non-oxide ceramics. (Shaw et al, 1987.)

2. Schematic of thermogravimetric apparatus (TGA) used for measuring oxidation kinetics. (Jacobson, 1993. Reprinted with permission of the American Ceramic Society.)

3. Calculated combustion products from combustion of jet fuel in air over a range of fuel to air ratios. Thermodynamic equilibrium is assumed. Also shown is the corresponding adiabatic flame temperature. (Jacobson, 1993. Reprinted with permission of the American Ceramic Society.)

4. Schematic of jet-fuel burner rig, used for studying oxidation and corrosion of high temperature materials. (Jacobson, 1993. Reprinted with permission of the American Ceramic Society.)

5. Schematic structure of silica: a) cristobalite b) amorphous silica c) alkali modified silica. Silicon atoms are small dark circles. Oxygen atoms are open circles. Large shaded circles in c) represent impurity ions such as sodium. (Adapted from Lamkin et al., 1992.)

6. Oxidation rates for pure silica forming materials in dry oxygen. (Adapted from Ogbuji and Opila, 1995.)

7. Micrograph of CVD SiC oxidized for 24h at 1400°C showing formation of spherulitic cristobalite. (Jacobson, 1993. Reprinted with permission of the American Ceramic Society.)

8. Cross-section of CVD Si_3N_4 oxidized for 48h at 1400°C showing the amorphous silicon oxynitride layer. The SiO_2 layer has been thinned. (Ogbuji, 1994)

9. Schematic diagram of the Si_3N_4 oxidation model in which a continuously varying oxygen and nitrogen content of the silicon oxynitride layer is proposed. (Adapted from Ogbuji and Jayne, 1993.)

10. Weight change behavior of dense SiC hot-pressed with Al_2O_3 oxidized at 1370°C in pure dry oxygen at 1 atm pressure. (Singhal, 1975. Reprinted with permission of the American Ceramic Society.)

11. Y_2O_3-containing Si_3N_4 oxidized for 97h at 1300°C in dry oxygen showing crystalline yttria silicate formed on oxide surface by migration of yttria impurities into the scale. (Jacobson, 1993. Reprinted with permission of the American Ceramic Society.)

12. Oxidation and reoxidation of Si_3N_4 with MgO additives at 1644K. (Cubiccioti and Lau, 1978. Reprinted with permission of the American Ceramic Society.)

13. Calculated activity of all potassium-containing vapor species for K_2CO_3 in equilibrium with a gas phase of $9CO_2$:$1O_2$ at 1160K as a function of water vapor content. (Pareek and Shores, 1991. Reprinted with permission of the American Ceramic Society.)

14. The diffusivity of oxygen and water vapor in amorphous silica as a function of temperature. (Adapted from Deal and Grove, 1965.)

15. The effect of temperature on the parabolic rate constant, B, of silicon in dry oxygen and water vapor. (Adapted from Deal and Grove, 1965.)

16. The effect of the partial pressure of oxidant on the parabolic rate constant of silicon. (Adapted from Deal and Grove, 1965.)

17. Bubbles formed in SiO_2 due to oxidation of SiC in 90% water vapor/10% O_2 at 1200°C. (Opila, in press.)

18. The variation of the parabolic oxidation rate of CVD SiC on water vapor partial pressure in O_2/H_2O gas mixtures at 1 atm total pressure. (Opila, in press.)

19. Paralinear kinetics for SiC oxidized in water vapor. Model results typical of exposures at 1200°C in 50% H_2O/50% O_2 at flow rates of 4.4 cm/sec. a) oxide growth and matrix recession b) weight change. (Adapted from Opila and Hann, 1997.)

20. Oxidation/volatilization weight change kinetics for silica, CVD SiC, and CVD Si_3N_4 at 1200°C in 50% H_2O/50% O_2 at flow rates of 4.4 cm/sec.

21. Weight loss of CVD SiC in a fuel-lean high pressure burner rig with gas velocities of 20 m/sec. (Adapted from Robinson and Smialek, 1999.)

22. Normalized weight loss rates of CVD SiC in a fuel-lean high pressure burner rig with gas velocities of 20 m/sec and total pressures between 5 and 15 atm. (Adapted from Robinson and Smialek, 1999.)

23. Comparison of CVD SiC oxidation kinetics in the oxidants CO_2, O_2 and H_2O at 1200°C. (Opila and Nguyen, 1998. Reprinted with permission of the American Ceramic Society.)

24. Thermal expansion of crystalline SiO_2, SiC, Si_3N_4, and amorphous SiO_2 as a function of temperature. (Jacobson, 1993. Reprinted with permission of the American Ceramic Society.)

25. Cyclic oxidation weight change kinetics for several silica forming materials exposed in air at 1300°C in 5h cycles (Jacobson and Opila, 1999).

26. Volatility diagrams for: (a) Pure Si at 1800K, showing all vapor species, (Kohl et al., 1977.) (b) SiC showing only the most abundant vapor species, (Heuer and Lou, 1990. Reprinted with permission of the American Ceramic Society.) (c) Si_3N_4 showing only the most abundant vapor species. (Heuer and Lou, 1990. Reprinted with permission of the American Ceramic Society.)

27. Predominance diagrams at 1500K with vapor pressures of major species superimposed for (a) SiC and (b) Si_3N_4. (Jacobson, 1993. Reprinted with permission of the American Ceramic Society.)

28. Total vapor pressure generated at (a) SiC/SiO_2 interface for different activities of Si and (b) Si_2N_2O/SiO_2 interface for different activities of Si. (Jacobson, 1993. Reprinted with permission of the American Ceramic Society.)

28. CVD SiC oxidized for 1 h at 2073 K in air. (Jacobson, 1993. Reprinted with permission of the American Ceramic Society.)

30. Schematic of two approaches to the active-to-passive oxidation transition: (a) Wagner boundary layer approach and (b) SiO_2 'smoke' formation. (Adapted from Narushima et al., 1997.)

31. Measured and calculated active-to-passive transitions for SiC oxidation. Results for SiC produced by various processes are shown: chemically-vapor-deposited (CVD), pressureless

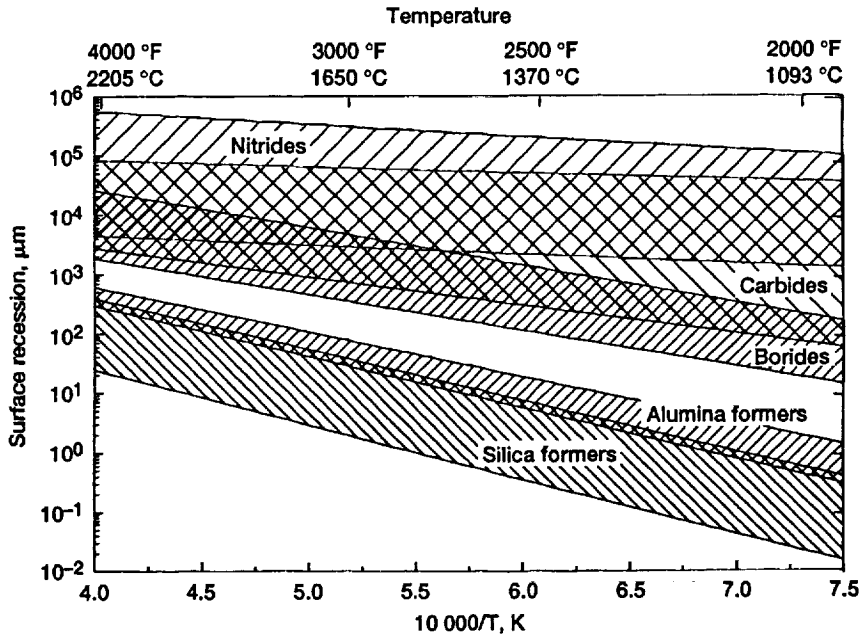
Temperature
4000 °F
2205 °C
3000 °F
1650 °C
2500 °F
1370 °C
2000 °F
1093 °C
Surface recession, μm
10^6
10^5
10^4
10^3
10^2
10^1
10^0
10^{-1}
10^{-2}
Nitrides
Carbides
Borides
Alumina formers
Silica formers
4.0
4.5
5.0
5.5
6.0
6.5
7.0
7.5
10 000/T, K

Figure 1

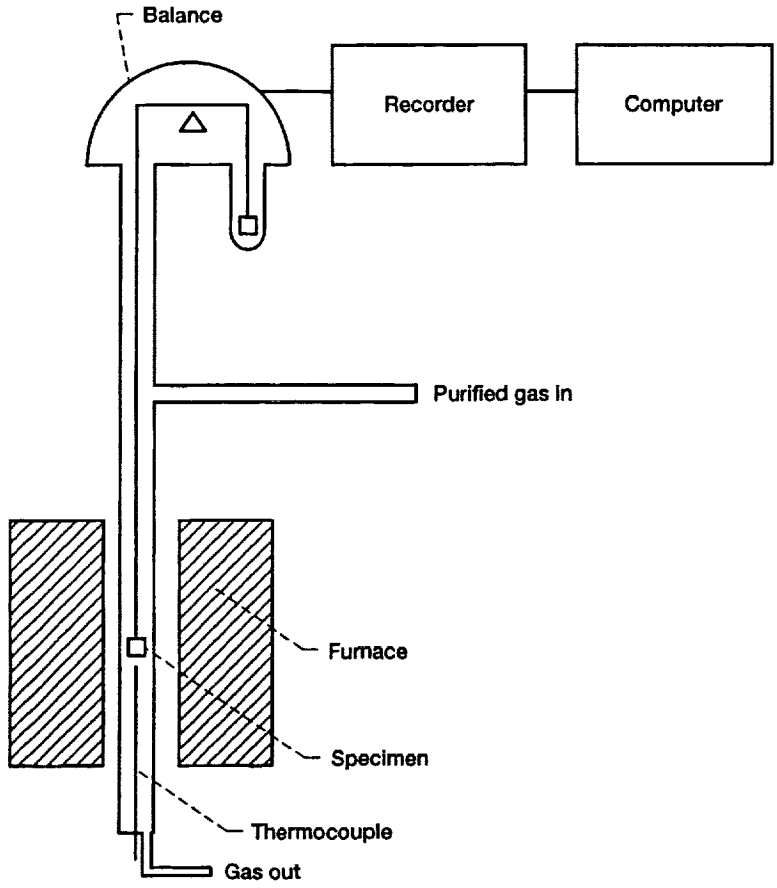
Balance
Recorder
Computer
Purified gas in
Furnace
Specimen
Thermocouple
Gas out

Figure 2

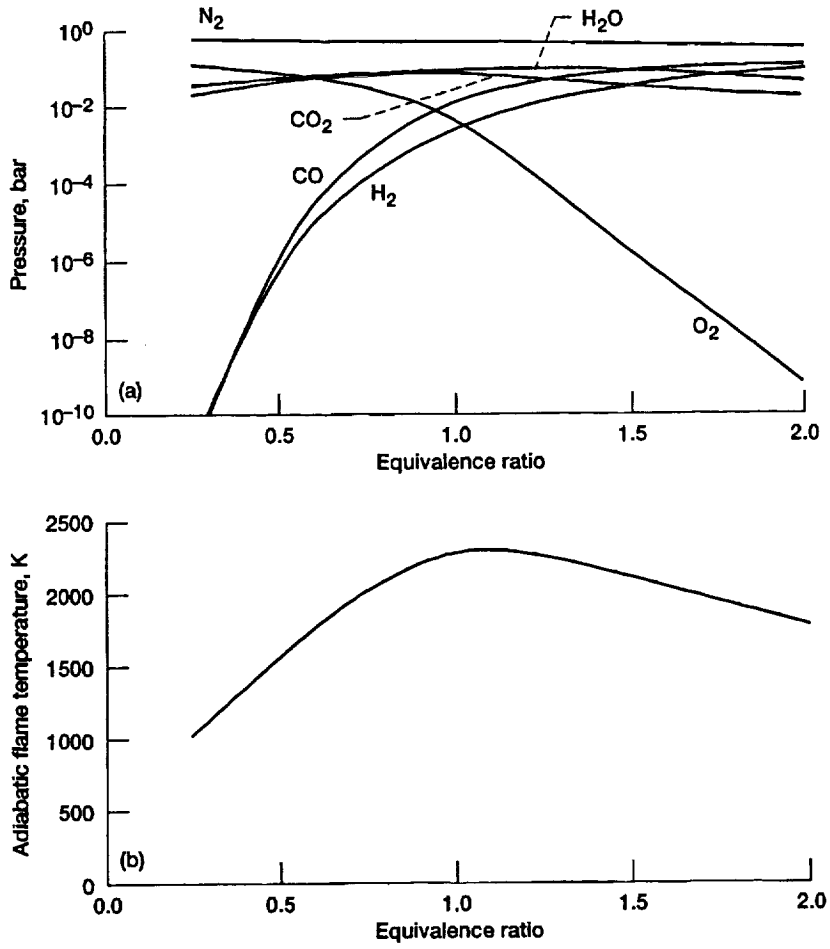
N_2
H_2O
CO_2
CO
H_2
O_2
Pressure, bar
10^0
10^{-2}
10^{-4}
10^{-6}
10^{-8}
10^{-10}
(a)
0.0
0.5
1.0
1.5
2.0
Equivalence ratio
Adiabatic flame temperature, K
2500
2000
1500
1000
500
0
(b)
0.0
0.5
1.0
1.5
2.0
Equivalence ratio

Figure 3

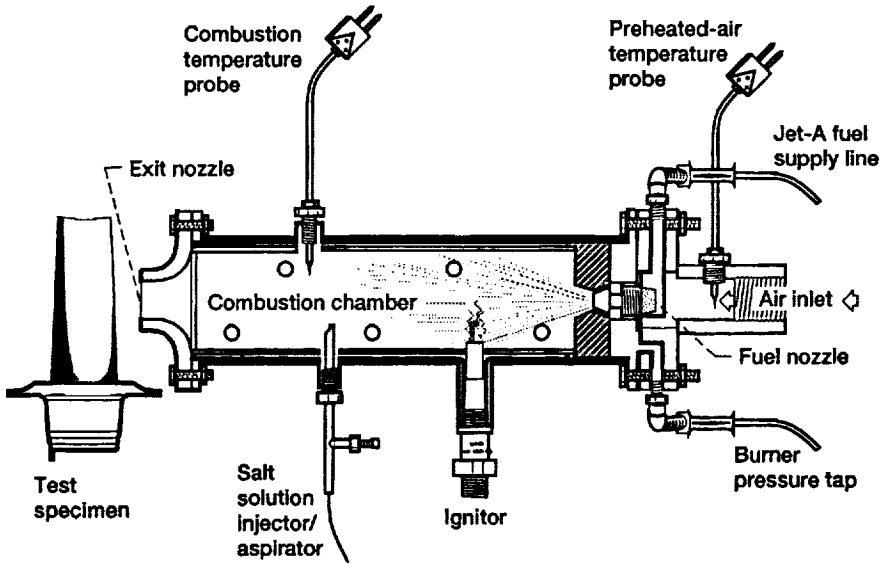
Combustion temperature probe
Preheated-air temperature probe
Jet-A fuel supply line
Exit nozzle
Combustion chamber
Air inlet
Fuel nozzle
Burner pressure tap
Test specimen
Salt solution injector/ aspirator
Ignitor

Figure 4

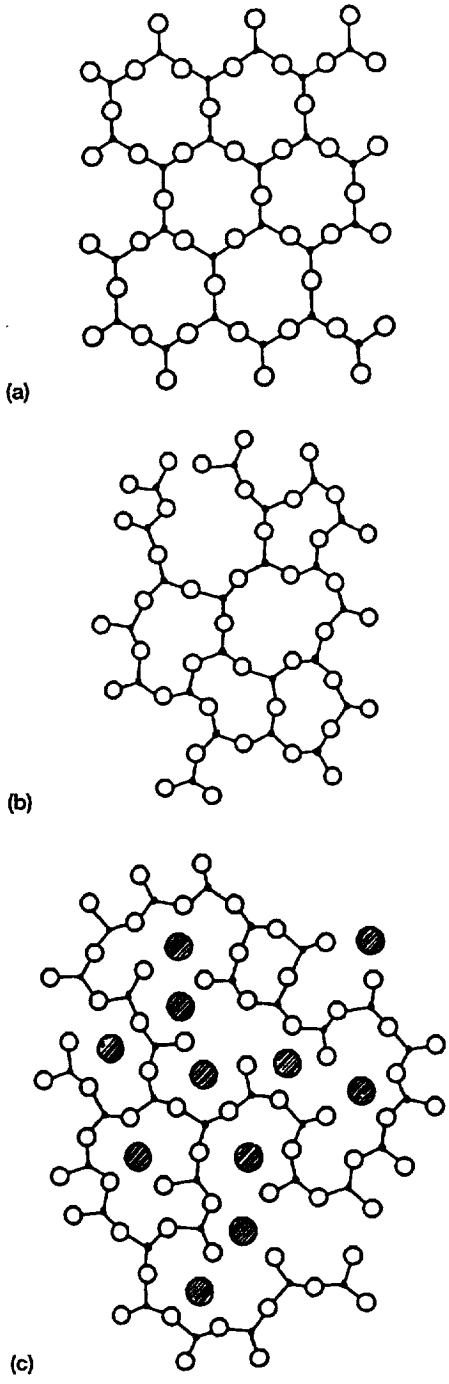

Figure 5

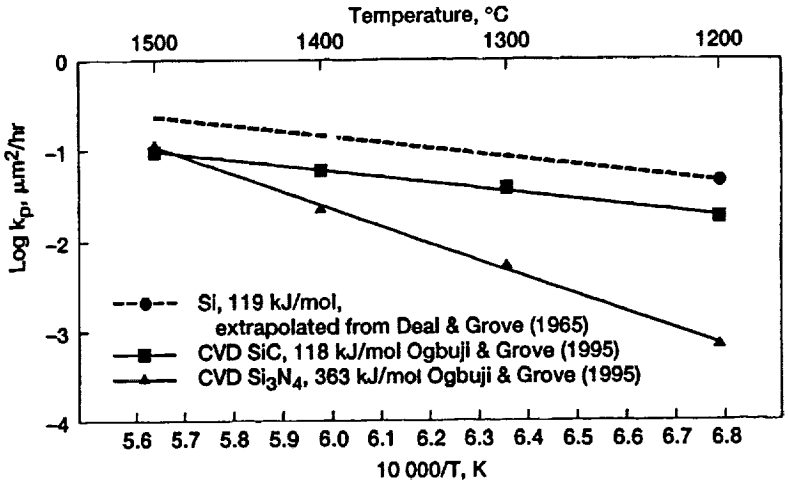
Temperature, °C
1500
1400
1300
1200
0
−1
−2
−3
−4
Log k_p, μm²/hr
Si, 119 kJ/mol,
extrapolated from Deal & Grove (1965)
CVD SiC, 118 kJ/mol Ogbuji & Grove (1995)
CVD Si_3N_4, 363 kJ/mol Ogbuji & Grove (1995)
5.6 5.7 5.8 5.9 6.0 6.1 6.2 6.3 6.4 6.5 6.6 6.7 6.8
10 000/T, K

Figure 6

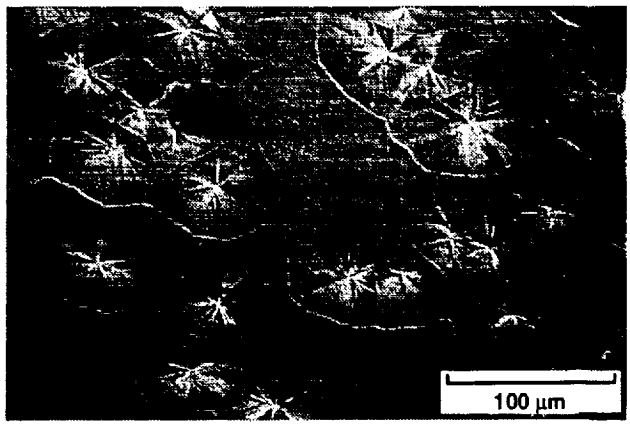

Figure 7

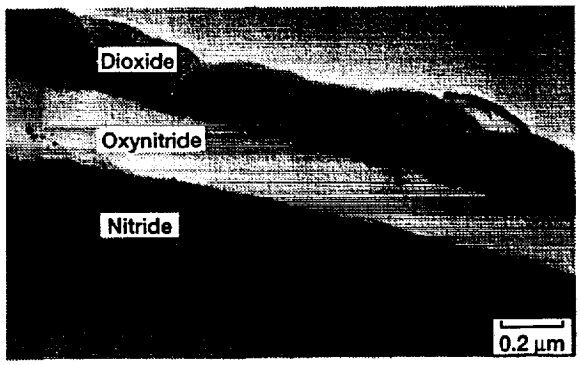

Figure 8

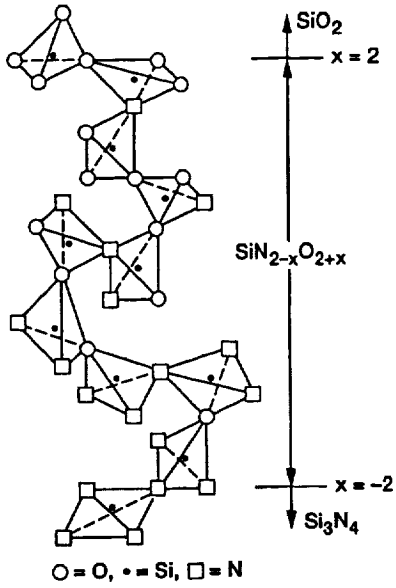

Figure 9

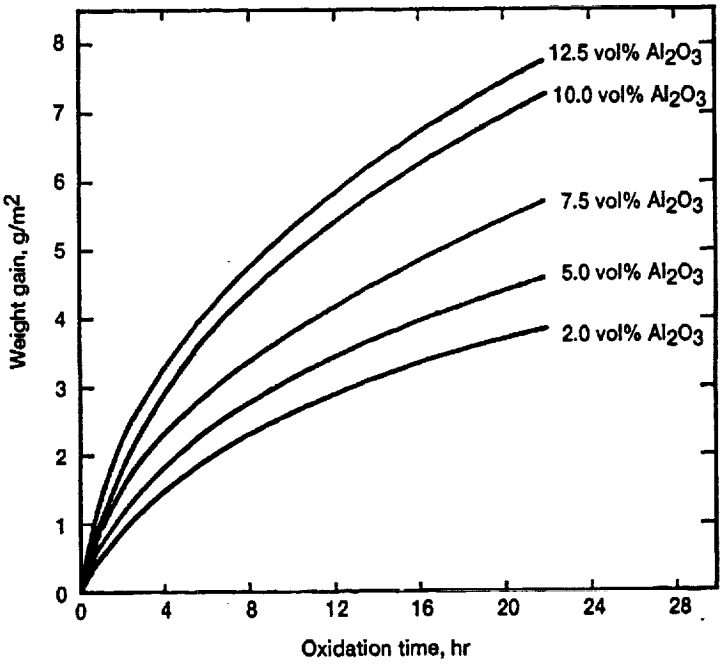
12.5 vol% Al_2O_3
10.0 vol% Al_2O_3
7.5 vol% Al_2O_3
5.0 vol% Al_2O_3
2.0 vol% Al_2O_3
Weight gain, g/m^2
Oxidation time, hr
0
1
2
3
4
5
6
7
8
0
4
8
12
16
20
24
28

Figure 10

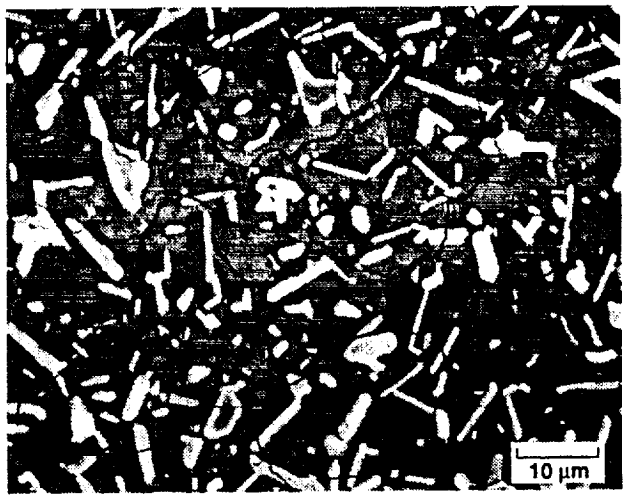

Figure 11

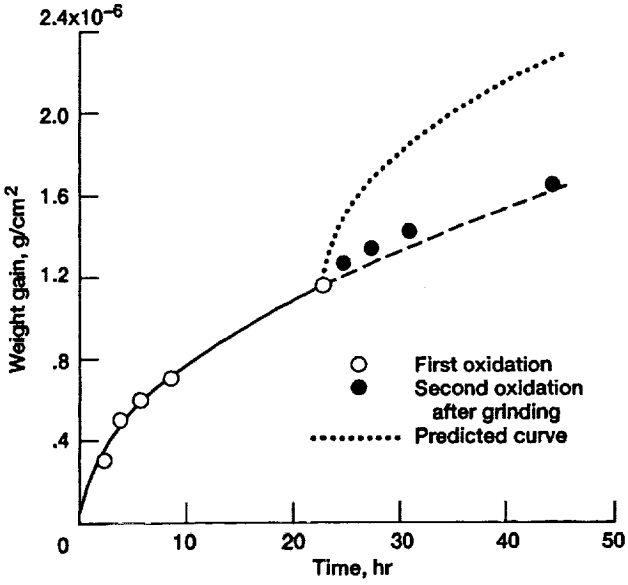
2.4x10⁻⁶
2.0
1.6
1.2
.8
.4
0
10
20
30
40
50
Weight gain, g/cm²
Time, hr
First oxidation
Second oxidation after grinding
Predicted curve

Figure 12

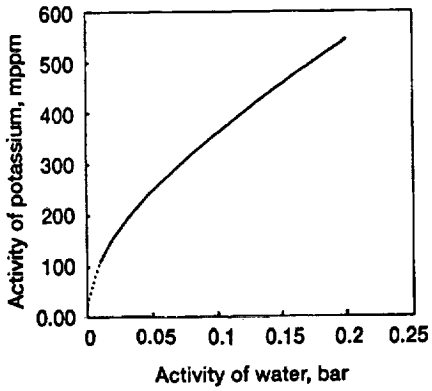
600
500
400
300
200
100
0.00
Activity of potassium, mppm
0
0.05
0.1
0.15
0.2
0.25
Activity of water, bar

Figure 13

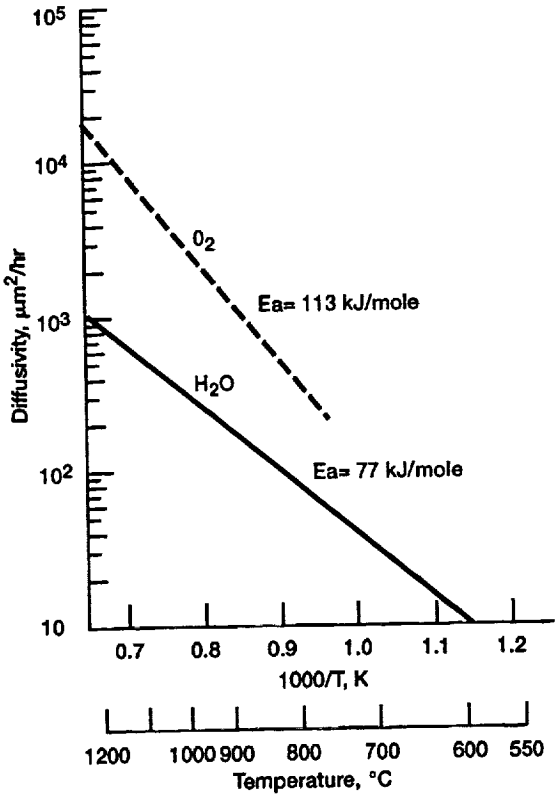
10^5
10^4
10^3
10^2
10
Diffusivity, $\mu m^2/hr$
O_2
Ea= 113 kJ/mole
H_2O
Ea= 77 kJ/mole
0.7
0.8
0.9
1.0
1.1
1.2
1000/T, K
1200
1000
900
800
700
600
550
Temperature, °C

Figure 14

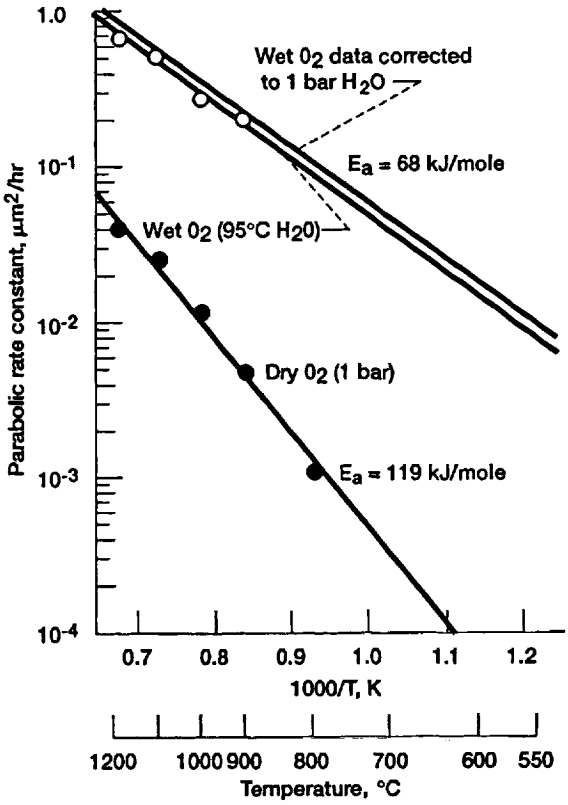
1.0
10^{-1}
10^{-2}
10^{-3}
10^{-4}
Parabolic rate constant, $\mu m^2/hr$
Wet 0_2 data corrected to 1 bar H_2O
E_a = 68 kJ/mole
Wet 0_2 (95°C H_2O)
Dry 0_2 (1 bar)
E_a = 119 kJ/mole
0.7
0.8
0.9
1.0
1.1
1.2
1000/T, K
1200
1000
900
800
700
600
550
Temperature, °C

Figure 15

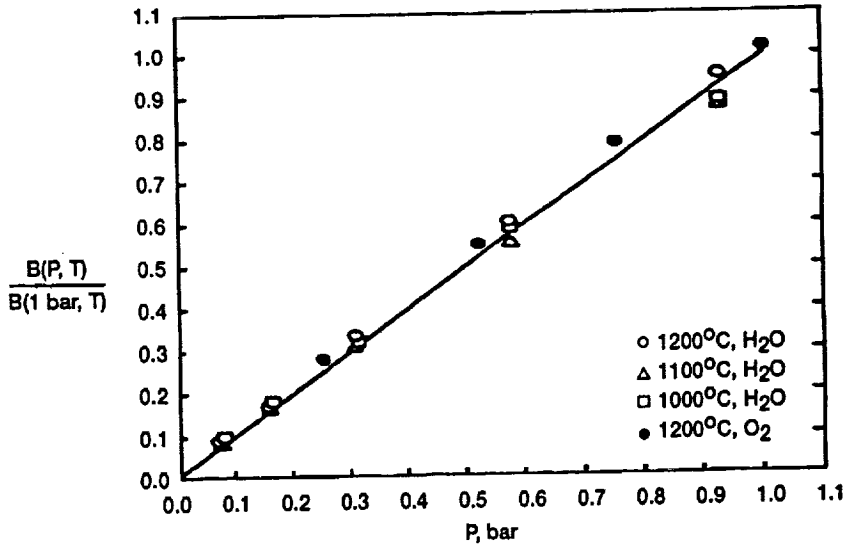
B(P, T) / B(1 bar, T)
1.1
1.0
0.9
0.8
0.7
0.6
0.5
0.4
0.3
0.2
0.1
0.0
0.0 0.1 0.2 0.3 0.4 0.5 0.6 0.7 0.8 0.9 1.0 1.1
P, bar
o 1200°C, H2O
△ 1100°C, H2O
□ 1000°C, H2O
● 1200°C, O2

Figure 16

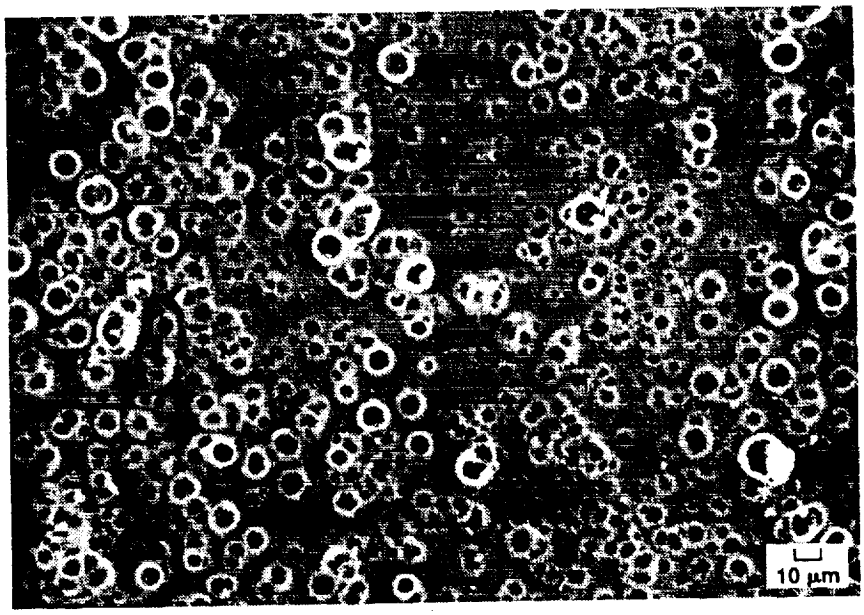

Figure 17

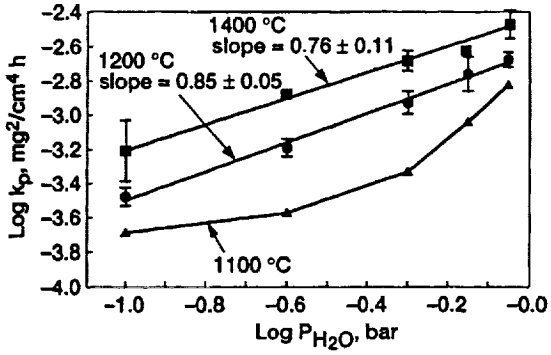
1400 °C
slope = 0.76 ± 0.11
1200 °C
slope = 0.85 ± 0.05
1100 °C
Log k_p, mg^2/cm^4 h
Log P_{H_2O}, bar
-2.4
-2.6
-2.8
-3.0
-3.2
-3.4
-3.6
-3.8
-4.0
-1.0
-0.8
-0.6
-0.4
-0.2
-0.0

Figure 18

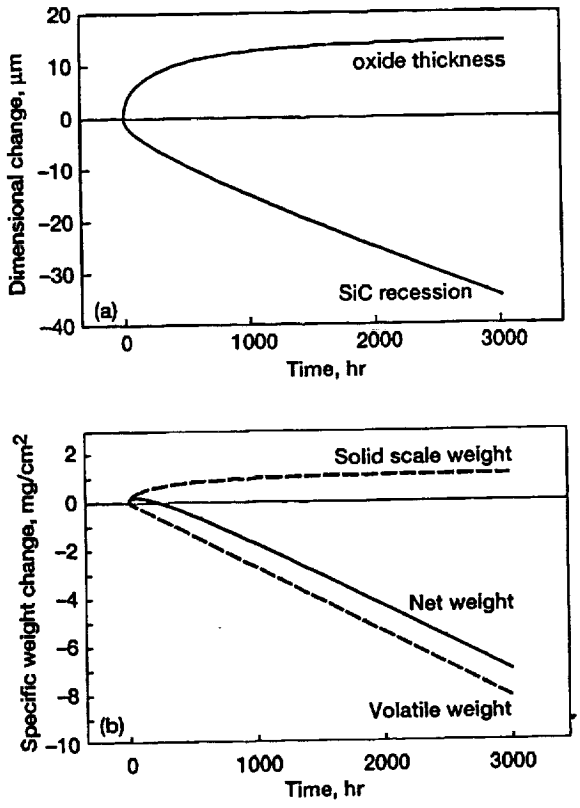
20
10
0
-10
-20
-30
-40
Dimensional change, μm
oxide thickness
SiC recession
(a)
0
1000
2000
3000
Time, hr
2
0
-2
-4
-6
-8
-10
Specific weight change, mg/cm²
Solid scale weight
Net weight
Volatile weight
(b)
0
1000
2000
3000
Time, hr

Figure 19

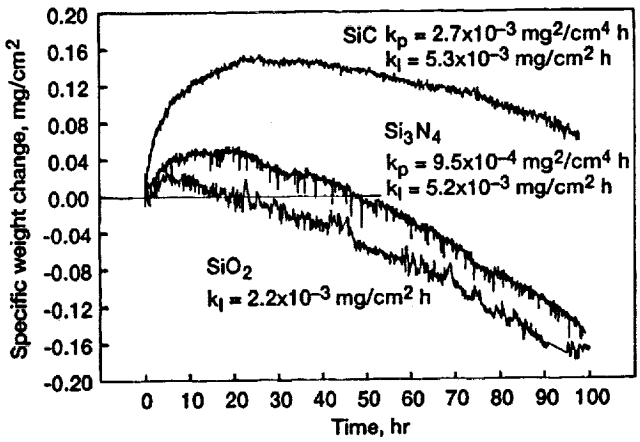
SiC $k_p = 2.7x10^{-3}$ mg^2/cm^4 h
$k_l = 5.3x10^{-3}$ mg/cm^2 h
Si_3N_4
$k_p = 9.5x10^{-4}$ mg^2/cm^4 h
$k_l = 5.2x10^{-3}$ mg/cm^2 h
SiO_2
$k_l = 2.2x10^{-3}$ mg/cm^2 h
Specific weight change, mg/cm^2
0.20
0.16
0.12
0.08
0.04
0.00
-0.04
-0.08
-0.12
-0.16
-0.20
0 10 20 30 40 50 60 70 80 90 100
Time, hr

Figure 20

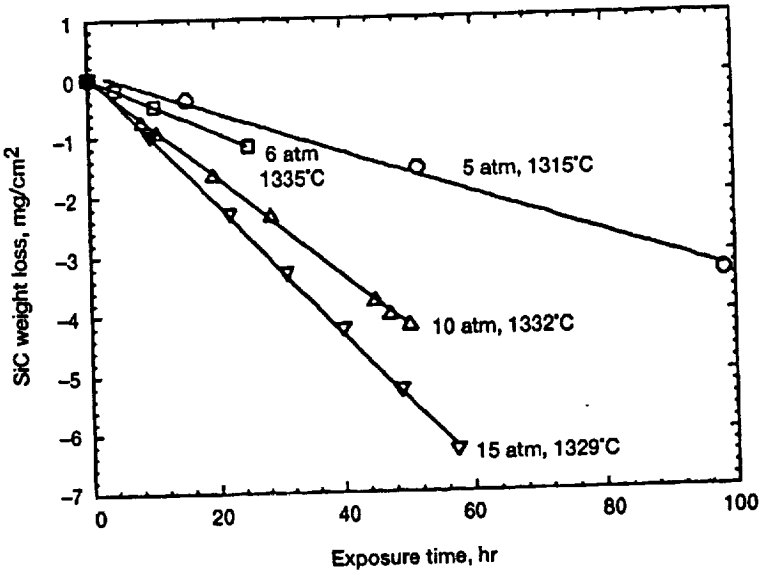
1
0
−1
−2
−3
−4
−5
−6
−7
0
20
40
60
80
100
SiC weight loss, mg/cm²
Exposure time, hr
6 atm
1335°C
5 atm, 1315°C
10 atm, 1332°C
15 atm, 1329°C

Figure 21

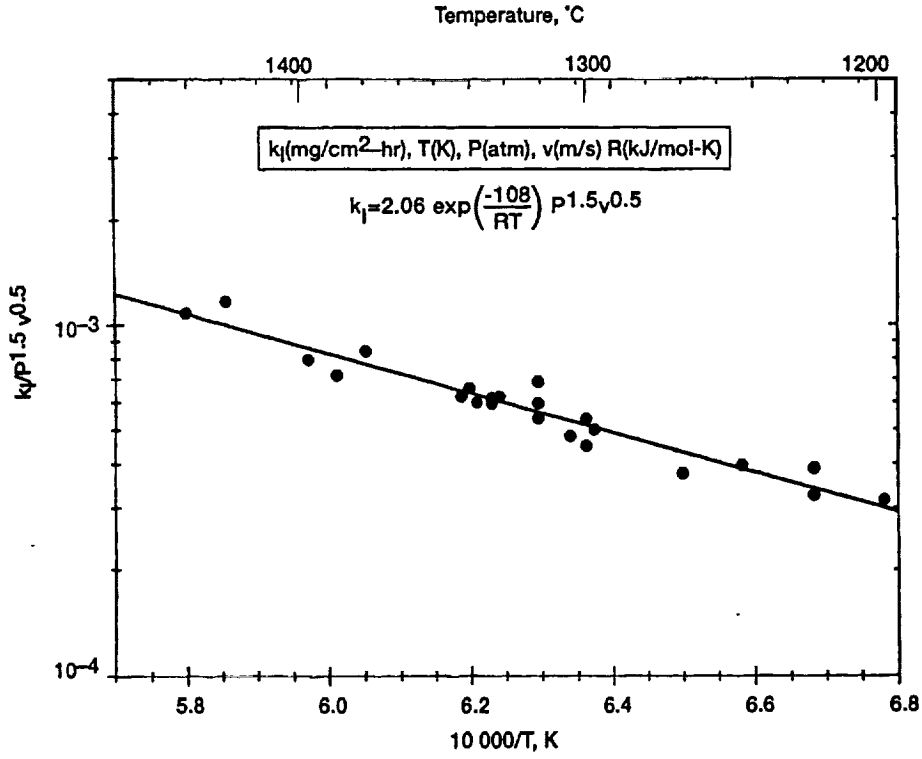
Temperature, °C
1400
1300
1200
k_l(mg/cm^2–hr), T(K), P(atm), v(m/s) R(kJ/mol-K)
k_l=2.06 exp$\left(\frac{-108}{RT}\right)$ P1.5$_V$0.5
k_l/P1.5 $_V$0.5
10^{-3}
10^{-4}
5.8
6.0
6.2
6.4
6.6
6.8
10 000/T, K

Figure 22

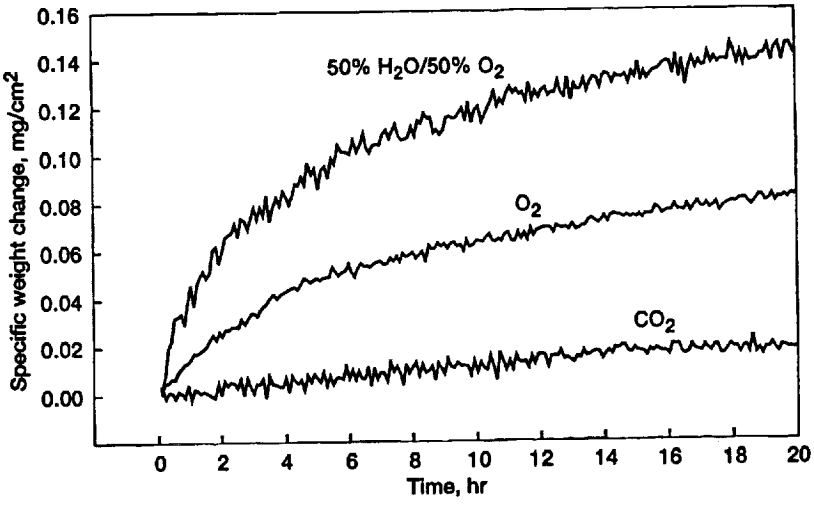
0.16
0.14
0.12
0.10
0.08
0.06
0.04
0.02
0.00
Specific weight change, mg/cm²
50% H₂O/50% O₂
O₂
CO₂
0
2
4
6
8
10
12
14
16
18
20
Time, hr

Figure 23

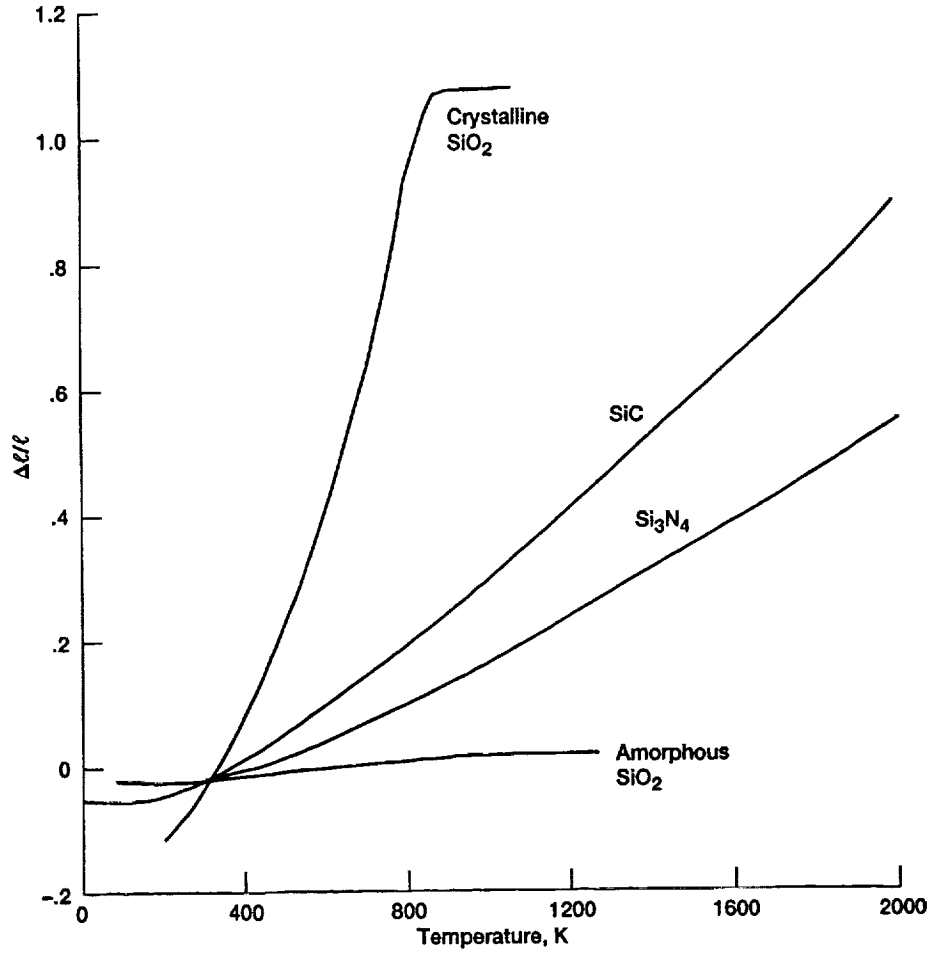
1.2
1.0
.8
.6
.4
.2
0
-.2
Δℓ/ℓ
Crystalline
SiO2
SiC
Si3N4
Amorphous
SiO2
0
400
800
1200
1600
2000
Temperature, K

Figure 24

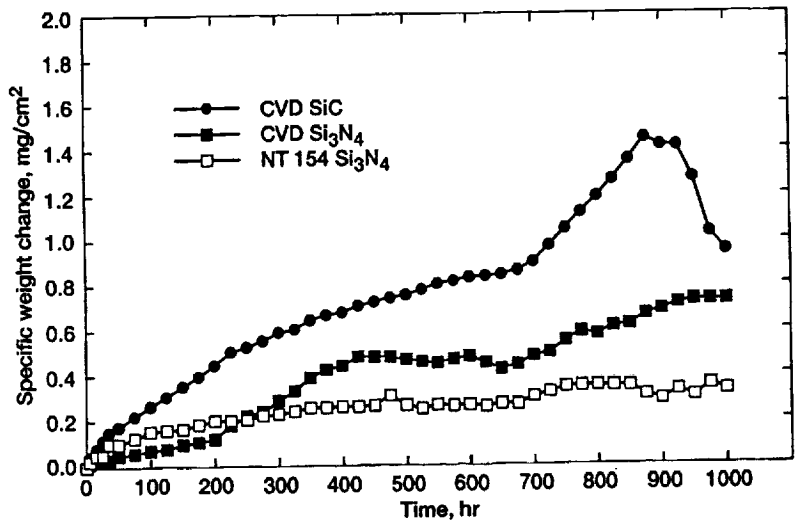
2.0
1.8
1.6
1.4
1.2
1.0
0.8
0.6
0.4
0.2
0.0
Specific weight change, mg/cm²
CVD SiC
CVD Si3N4
NT 154 Si3N4
0
100
200
300
400
500
600
700
800
900
1000
Time, hr

Figure 25

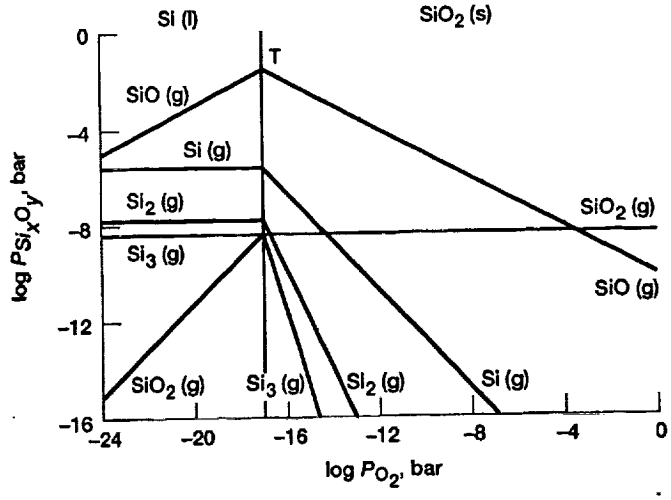
Si (l)
SiO2 (s)
T
SiO (g)
Si (g)
Si2 (g)
Si3 (g)
SiO2 (g)
SiO (g)
SiO2 (g)
Si3 (g)
Si2 (g)
Si (g)
0
-4
-8
-12
-16
-24
-20
-16
-12
-8
-4
0
log PSixOy, bar
log PO2, bar

Figure 26(a)

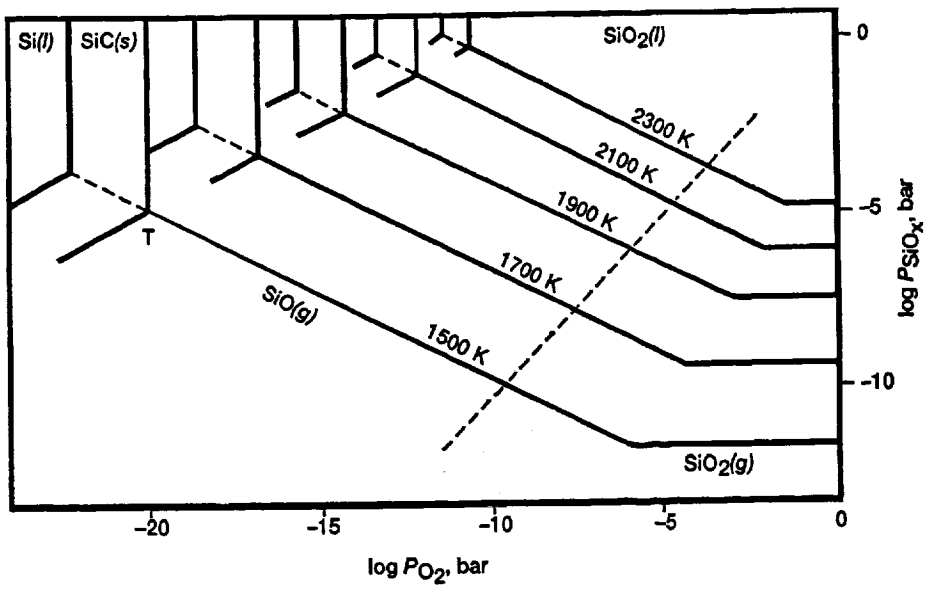
Si(l)
SiC(s)
SiO2(l)
2300 K
2100 K
1900 K
1700 K
1500 K
T
SiO(g)
SiO2(g)
0
-5
-10
log PSiOx, bar
-20
-15
-10
-5
0
log PO2, bar

Figure 26 (b)

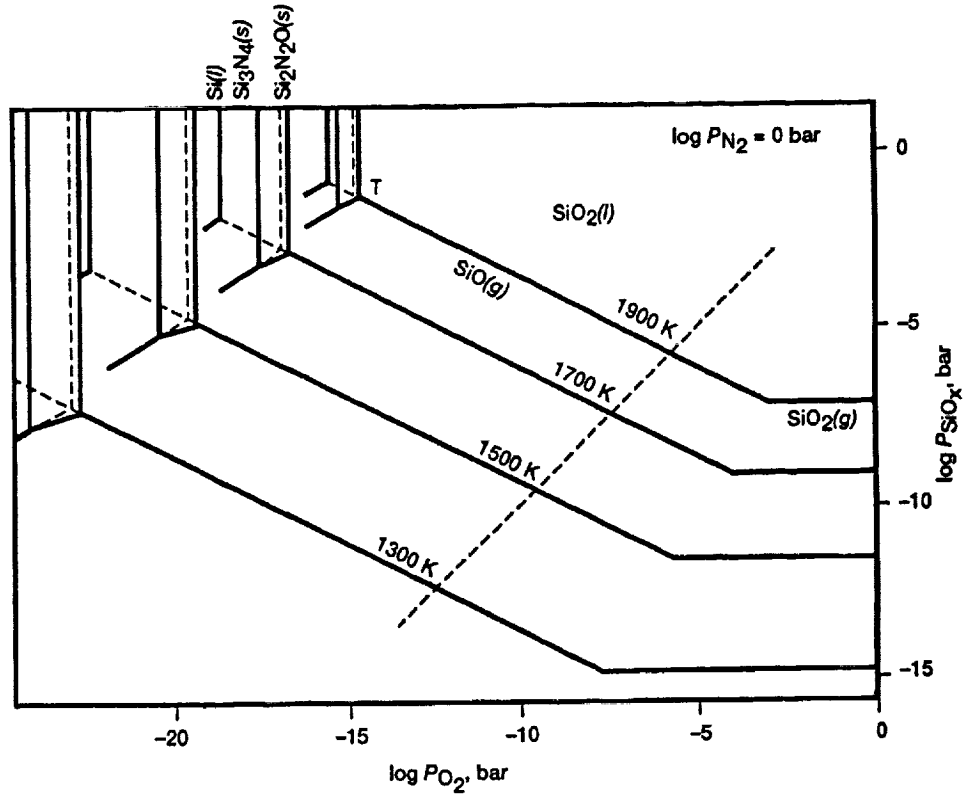
Si(l)
Si3N4(s)
Si2N2O(s)
T
log PN2 = 0 bar
SiO2(l)
SiO(g)
1900 K
1700 K
1500 K
1300 K
SiO2(g)
0
-5
-10
-15
log PSiOx, bar
-20
-15
-10
-5
0
log PO2, bar

Figure 26 (c)

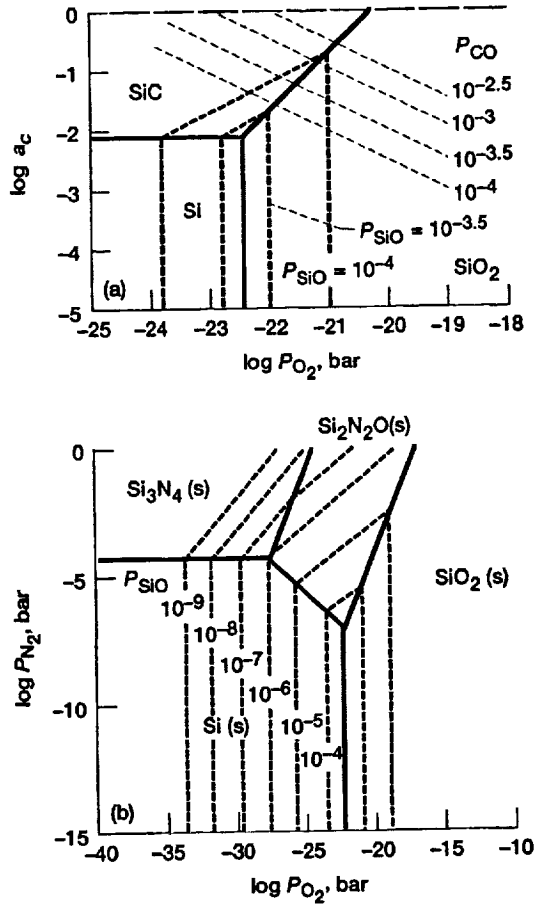
0
-1
-2
-3
-4
-5
log a_c
SiC
Si
P_{CO}
$10^{-2.5}$
10^{-3}
$10^{-3.5}$
10^{-4}
$P_{SiO} = 10^{-3.5}$
$P_{SiO} = 10^{-4}$
SiO_2
(a)
-25 -24 -23 -22 -21 -20 -19 -18
log P_{O_2}, bar
Si_2N_2O(s)
Si_3N_4 (s)
SiO_2 (s)
P_{SiO}
10^{-9}
10^{-8}
10^{-7}
10^{-6}
10^{-5}
10^{-4}
Si (s)
log P_{N_2}, bar
0
-5
-10
-15
(b)
-40 -35 -30 -25 -20 -15 -10
log P_{O_2}, bar

Figure 27

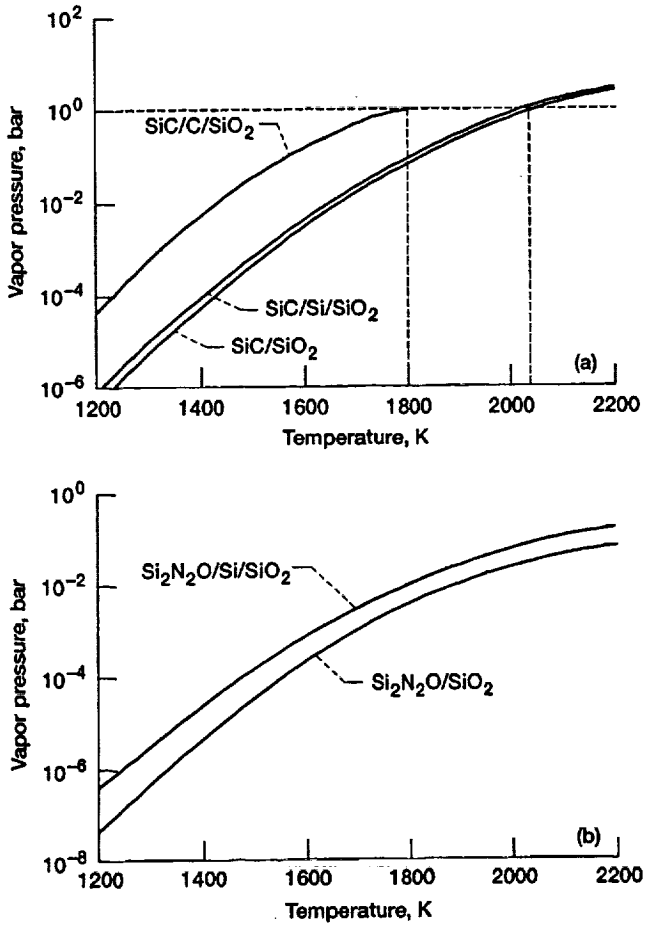
Vapor pressure, bar
10^2
10^0
10^{-2}
10^{-4}
10^{-6}
$SiC/C/SiO_2$
$SiC/Si/SiO_2$
SiC/SiO_2
(a)
1200
1400
1600
1800
2000
2200
Temperature, K
Vapor pressure, bar
10^0
10^{-2}
10^{-4}
10^{-6}
10^{-8}
$Si_2N_2O/Si/SiO_2$
Si_2N_2O/SiO_2
(b)
1200
1400
1600
1800
2000
2200
Temperature, K

Figure 28

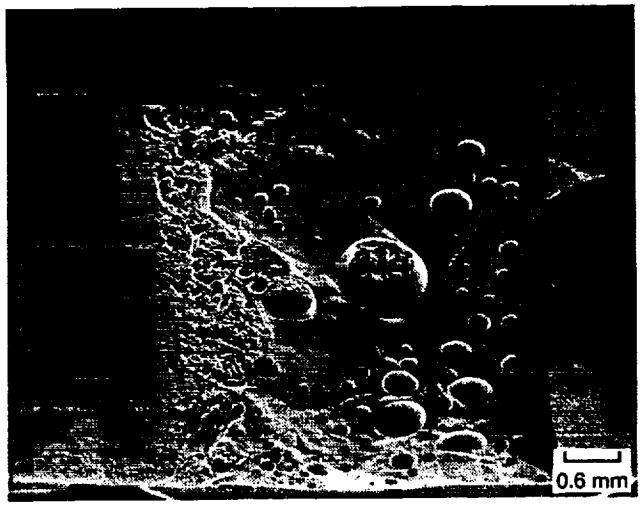

Figure 29

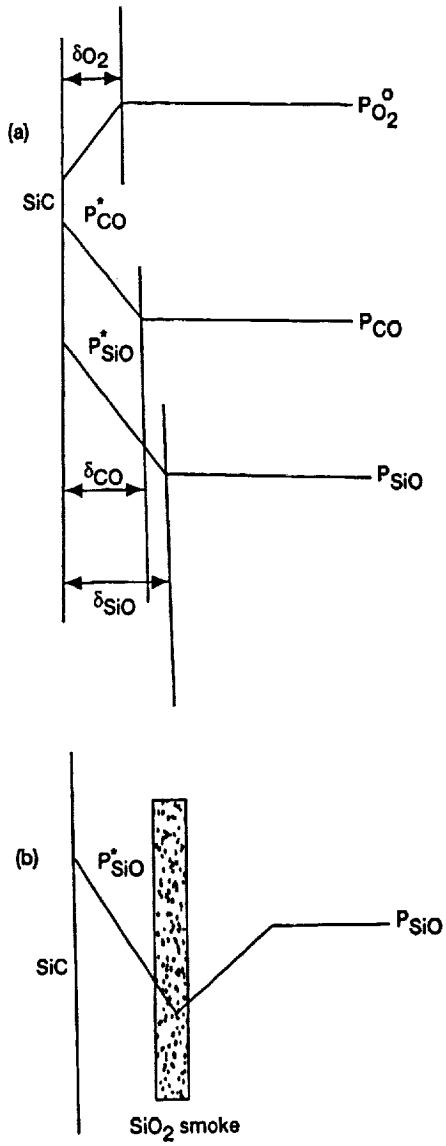
(a)
δO_2
$P^o_{O_2}$
SiC
P^*_{CO}
P_{CO}
P^*_{SiO}
P_{SiO}
δ_{CO}
δ_{SiO}
(b)
P^*_{SiO}
P_{SiO}
SiC
SiO_2 smoke

Figure 30

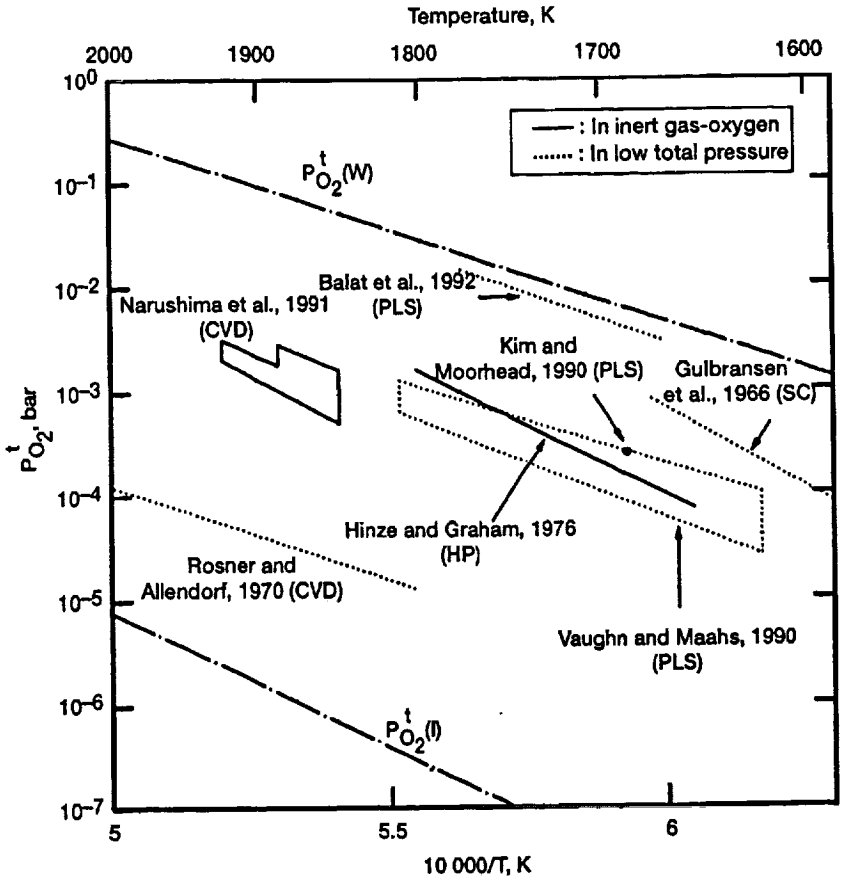
Temperature, K
2000
1900
1800
1700
1600
10^0
10^{-1}
10^{-2}
10^{-3}
10^{-4}
10^{-5}
10^{-6}
10^{-7}
$P^t_{O_2}$, bar
—— : In inert gas-oxygen
..... : In low total pressure
$P^t_{O_2}$(W)
Balat et al., 1992 (PLS)
Narushima et al., 1991 (CVD)
Kim and Moorhead, 1990 (PLS)
Gulbransen et al., 1966 (SC)
Hinze and Graham, 1976 (HP)
Rosner and Allendorf, 1970 (CVD)
Vaughn and Maahs, 1990 (PLS)
$P^t_{O_2}$(l)
5
5.5
6
10 000/T, K

Figure 31

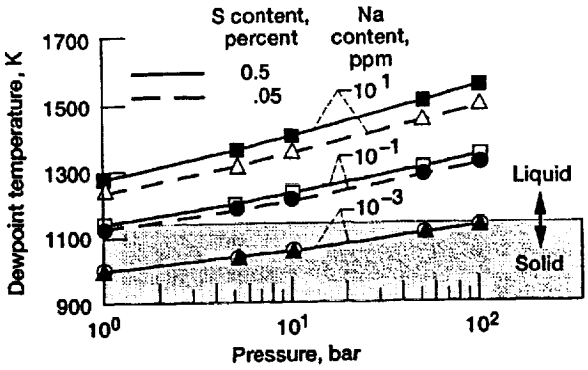
S content, percent
0.5
.05
Na content, ppm
10^1
10^{-1}
10^{-3}
Liquid
Solid
Dewpoint temperature, K
1700
1500
1300
1100
900
10^0
10^1
10^2
Pressure, bar

Figure 32

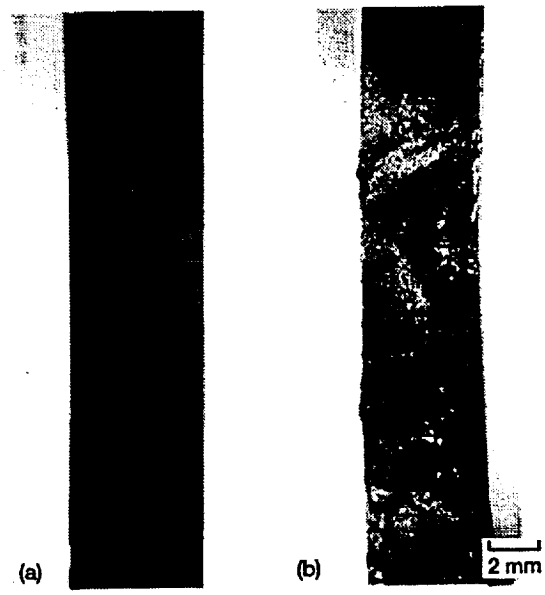

Figure 33

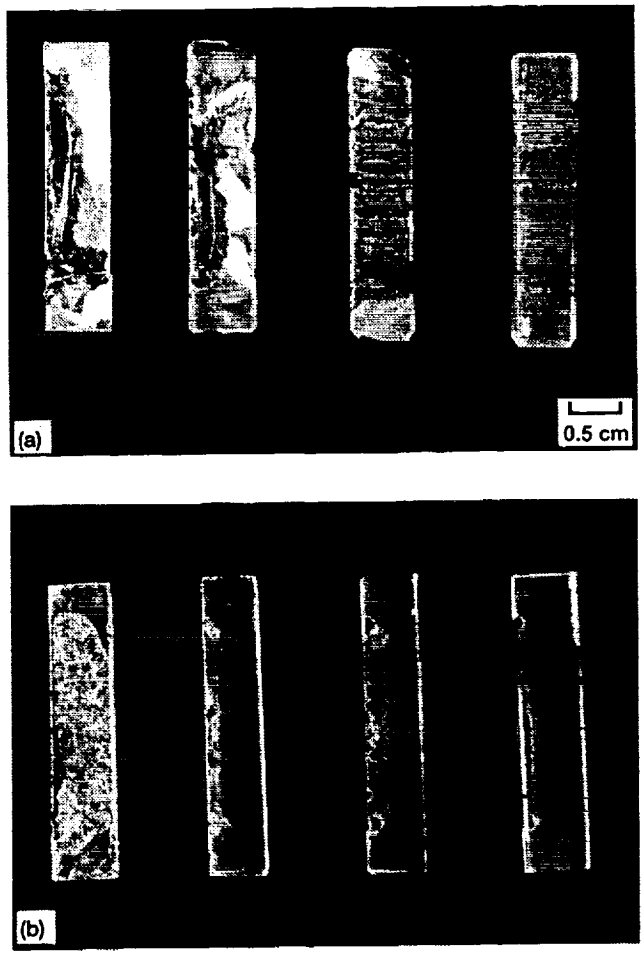

Figure 34

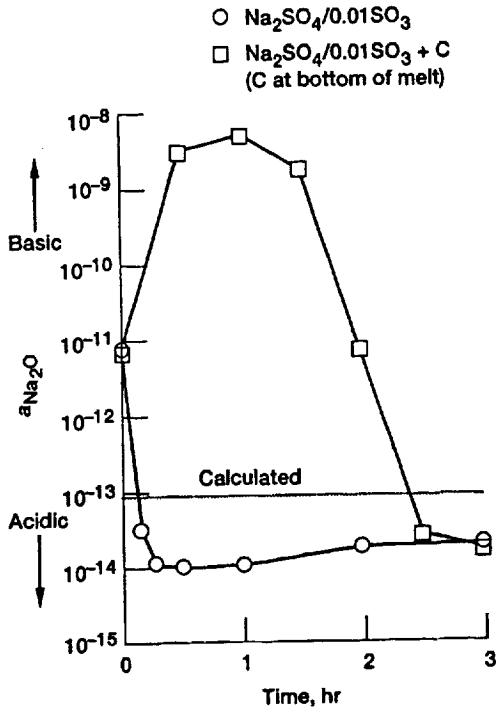
○ $Na_2SO_4/0.01SO_3$
□ $Na_2SO_4/0.01SO_3$ + C
(C at bottom of melt)
10^{-8}
10^{-9}
Basic
10^{-10}
10^{-11}
a_{Na_2O}
10^{-12}
Calculated
10^{-13}
Acidic
10^{-14}
10^{-15}
0
1
2
3
Time, hr

Figure 35

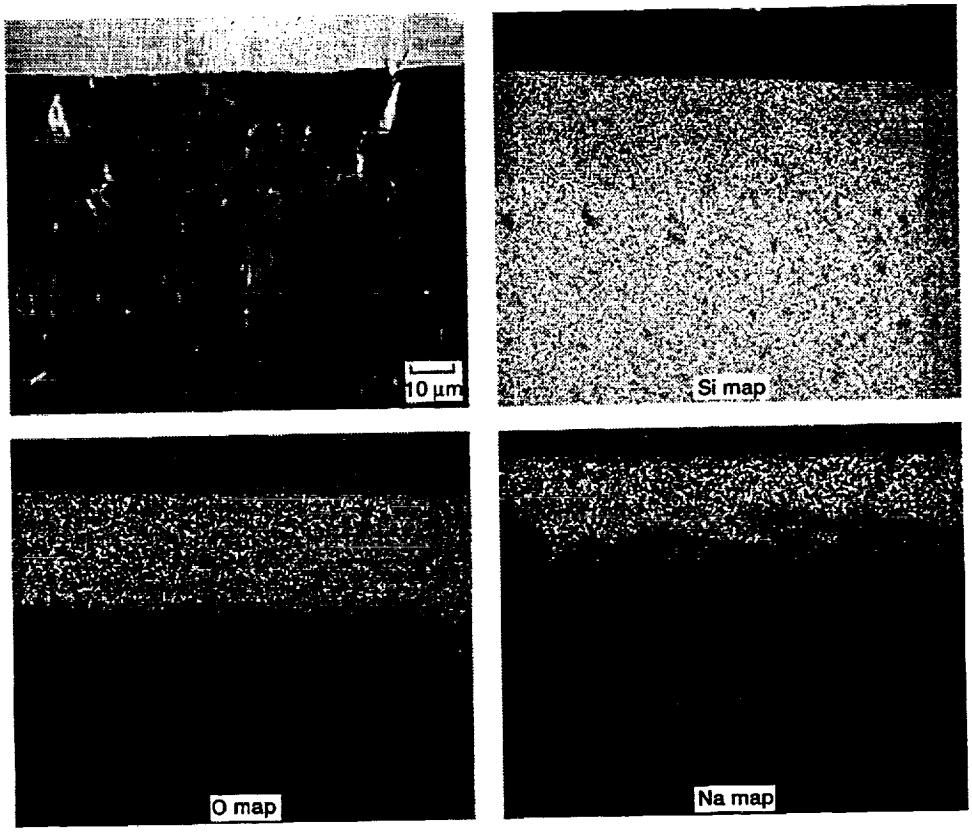

Figure 36

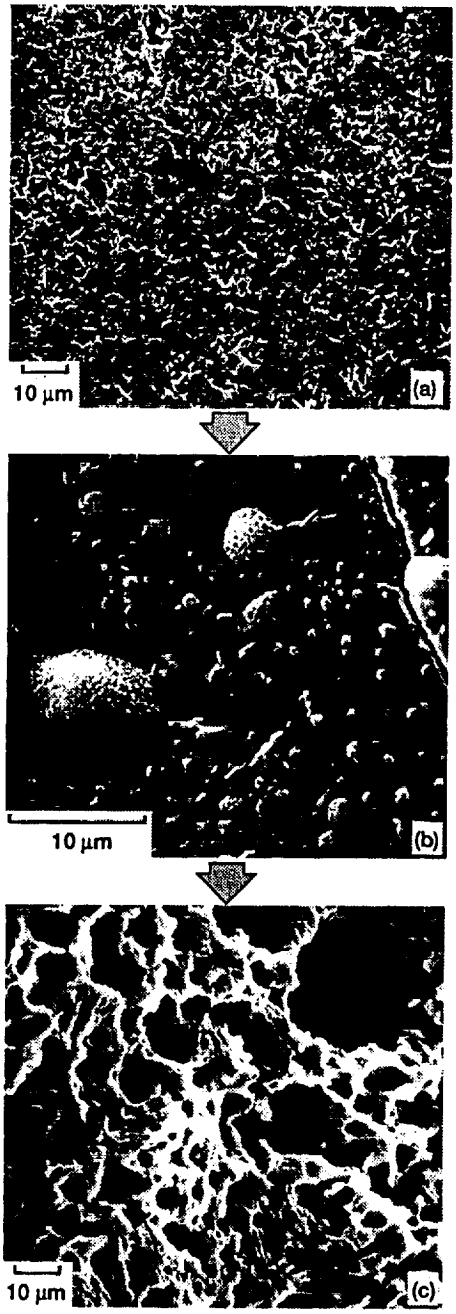

Figure 37

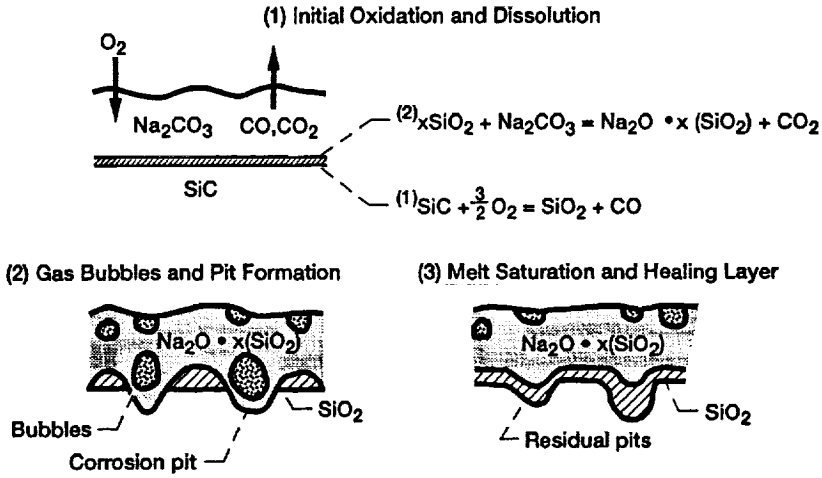
(1) Initial Oxidation and Dissolution
O_2
Na_2CO_3 CO,CO_2
SiC
$^{(2)}xSiO_2 + Na_2CO_3 = Na_2O \cdot x(SiO_2) + CO_2$
$^{(1)}SiC + \frac{3}{2}O_2 = SiO_2 + CO$
(2) Gas Bubbles and Pit Formation
$Na_2O \cdot x(SiO_2)$
SiO_2
Bubbles
Corrosion pit
(3) Melt Saturation and Healing Layer
$Na_2O \cdot x(SiO_2)$
SiO_2
Residual pits

Figure 38

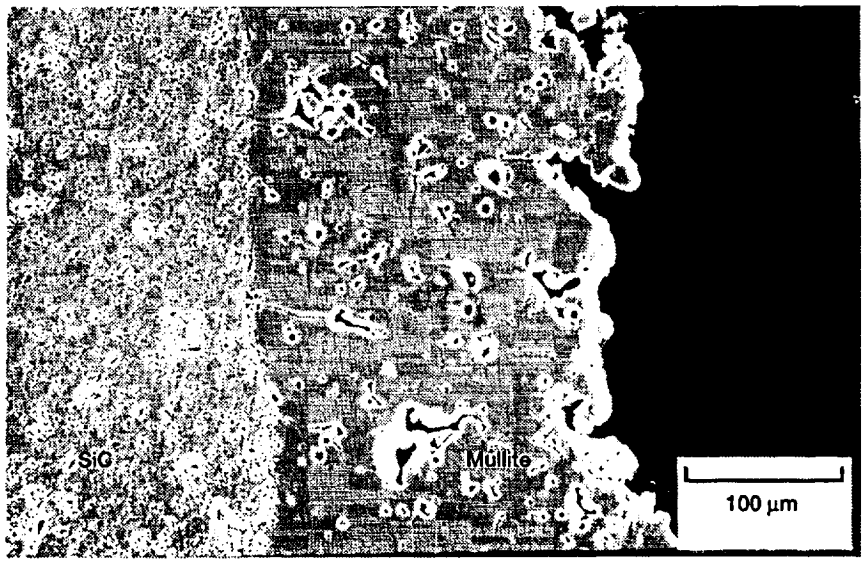

Figure 39

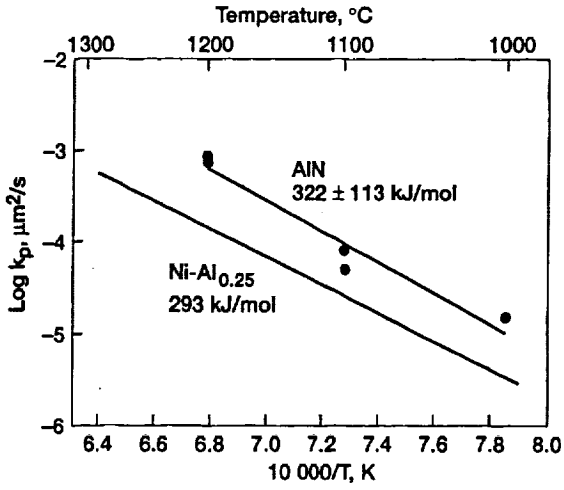
Temperature, °C
1300
1200
1100
1000
−2
−3
−4
−5
−6
Log k_p, $\mu m^2/s$
AlN
322 ± 113 kJ/mol
Ni-$Al_{0.25}$
293 kJ/mol
6.4
6.6
6.8
7.0
7.2
7.4
7.6
7.8
8.0
10 000/T, K

Figure 40

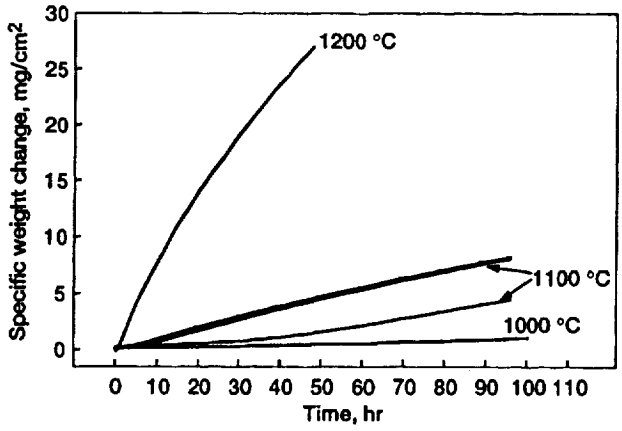
Specific weight change, mg/cm²
30
25
20
15
10
5
0
1200 °C
1100 °C
1000 °C
0 10 20 30 40 50 60 70 80 90 100 110
Time, hr

Figure 41

Figure 42

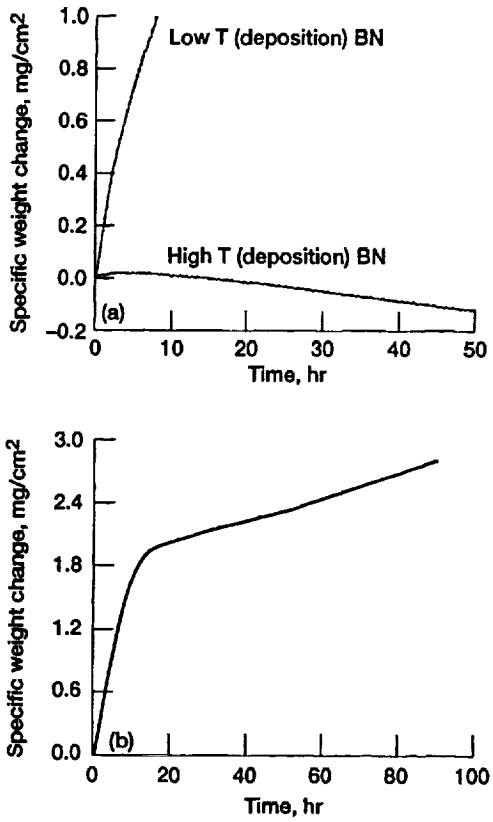
Specific weight change, mg/cm²
1.0
0.8
0.6
0.4
0.2
0.0
−0.2
Low T (deposition) BN
High T (deposition) BN
(a)
0
10
20
30
40
50
Time, hr
Specific weight change, mg/cm²
3.0
2.4
1.8
1.2
0.6
0.0
(b)
0
20
40
60
80
100
Time, hr

Figure 43

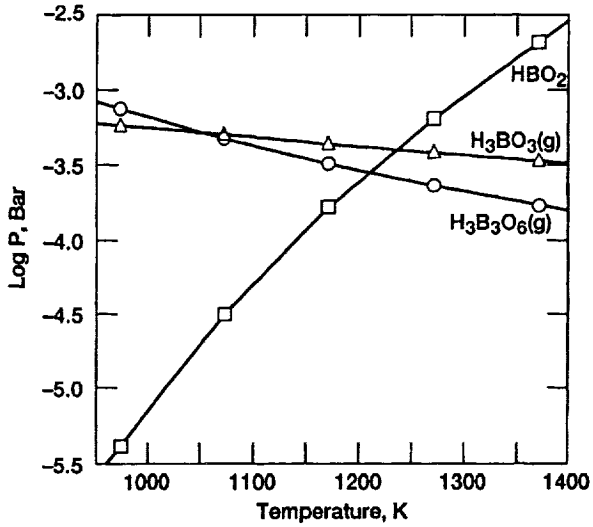
-2.5
-3.0
-3.5
-4.0
-4.5
-5.0
-5.5
Log P, Bar
1000
1100
1200
1300
1400
Temperature, K
HBO_2
$H_3BO_3(g)$
$H_3B_3O_6(g)$

Figure 44

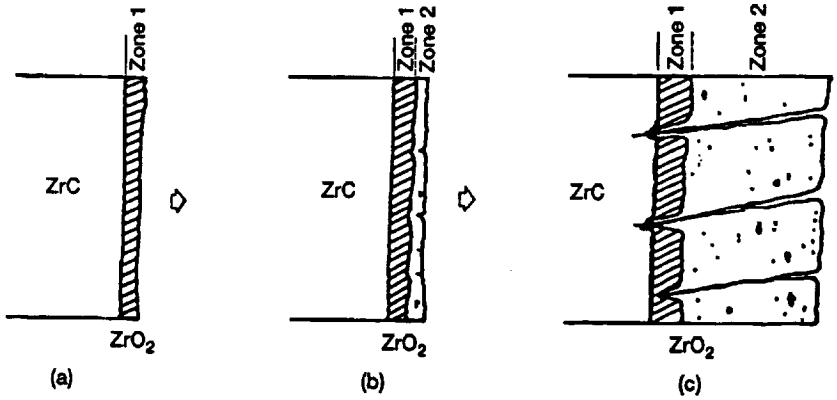

Figure 45

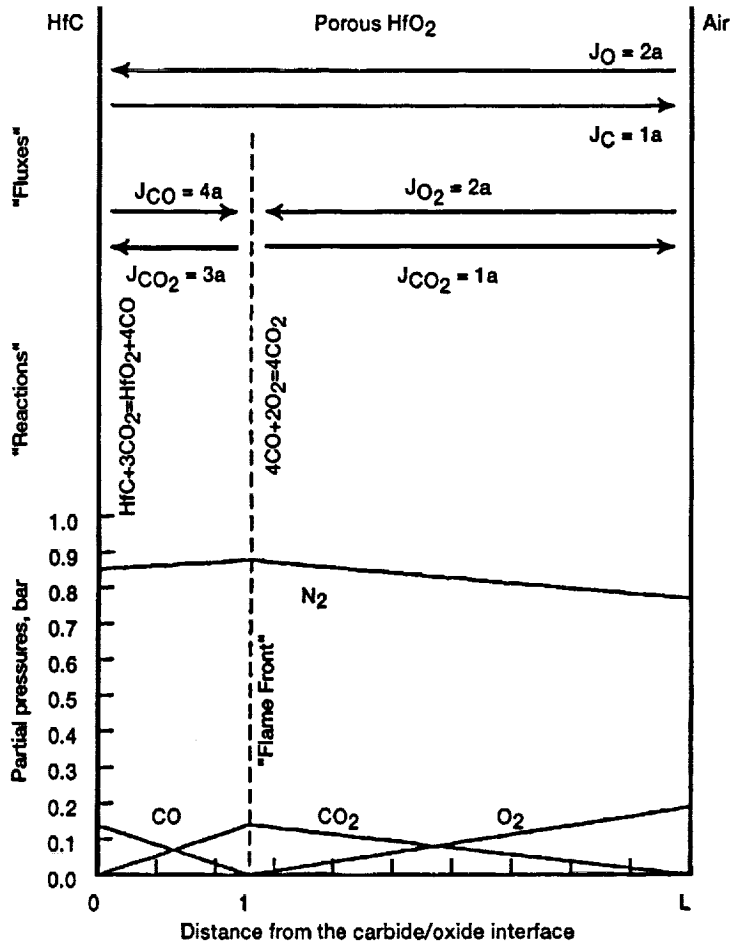
HfC
Porous HfO_2
Air
$J_O = 2a$
$J_C = 1a$
"Fluxes"
$J_{CO} = 4a$
$J_{O_2} = 2a$
$J_{CO_2} = 3a$
$J_{CO_2} = 1a$
"Reactions"
$HfC+3CO_2=HfO_2+4CO$
$4CO+2O_2=4CO_2$
Partial pressures, bar
1.0
0.9
0.8
0.7
0.6
0.5
0.4
0.3
0.2
0.1
0.0
N_2
"Flame Front"
CO
CO_2
O_2
0
1
L
Distance from the carbide/oxide interface

Figure 46

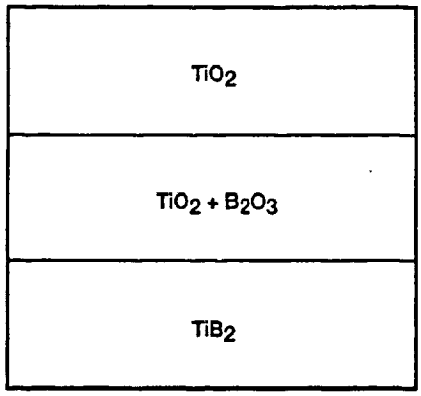

Figure 47

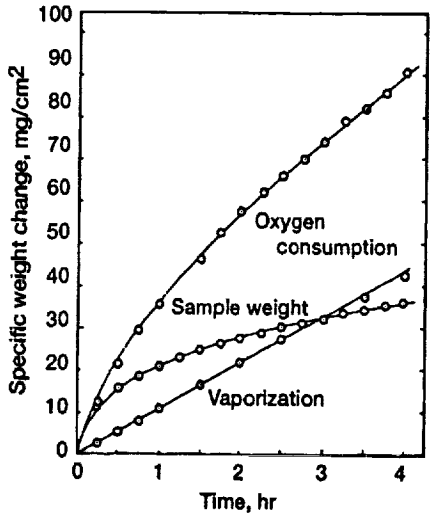
Specific weight change, mg/cm²
100
90
80
70
60
50
40
30
20
10
0
0
1
2
3
4
Time, hr
Oxygen consumption
Sample weight
Vaporization

Figure 48

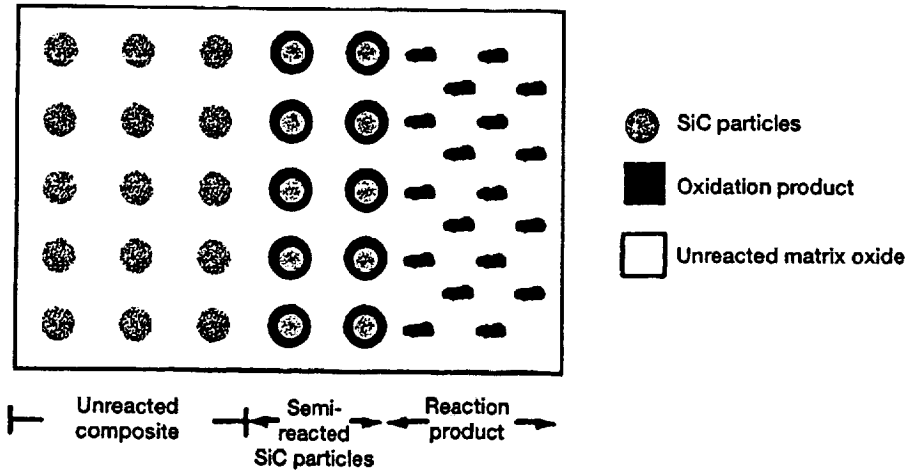
SiC particles
Oxidation product
Unreacted matrix oxide
Unreacted composite
Semi-reacted SiC particles
Reaction product

Figure 49

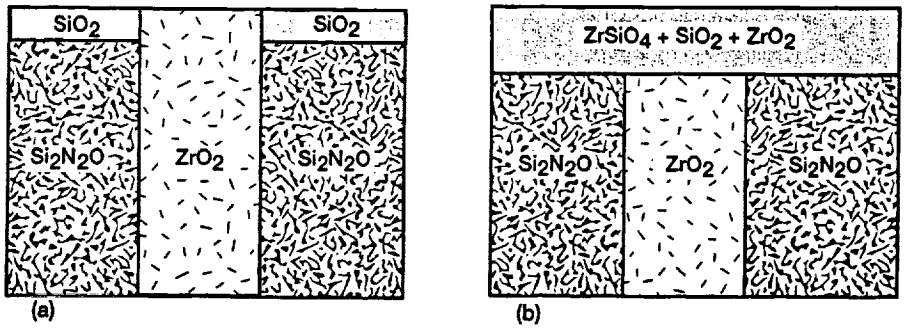
SiO2
SiO2
Si2N2O
ZrO2
Si2N2O
(a)
ZrSiO4 + SiO2 + ZrO2
Si2N2O
ZrO2
Si2N2O
(b)

Figure 50

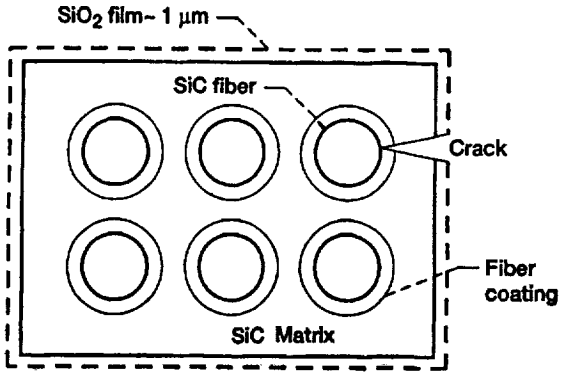

Figure 51

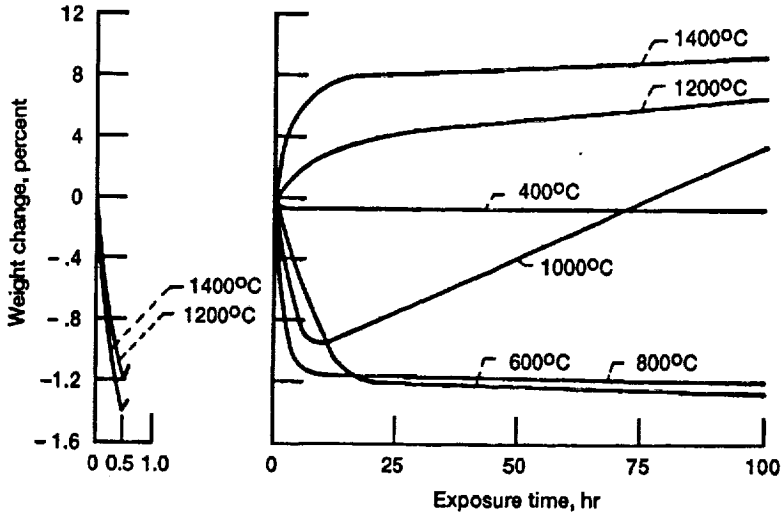
12
8
4
0
-.4
-.8
-1.2
-1.6
Weight change, percent
0 0.5 1.0
1400°C
1200°C
0
25
50
75
100
Exposure time, hr
1400°C
1200°C
400°C
1000°C
600°C
800°C

Figure 52

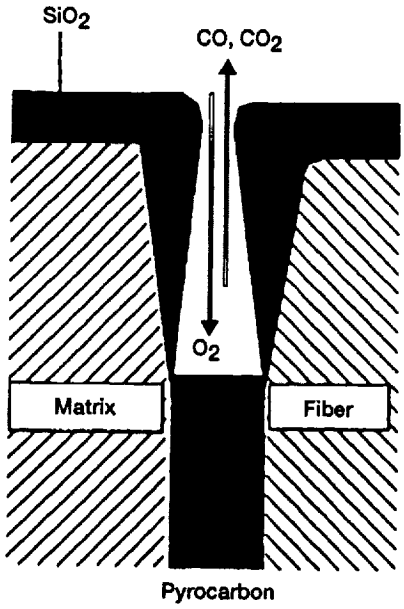

Figure 53

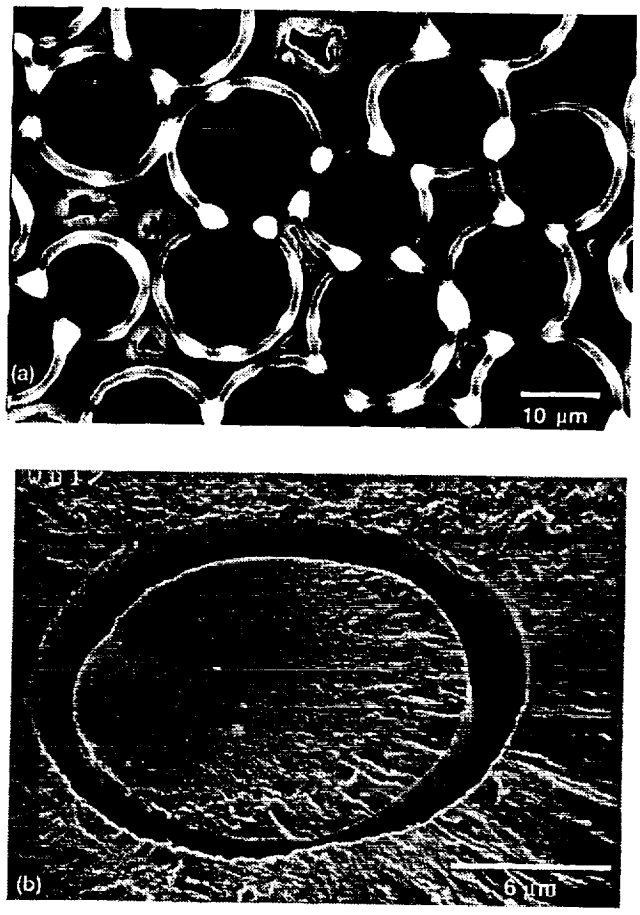

Figure 54

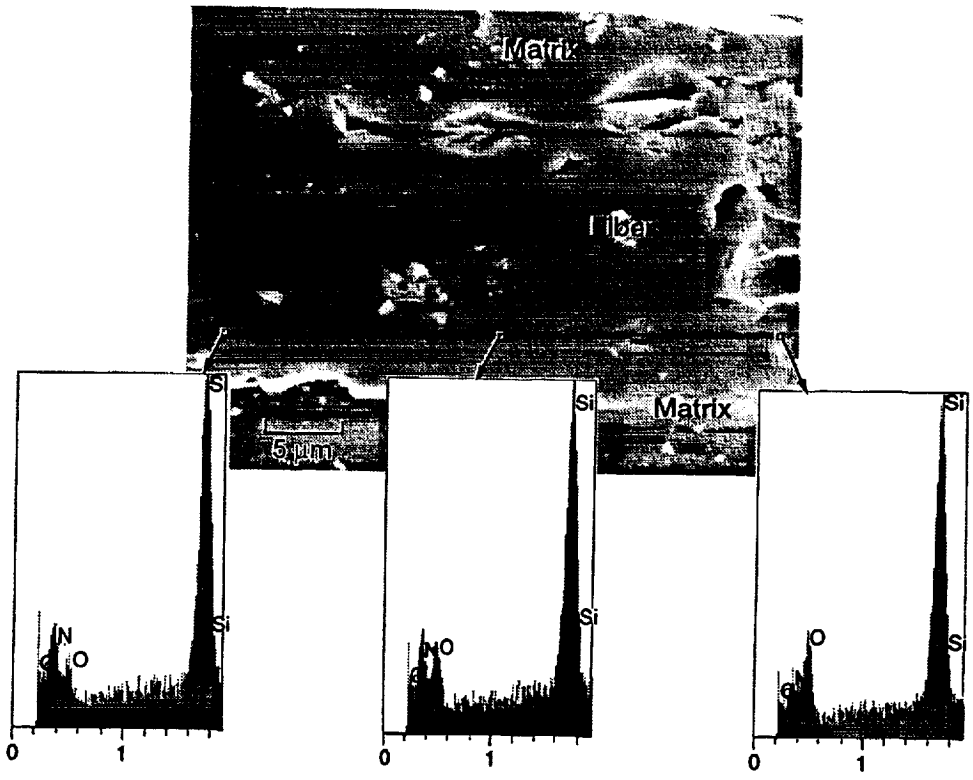

Fig 55

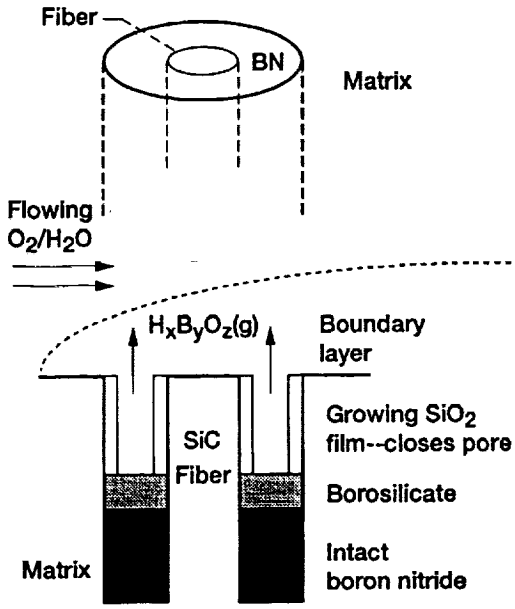
Fiber
BN
Matrix
Flowing
O_2/H_2O
$H_xB_yO_z(g)$
Boundary
layer
Growing SiO_2
film--closes pore
SiC
Fiber
Borosilicate
Intact
boron nitride
Matrix